Analysis of Energy Storage Performance of Supercapacitors With Crumpled Graphene Electrodes

Thesis

M. Sc. Engg (Mechanical)

Submitted by

Abrar Amin Khan

Student No. 0419102074

Department of Mechanical Engineering
Bangladesh University of Engineering and Technology (BUET)

June 2022

Analysis of Energy Storage Performance of Supercapacitors With Crumpled Graphene Electrodes

A Dissertation

by

Abrar Amin Khan (Student ID: 0419102074)

Under the Supervision of

Dr. Md. Ashiqur Rahman

MASTER OF SCIENCE IN MECHANICAL ENGINEERING

Department of Mechanical Engineering

BANGLADESH UNIVERSITY OF ENGINEERING AND TECHNOLOGY

June 2022

RECOMMENDATION OF THE BOARD OF EXAMINERS

The thesis titled "**Analysis of Energy Storage Performance of Supercapacitors with Crumpled Graphene Electrodes**" submitted by Abrar Amin Khan, Student No.: 0419102074, Session: April 2019, has been accepted as satisfactory in partial fulfillment of the requirement for the degree of Master of Science in Mechanical Engineering on 20th June, 2022.

BOARD OF EXAMINERS

Dr. Md. Ashiqur Rahman Professor Department of Mechanical Engineering BUET, Dhaka-1000	Chairman (Supervisor)
Dr. Muhammad Ashiqur Rahman Professor and Head Department of Mechanical Engineering BUET, Dhaka-1000	Member (Ex- officio)
Dr. Mohammad Nasim Hasan Professor Department of Mechanical Engineering BUET, Dhaka-1000	Member (Internal)
Dr. Md. Shakhawat Hossain Firoz Professor Department of Chemistry BUET, Dhaka-1000	Member (External)

CANDIDATE'S DECLARATION

It is hereby declared that this thesis/project or any part of it has not been submitted elsewhere for the award of any degree or diploma.

20/6/22

Abrar Amin Khan

Dedicated to my late maternal grandmother

ACKNOWLEDGEMENTS

"Acknowledging the good that you already have in your life is the foundation for all abundance.", starting with the very words of Eckhart Tolle, I want to begin by showing my utmost gratitude towards the almighty Allah. I personally believe everything in this world is controlled by Him

After that, without whom it would have been an impossible task to conduct this study is my supervisor Dr. Md. Ashiqur Rahman. He has been very helpful, co-operative and tolerant throughout the course of this research. His brilliant ideas, suggestions, encouragements accelerated my research to get the desired results.

I was able to access high-speed computational tools at BUET's Institute of Information and Communication Technology (IICT). I am extremely grateful to IICT for allowing me to use their computing resources. CASR, BUET, has provided financial support for this research project, which I am quite grateful for.

Then, I would like to mention the person who has been a constant support for me is my wife Anika Imraana Sohaana. She not only lends the mental support but also at times solved complicated problems that raised in front of me. In addition to that, no words are enough to thank my parents, Dr Fakrul Amin Khan and Dr Anwara Shareef for their continuous love, moral support and prayers. I also want to acknowledge my elder brother Dr. Arham Amin Khan for keeping me in the right track when I tend to lose my way. The roles of my extended family are worth mentioning too.

There are some people who have helped in so many direct and indirect ways throughout this project. I would like appreciate Musanna Galib who is a pioneer researcher in supercapacitors. His guidance helped me a lot. Dr. Fazle Elahi Ashek, Tanveer Islam Joy, Tousif Jamee, Sazid Noor are some other names I would like to recognize their contribution.

Finally I extend my heartiest gratitude to the board members, Dr. Muhammad Ashiqur Rahman, Head department of ME, BUET, Dr. Mohammad Nasim Hasan, and Dr. Md. Shakhawat Hossain Firoz, to give their invaluable time to attend my M.Sc defense.

ABSTRACT

The Electric Double Layer Capacitors (EDLC) are one of the most promising technologies now-a-days in the field of energy storage due to its excellent power density, great cyclability and faster charging-discharging. However, having a lower energy density than batteries leading researchers to optimize the performance of supercapacitors by enhancing their energy storage capability. Improving the electrode design of the supercapacitors has been the primary approach in this regard. In this study, to enhance the capacitive performance of supercapacitors, EDLC with crumpled graphene electrode has been designed with aqueous (NaCl) electrolyte. This study is performed with the aid of molecular dynamics (MD) simulation to analyze the influence of crumpled graphene electrode on the EDLC performance. The findings show that the proposed EDLC model possesses five times higher specific capacitance (16.351 $\mu F/cm^{-2}$) than the planar graphene. Better charging mechanism and higher ion accessible area are the reasons behind this improved performance. In addition, the effects of the degree of crumpling of graphene, inclusion of defects on the crumpled graphene surface, and the variation of surface wettability on the performance of the modeled EDLC are also examined. The effect of degree of crumpling is found to be that complete crumpling aids the capacitive ability of the EDLC. The most optimized structure of the crumpled graphene electrode is observed for an added vacancy of 20% which possesses an outstanding specific capacitance of 19.8 $\mu F/cm^{-2}$. Finally, for the effect of surface wettability, it is observed that super-hydrophilic electrodes facilitate better electrode-electrolyte interaction and improves ion separation, leading to a superior performance than the hydrophobic surfaces. The major takeaway from the project is that it provides significant insight into the potential of crumpled graphene electrode-based EDLC and sheds light on the possibility of achieving the desired balance of high-storage and high-power energy.

NOMENCLATURE

A	:	Surface area of the electrode
C	:	Capacitance of the EDLC
C_A	:	Capacitances of the anode
C_C	:	Capacitances of the cathode
C_T	:	Total capacitance
d	:	Effective thickness of the double layer
E	:	Energy density
ε	:	Electrolyte's dielectric constant
ε_0	:	Vacuum's dielectric constant
P	:	Power density
Q	:	Charge quantity
T	:	Temperature (K)

Abbreviation

ACN	:	Acetonitrile
CNT	:	Carbon nanotube
Cl^-	:	Chloride
EDL	:	Electric double-layer
EDLC	:	Electrical double layer capacitor
ES	:	Electrochemical supercapacitor
ESR	:	Equivalent series resistance
GCS	:	Gouy-Chapman-Stern
IHP	:	Inner Helmholtz plane
MD	:	Molecular dynamics
Na^+	:	Sodium
OHP	:	Outer Helmholtz plane
RTIL	:	Room-temperature ionic liquids
SPC/E	:	Simple point charge
TIP3P	:	Three-pointtransferrable intermolecular potential

Table of Contents

Chapter 1 ..... **1**

Introduction **1**

1.1 General Introduction 1

1.2 Fundamentals of Supercapacitors 3

1.2.1 EDLC Supercapacitor 4

1.2.2. Pseudocapacitors 5

1.3 Differences between Battery and Capacitors 6

1.4 Different Models of EDLC 7

1.4.1 Helmholtz Model 7

1.4.2 Gouy-Chapman or Diffuse Model 8

1.4.3 Stern Model 9

1.5 Characterization of EDLC Performance 10

1.6 Advantages of EDLC Supercapacitors 11

1.7 Application of Supercapacitor 13

1.8 Limitations of EDLC Supercapacitors 14

1.9 Review of Germane Work 14

1.9.1 Usage of Porous Materials as Electrode 15

1.9.2 Investigation on 0-D and 1-D Materials as EDLC Electrode 17

1.9.3 Graphene and Crumple Graphene Electrodes 18

1.9.4 Effects of Electrolytes on the Performance of EDLC 25

1.10 Objective of This Study 27

Chapter 2 ..... **29**

Computational Methodology **29**

2.1 Molecular Dynamics Simulation 29
2.1.1 Large-scale Atomic/Molecular Massively Parallel Simulator (LAMMPS) 29
2.1.2 Modelling the Physical System 30
2.1.3 The Lennard-Jones Potential 31
2.1.4 Periodic Boundary Conditions (PBC) 33
2.1.5 Time Integration Algorithm 34
2.1.5.1 The Verlet Algorithm 35
2.1.6 Ensembles 36
2.1.6.1 NPT Ensemble 37
2.1.6.2 NVT Ensemble 37
2.1.6.3 NVE Ensemble 37
2.1.6.4 NPH Ensemble 37
2.1.7 Particle-Particle Particle-Meshstyle (PPPM) 38
2.1.8 General Procedure of Molecular Dynamics Simulation 39
2.1.9 Limitations of MD Simulations 40
2.1.9.1 Use of Classical Forces 40
2.1.9.2 Realism of Forces 40
2.1.9.3 Time and Size Limitation 41
2.2 Modelling the Simulation Domain for Current Study 41
2.2.1 Modelling Crumpled-Graphene Sheets in LAMMPS 42
2.2.2 Electrolyte Modelling 44
2.2.3 Simulation Physics Employed in the Present Study 46
2.2.4 Units: Real, Metal and SI Units 46
2.2.5 Simulation Time Step 47
2.2.6 Simulation Domain 48

2.2.7 Pair_Style, Bond_Style and Angle_Style Commands 50
2.3 Simulation Parameters 50
2.3.1 Atom Types, Total number and Atomic Mass 50
2.3.2 Force Field Parameters – Bond Coefficients 50
2.3.3 LJ Parameters: Pair Coefficients 51
2.4 Modelling Electrodes for Different Degree of Crumpling of Graphene 52
2.5 Modelling of Crumpled Graphene with Defectss 55
2.6 Modelling the Variation of Surface Wettability 57
2.7 Surface Charge Density on Electrodes 58
2.8 Calculation of Electric Potential and Capacitance 59
Chapter 3 61
Results and Discussion 61
3.1 Validation 61
3.2 Performance of the EDLC with Crumpled-Graphene Electrode 63
3.2.1 Effect on Electrolyte Ions 64
3.2.2 Behavior of Water Molecules 66
3.2.3 Performance Parameter Analysis: 67
3.3 Effect of Crumpling State of the Graphene Electrodes 68
3.3.1 Influence on Interaction between Electrode-Electrolyte 68
3.3.2 Interactions between Electrode and Solvent 72
3.3.3 Impact on EDLC Energy Storage Ability 75
3.4 Supercapacitor Performance of Crumpled Graphene with Defects 79
3.4.1 Variation of Ion and Solvent Distribution with Different Amount of Defects 79
3.4.2 Comparison of EDLC Performance of Various Porous Electrodes 82
3.5 Effect of Surface Wettability of Crumpled Graphene Electrode on the EDLC Performance 88

3.5.1 Density Profiles of the Electrolyte Ions for Different Surface Wettability 88
3.5.2 Variation of Density Profiles of Water Molecules with Varied Contact Angles 90
3.5.3 Impact of Surface Wettability on EDLC Performance 91
Chapter 4 96
Conclusions and Recommendations 96
4.1 Conclusion 96
4.2 Recommendation 97
References 99
Appendices 113

List of Figures

Fig 1. 1: Specific energy and specific power scenario for different energy storage devices [1] 3
Fig 1. 2: Basic Structure of an EDLC (a) discharged state and (b) charged state. 4
Fig 1. 3: Schematic diagram of Pseducapacitor. 6
Fig 1. 4: Different Models of EDLC. (a) Helmholtz model (b) GC model (c) Stern Model. 7
Fig 1. 5: Electric bus powered by Li-ion battery with support of supercapacitor [18]. 12
Fig 1. 6: Taxonomy of supercapacitor materials [3]. 15
Fig 1. 7: Four typical structure for adsorption location [33]. 16
Fig 1. 8: Specific capacitance of planar and edge electrode [65]. 20
Fig 1. 9: Schematic diagram of (a) graphene and (b) crumpled graphene [77]. 23
Fig 1. 10: Variation of capacitance with respect to varied concentration of ACN [96]. 27

Fig 2. 1: Periodic boundary conditions (The central box is outlined by a thicker line)..... 34
Fig 2. 2: Schematic diagram of a basic MD code [107] 39
Fig 2. 3: Crumpling of Graphene from a layer of conventional planer graphene. 43
Fig 2. 4: Algorithm for Modelling electrolyte solution 44
Fig 2. 5: Full Set-up of the Simulation Model 49
Fig 2. 6: Simulation system for r=165.4 Å. 54
Fig 2. 7: Simulation system for r=110.1 Å 54
Fig 2. 8: Crumpled graphene for (a) 5% (b) 10% (c) 20% and (d) 30% vacancy 55
Fig 2. 9: Varied state of surface wettability. Hydrophobic to hydrophilic state from left to right 57

Fig 3. 1: Density profile of water molecules. 62
Fig 3. 2: EDLC scenarios (a) discharged state (b) charged state. 63
Fig 3. 3: Density profile of Cl^- for validated crumpled graphene model. 64
Fig 3. 4: Variation of Na^+ ion with for different spatial position 65
Fig 3. 5: Electrolyte ion tend to enter into the pore whereas solvents are moving towards the surface. 66
Fig 3. 6: Density profile of Cl^- for (a) r=89.5Å (b) 110.1 Å and (c) 165.4 Å crumpled states. 70

Fig 3. 7: Density profile of Na^+ ion for (a) r=89.5Å (b) 110.1 Å and (c) 165.4 Å crumpled states. 72
Fig 3. 8: Density profile of water for (a) r=89.5Å (b) 110.1 Å and (c) 165.4 Å crumpled states. 74
Fig 3. 9: Variation of EDLC thickness with different degree of crumpling state. 75
Fig 3. 10: Distribution of potential values with spatial distances at different crumpled states 76
Fig 3. 11: Distribution of specific capacitance with varied crumpled radius 77
Fig 3. 12: Simulation domain showing electrolyte ions accumulated in electrode surfaces. 78
Fig 3. 13: Density profile of Cl^- for different electrodes consisting varied amount of defects (in % of the surface area)..... 80
Fig 3. 14: Distribution of cations from different distance of electrodes consisting 5%, 10%, 20% and 30 % defects. respectively..... 81
Fig 3. 15: Similar pattern of water molecules accumulation near electrode surface for different defects levels. 81
Fig 3. 16: Free-Energy scenario with spatial position of different porous crumpled electrode.... 82
Fig 3. 17: Incrementation of Double layer thickness with increased amount of defects. 83
Fig 3. 18: Impact on Partition co-efficient for different levels of defects-based electrodes. 83
Fig 3. 19: Magnified views of electrodes consisting (a) 5% (b) 10% (c) 20% and (d) 30% defects. 85
Fig 3. 20:Greater potential drops for 20% defects-based electrode. 86
Fig 3. 21: Variation of Specific Capacitance with defects levels. Highest specific capacitance can be seen at 20% defects..... 87
Fig 3. 22: Density profile of Cl^- for different contact angles. 88
Fig 3. 23: Cations gathering up near cathode. Higher accumulation for hydrophilic surface. 89
Fig 3. 24: Lower density peak of H molecules for hydrophilic surface. 90
Fig 3. 25: Distribution of water-O solvent molecules as a function of contact angle..... 90
Fig 3. 26: Distribution of free energy with different surface wettability situations. 92
Fig 3. 27: Total potential distribution at different contact angles. 92
Fig 3. 28: Variation of EDL thickness with changed contact angles. 93
Fig 3. 29: Increased capacitance shown from hydrophobic surface to Hydrophilic surface. 94

List of Tables

Table 2. 1: Total number of bonds, angles, atom types, bond types, angle types and size of simulation cell 48
Table 2. 2: Dimension of Simulation domain 49
Table 2. 3: Atom types and their masses used in current study 50
Table 2. 4: Bond Co-efficients. 51
Table 2. 5: Pair Co-efficient of the atoms used in current model 52
Table 2. 6: Simulation domain for varied crumpled state 53
Table 2. 7: Number of atoms per electrode for different defect level 56
Table 2. 8: L-J parameter for different contact angle [114] 58

Table 3. 1 Comparison of performances for different electrode configuration 77
Table 3. 2 Variation of capacitance for different level porous electrode based EDLC 86
Table 3. 3 Various performance parameters summarized for different surface wettability. 95

Chapter 1

Introduction

1.1 General Introduction

Changing weather trends, depletion of fossil fuels, and unequal distribution of energy sources force us to turn to alternative, renewable energy sources to fulfill the world's ever-increasing energy demands. In order to harvest energy from the infinite but intermittent renewable energy sources such as wind, tidal, and sunlight, it is necessary to develop and actualize economical, efficient, and dependable energy storage technologies in order to cope with such a shifting energy paradigm. There are different energy storage devices available, but electrochemical energy storage technologies are the most viable, ecologically beneficial, and long-term clean energy solutions. Batteries, capacitors, and fuel cells are now the most widely used commercial energy storage systems. However, these devices have their own limitations for example, although batteries have a high energy density of around 180 Wh kg^{-1}, they have a low power capability which have ruled them out from many applications [1]. The potential solution of this problem is the usage of 'Electrochemical capacitors,' also known as supercapacitors or ultracapacitors. Because of its fast charge/discharge rate, prolonged life cycle, and high-power density, supercapacitors have received a lot of interest [2].

It is critical to evaluate these energy storage devices' capacities in terms of energy and power density based on their unit mass or volume. The Fig 1.1 known as Ragone plot is a good indication of the comparative study for the different electrochemical energy devices [1]. As seen from the Fig 1.1 supercapacitors are in the highest end with respect to the power density which allows them to be used in varied applications starting from Power electronics, large-scale vehicle applications, such as buses and subway trains etc. The problem that supercapacitors face is possessing low energy density. So, the key challenge is to increase the energy storage capacity of these devices while keeping its power density high. To increase energy density of electric double layer capacitor (EDLC), one type of supercapacitor, the capacitance needs to be increased. Researchers attempt to enhance the performance by using different electrode materials as it is the most prominent factor

behind the capacitance [3]. Graphene is the most widely used electrode material due to its high thermal and electrical conductivity while having a very high specific area [4]. Graphene based electrodes have shown excellent results in terms of energy storage. For instance. Vivekchand et al found capacitance of 135 F/g for graphene based electrode [5]. This result can be further improved by modifying the surface geometry of the electrode to a 3-D structure. Tarek et al recently explored a significant uprise in the capacitance with wrinkled flower like graphene structure [6]. This scenario paves the way of the emergence of crumpled graphene, a dense three-dimensional deformation of planar graphene. Recent published articles hold a very optimistic view regarding crumpled graphene used as electrode material as it can improve the interaction between electrode and electrolyte [7]. However, no prior atomistic simulation study has been conducted by incorporating crumpled graphene as electrodes of EDLC. Thus, this has been bygone of the major motivations for this thesis work.

So, the prime objective of this study was to discover energy storage capability of EDLC with crumpled graphene electrodes by conducting Molecular dynamics simulation (MD). Along with this, the effect of the surface geometry was explored by varying the degree of crumpling. Influence of surface geometry on the crumpled graphene was studied too by adding defects on the material. And lastly, another surface property, wettability was varied to visualize its effect on the EDLC performance.

After the results, it will be shown how crumpled graphene could improve the capacitance drastically because of the better surface accessible area for electrolyte ions in chapter 3. This study involves a very extensive effort to replicate a physical phenomenon occurring in EDLCs in the simulation and the EDLC modelling discussed in Chapter 2. Having said that, this research has a few limitations as well which are addressed in the chapter 4. The final goal of this thesis is to open a door for researchers who are tending to improve the energy density of supercapacitors so that the world can try to mitigate the problem of energy crisis, which is expected to be more prominent in the coming years.

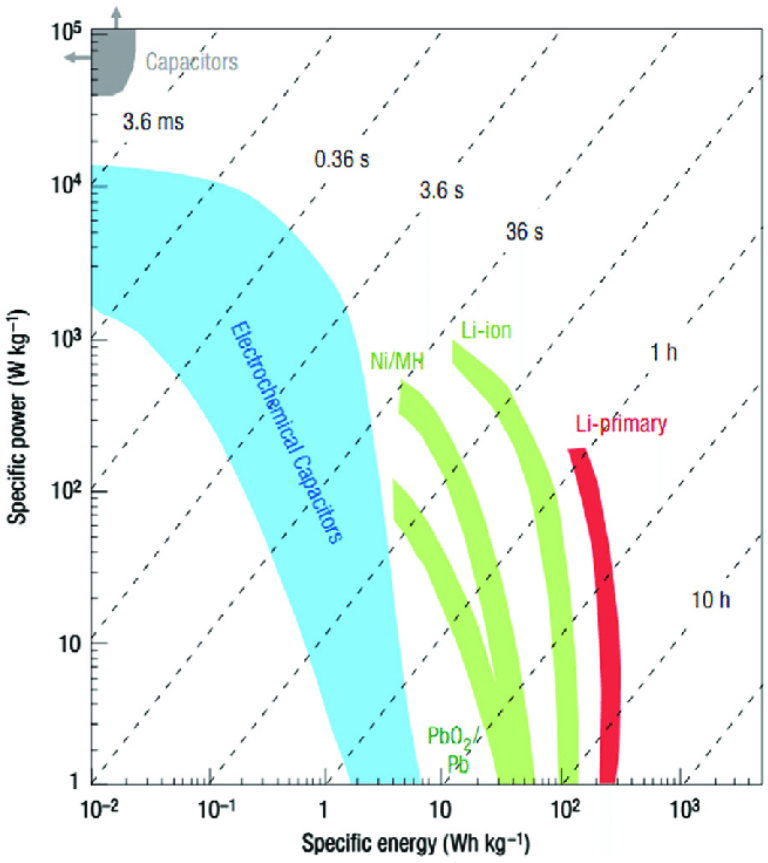

Fig 1. 1: Specific energy and specific power scenario for different energy storage devices [1]

1.2 Fundamentals of Supercapacitors

Supercapacitors are a unique type of capacitor that charges and discharges at the electrode-electrolyte interface of porous carbons or metal oxides with a large surface area. An electrochemical supercapacitor is constructed with two conducting electrodes separated by a dielectric membrane immersed in electrolyte solution which can be solid or liquid. The passage of ions is permitted by this dielectric membrane. The ions in the electrolyte are parted by an external electric field, and the opposite ions are drawn to the corresponding electrode. Supercapacitors can be classified into two main categories with respect to capacitive behavior: electrical double layer capacitance and pseudo-capacitance, which will be briefly explained in the following section.

1.2.1 EDLC Supercapacitor

Electrochemical double layer capacitors (EDLCs) can store charge electrostatically or by a non-Faradic method in which there is no charge transfer between the electrode and the electrolyte when the voltage is applied. Charge accumulates on the electrode surfaces, and because of the potential difference, opposite charges are attracted to each other. This results in ions in the electrolyte diffusing over the separator and into the pores of the opposite charged electrode shown in Fig 1.2. A double layer of charge is created at the electrode to prevent ion recombination. EDLCs can achieve better energy density thanks to the double layer, which is combined with an increase in specific surface area and shorter distances between electrodes. The capacitance of electric double layer capacitors is substantially determined by the electrode's surface composition, surface area, electrolyte types, and Debye length, where Debye length refers to the double layer's effective thickness.

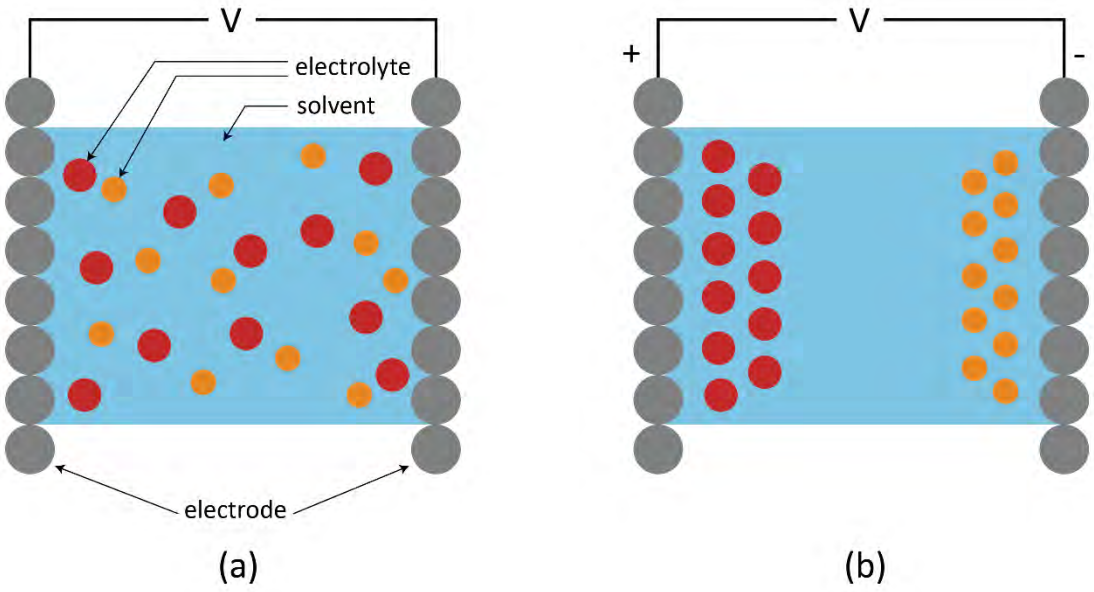

Fig 1. 2: Basic Structure of an EDLC (a) discharged state and (b) charged state.

The specific capacitance of EDLCs is represented by the following formula:

$$C = \frac{\varepsilon_r \varepsilon_0 A}{d} \tag{1.1}$$

where C is the capacitance of the EDLC, ε_r is the electrolyte's dielectric constant, ε_0 is the vacuum's dielectric constant, d is the effective thickness of the double layer, and A is the surface area of the electrode. The equation 1.1 shows that Capacitance is directly proportional to the surface area of the electrode. Therefore, optimization of the electrode surface is essential to enhance the performance of the supercapacitor. Advantages of this mechanism include very fast energy storing and delivery and also high stability of EDLCs during charge-discharge cycles.

1.2.2. Pseudocapacitors

Pseudocapacitors, unlike EDLCs, which store charge electrostatically, store charge via the Faradic process, which involves charge transfer between electrode and electrolyte (illustrated in Fig 1.3.) When a potential is applied to a pseudocapacitor, the electrode material undergoes reduction and oxidation, resulting in charge passage across the double layer and Faradic current traveling through the supercapacitor cell. The charges that collect in the electrode and the electric potential are inextricably linked in this action. Equation 1.2 can be used to express this relationship.

$$C = \frac{dQ}{dV} \tag{1.2}$$

where C is the capacitance of the pseudo-capacitor, Q denotes the charge quantity, and V denotes the potential. The capacitance of pseudo-capacitors is often substantially higher than that of EDLCs. However, this sort of capacitor is prone to low power density and instability. These issues arise as a result of poor electrical conductivity and the swelling of the framework as a result of cycling.

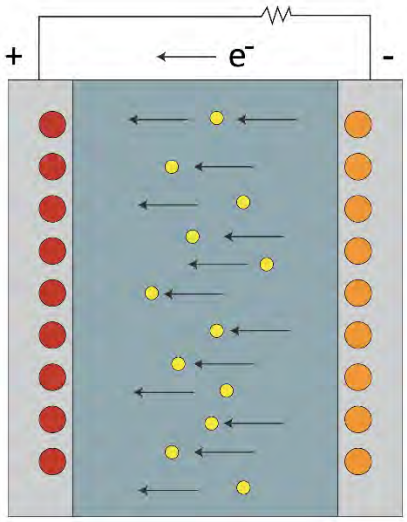

Fig 1. 3: Schematic diagram of Pseducapacitor.

1.3 Differences between Battery and Capacitors

The mode of energy storage is the primary distinction between supercapacitors and batteries. Chemical reactions that are placed in the electrodes that are oxidized or reduced, generating charges, are used to store energy in batteries. However, due to the creation of a double layer in the electrode/electrolyte interphase, supercapacitors store energy directly as electrostatic charge. The slow kinetics of the redox process in battery electrodes, as well as the limited mass transport of the reactants, typically limit battery power performance [8]. The creation of the double layer in supercapacitors is a quick process that results in high-power devices. Supercapacitors (SCs) or ultracapacitors, which have a substantially higher power density, longer shelf life, and cycle life than batteries, have emerged as a complementary energy storage technology to batteries, filling a niche in terms of specific power for high-power applications [9]. In fact, capacitors have a lower energy density than batteries, and the trade-off between high power delivery in a short period of time and energy density is a significant design concern. In this situation, SCs can fill the gap between batteries' large energy storage capacity and conventional capacitors' high-power capability.

1.4 Different Models of EDLC

There are different theories/models developed for the interface between solid electrode and liquid electrolyte in EDLCs. It's fascinating to see how the models have evolved over time, integrating more and more elements that reflect the interfacial structure. Significant Models will be discussed in the following section

1.4.1 Helmholtz Model

Charged electrodes immersed in electrolyte solutions repel ions of the same charge while attracting ions of the opposite charge to their surfaces, according to Hermann von Helmholtz. At the electrode-electrolyte interface, two layers of opposite polarity form. He established in 1853 that an electrical double layer (DL) is simply a molecular dielectric that retains electric charge statically. For simulating the spatial charge distribution at double layer interfaces, this theory is the simplest approximation.

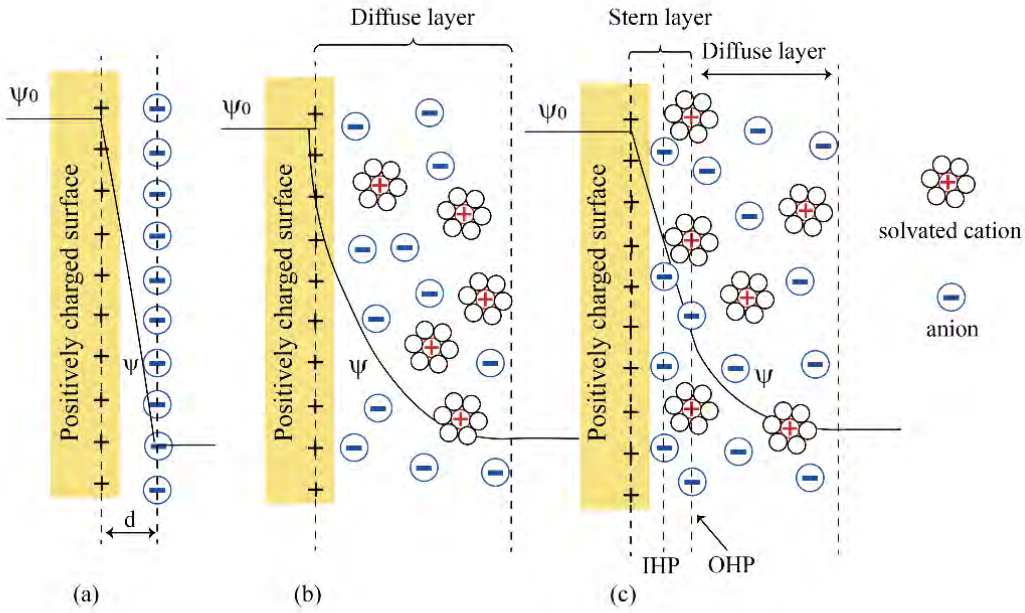

Fig 1. 4: Different Models of EDLC. (a) Helmholtz model (b) GC model (c) Stern Model.

At a distance from the solid, opposite sign ions neutralize the charge of the solid electronic conductor. This is the distance between the surface and the ion's core. The breakdown voltage of the electrolyte in the stored condition is linearly dependent on the voltage applied, as illustrated in Fig. 1.4. The distance of closest approach of the charges, that is, the ionic radius, would be X_H in this case, and the charges would be considered as point charges for the sake of the computation. By analogy with a capacitor the capacity would be

$$C_{d,H} = \frac{\varepsilon_r \varepsilon_0}{X_H} \tag{1.3}$$

where ε_r is the relative permittivity, which is believed to be constant throughout distance, and ε_0 is the vacuum permittivity.

This early model predicted a constant differential capacitance independent of charge density based on the dielectric constant of the electrolyte solvent and the thickness of the double-layer, and while it provides a good foundation for the description of the interface, it ignores several important factors such as ion diffusion/mixing in solution, the possibility of adsorption onto the surface, and the interaction between solvent dipole moments and the ions in solution. As of now, this is regarded as the most basic theory, although it still fails to adequately describe natural phenomena.

1.4.2 Gouy-Chapman or Diffuse Model

Capacitance was not a constant, according to Louis Georges Gouy in 1910 and David Leonard Chapman in 1913, and it relied on the applied voltage and ionic concentration. According to Gouy, a liquid surrounding a charged solid has an equivalent amount of opposite ionic charge, but the ions are not securely bound to the surface [10]. These ions in solution tend to diffuse into the liquid phase until their departure creates a counter-potential that prevents diffusion. The thickness of the diffuse layer will be determined in part by the kinetic energy of ions in solution. By adopting a diffuse model of the double layer, Gouy and Chapman generated theories with significant improvements, Maxwell-Boltzmann statistics can be applied to the charge distribution of ions as a function of distance from the metal surface in this model. As a result, the electric potential diminishes exponentially as one moves away from the fluid bulk's surface. For highly charged

double layers, this model fails [11]. The thickness of double layers measured experimentally is larger than the expected thickness.

1.4.3 Stern Model

The Gouy-Chapman model is closer to reality than the Helmholtz model, although its quantitative applications are limited. For strongly charged DLs, the Gouy-Chapman model fails. It presupposes that the ions are point charges that can freely reach the surface, which is not the case. Otto Stern proposed integrating the Helmholtz and Gouy-Chapman models in 1924. Some ions cling to the electrode, as indicated by Helmholtz, forming an internal Stern layer, while others form a Gouy-Chapman diffuse layer, according to Stern's concept. Stern amended the Gouy-Chapman model by claiming that ions have a finite size, hence limiting their approach to the surface. As a result, the Stern layer accounts for the ions' finite size, and an ion's closest approach to the electrode is on the order of the ionic radius [3]. The Gouy Chapman model implies that the first ions are at a distance from the surface, whereas the Stern model assumes that there can be precisely surface-adsorbed ions in plane, which is known as the Stern layer. Within this so-called compact layer, ions are strongly adsorbed by the electrode. Specifically adsorbed ions (forming the inner Helmholtz plane) and nonspecifically adsorbed counter-ions (forming the outer Helmholtz plane) are found in the compact layer in Fig 1.4 [12]. The thinner the diffuse layer, like in the Gouy-Chapman model, the less important the thickness of the diffuse layer is, and the faster the potential drops. The transition from the compact to the diffuse layer occurs at distance X_H. The outer Helmholtz plane is the plane that separates the two zones. This is comparable to two capacitors connected in series, with capacity C_H representing the stiff compact layer and CGC representing the diffuse layer in mathematics. The observable behavior is determined by the smaller of the two capacities:

$$\frac{1}{C_d} = \frac{1}{C_H} + \frac{1}{C_{GC}} \tag{1.4}$$

To address the limitations of the Gouy-Chapman model for the diffuse layer, Stern proposed combining the two prior models, resulting in an inner Stern layer (e.g., the Helmholtz layer) and an outer diffuse layer.

1.5 Characterization of EDLC Performance

A set of important metrics such as cell capacitance, operating voltage, equivalent series resistance, power density, and energy density are used to evaluate the performance of a supercapacitor (SC). Energy density and power density are denoted by E, in Watt-hours per unit mass or volume and *P,* in Watts per unit mass or volume respectively [13]. The expression of E and P are given as:

$$E = \frac{1}{2} C_T V^2 = \frac{QV}{2} \tag{1.5}$$

$$P = \frac{V^2}{4R} \tag{1.6}$$

where V (in volts) is the operating voltage, Q (in volts) is the total charge stored in the electrochemical supercapacitor (ES), CT (in F) is the cell's total capacitance, and R (in volts) is the Equivalent series resistance (ESR). Increasing CT and/or V increases the energy density of the electric double layer supercapacitor, as shown in eqns. 1.5 and 1.6.

According to eqn. 1.6, EDLCs have a comparatively high-power density due to the low ESR caused by the absence of charge adsorption and desorption between the electrode and the electrolytes. On the other side, the energy density of EDLCs is smaller. Because V is set for an electrolyte, the only way to raise E is to increase CT, which may be calculated using the equation below.

$$\frac{1}{C_T} = \frac{1}{C_A} + \frac{1}{C_C} \tag{1.7}$$

where C_A and C_C are the capacitances of the anode and cathode, respectively. Eqn. 1.7 indicates that it is desirable to increase C_A and C_C simultaneously to avoid limiting the total cell capacitance by the electrode. The ES can be classified as symmetric or asymmetric depending on the values of CA and CC. Both electrodes' materials and capacitance will be the same in symmetric ES, i.e., Ca = Cc. As a result, the total capacitance (CT) of both devices will be halved. Materials, as well as capacitance, will be different for the anode and cathode electrodes in asymmetric ES. In this instance, the electrode with the smaller capacitance will dominate the total capacitance. Numerous attempts have been made to accurately explain the capacitance of carbon materials in terms of pore

structure and size, as well as the specific character of their interaction with electrolytes. The classic paradigm is utilized for mesoporous carbons with cylindrical pores shown in Eqn. 1.8 [14] :

$$\frac{C}{A} = \frac{\varepsilon_r \varepsilon_0}{b \ln(\frac{b}{b-d})} \tag{1.8}$$

where d is the distance between the ion and the carbon surface and b is the pore radius. Because the ions are supposed to line up in the middle of a cylindrical pore in micropores, the capacitance is computed as follows in Eqn. 1.9 [14] :

$$\frac{C}{A} = \frac{\varepsilon_r \varepsilon_0}{b \ln(\frac{b}{a_0})} \tag{1.9}$$

where a0 is the ion's effective size. This ionic radius was discovered to be near to that of the bare ion, implying that the ions might be totally de-solvated.

In general, electrode materials appear to be the primary determinant of capacitance and stored charge. The ES voltage (V) and thus capacitance develops across the electrodes as a result of a charging process, the value of which is determined by the electrolyte and electrode materials. According to the equation 1.5, energy density is directly proportional to the capacitance of the supercapacitor. Optimizing the electrode surface designs as well as the materials that make up the electrode can result in higher capacitance which can overcome the present problem of ES which is the low energy storage capacity. Therefore, this research was performed in accordance to this need.

1.6 Advantages of EDLC Supercapacitors

When compared to batteries, electrochemical supercapacitors (ES) have various advantages. The following are a few of them:

- High Power Density: When compared to lithium-ion batteries, ES have a substantially higher power delivery (1–10 kW kg^{-1}) than lithium-ion batteries (150 W kg^{-1}). The charging-discharging process in supercapacitors is much faster than in batteries, resulting

in a high-power density [1]. The ES retains electrical charges both at the electrode surface and in the bulk near the surface of the solid electrode, which explains why it charges and discharges quickly.

- Longer Life expectancy: Electrochemical supercapacitors can withstand a large number of charge-discharge cycles (up to 1000000), with no maintenance required during their lifetime. Furthermore, ES can run for 500000–1000000 cycles at high speeds with just little changes in their features [15]. Even if the depth of discharge is only 10–20 percent of the total energy, such longevity is unattainable for batteries. ES batteries have a life expectancy of up to 30 years, which is significantly longer than lithium-ion batteries [16].
- High Efficiency: Because of the reversible behavior during charging-discharging across the whole operating range of voltage, one of the key advantages of ES is that heat loss management is easy. As a result, the energy loss and heat loss while charging and discharging for ES are very low and may be easily removed. For example, even at rates above 1 $kWkg^{-1}$, ES has been observed to have a high cycle efficiency (about 95%) [17].
- Wider temperature Range: Extremely high and low temperatures are not a problem with ES. The operating temperature for ES is typically between -40 and 70°C.

Fig 1. 5: Electric bus powered by Li-ion battery with support of supercapacitor [18].

This is beneficial for military applications, where reliable energy storage is necessary to power proprietary electrical gear in all temperatures during a battle.

- Environment friendly: non corrosive and non-toxic material and electrolyte are generally selected to model a commercial supercapacitor. So, it is considered environment friendly.

1.7 Application of Supercapacitor

Instead of long-term compact energy storage, supercapacitors are typically utilized in applications requiring multiple quick charge-discharge cycles. However, the early commercialization of electrochemical capacitors for computer memory backup has lately expanded to include uses for transportation and large-scale energy conservation [19]. They're employed for regenerative braking, short-term energy storage, and burst mode power delivery in cars, buses, trains, cranes, and elevators shown in Fig 1.5 [20]. They can also enhance fuel efficiency by storing energy during braking and then releasing it as the vehicle accelerates. Automobiles driven by a combination of fuel cells and supercapacitors are perfect for stop-and-go traffic, as the supercapacitors give quick bursts of energy while the fuel cells provide long-term energy. Supercapacitors are also compact, lightweight, and function well at extremely low temperatures (–40°C).

Supercapacitors are commonly employed as backup energy sources in consumer electronics for system memories, microcomputers, system boards and clocks, toys, and mobile phones. They're great for gadgets that need to charge quickly. Because supercapacitors have extraordinarily long lifetimes and do not require replacement during the lifetimes of the devices they power, they are a cost-effective solution.

In UPS systems, supercapacitors can be utilized for temporary backup power. They can deliver power instantly and without delay, preventing mission-critical applications from malfunctioning. Supercapacitors are used to swiftly bridge the power gap in stationary UPS systems with fuel cells. Furthermore, supercapacitors are the ideal choice for providing power during startup and peak load buffering.

Hospitals, financial centers, airport control towers, and mobile phone towers could all benefit from supercapacitors. Because supercapacitors generate power within milliseconds to a few seconds

after a power failure, they can effectively bridge the critical interval between a power outage and the start of a generator.

1.8 Limitations of EDLC Supercapacitors

Commercial supercapacitors have a lower energy density (approximately 5 Whkg-1) than batteries (>50 Whkg-1), as well as a high self-discharge rate and a high cost. Supercapacitors cannot compete with batteries in terms of cost in terms of $/Wh, but they can compete in terms of $/kW. Batteries have a lower energy density (1-2 $/Wh) than supercapacitors, which have a higher energy density (10-20 $/Wh) [21]. The cost of electricity from supercapacitors (25-50 $/kW) is, on the other hand, less than half that of power from batteries (75-150 $/kW) [22]. Electrochemical capacitors have been rejected in a variety of applications due to their high energy cost. In addition to that, ES has a concerning practical constraint in the form of its high self-discharge rate. It has a high discharge rate of 10–40 percent each day and a short lifespan for particular applications [23]

1.9 Review of Germane Work

Performance of Supercapacitor largely depends on the interaction between the electrode and electrolyte interaction. EDLCs make use of the interface's quick reaction to changes in electrode potential and the formation of high reversibility. Pseudocapacitors, on the other hand, are devices that use the electrode charge storage phenomenon in conjunction with highly reversible Faradaic electrochemical redox surface processes. As a result, the electrode materials required for supercapacitor applications varied depending on the underpinning mechanisms in each category. High surface area carbons have been the primary materials used in EDLCs, whereas oxides such as ruthenium and manganese oxides have dominated pseudocapacitor research [1]. To improve device performance in industrial and large-scale EDLC applications, rational tuning of electrode–electrolyte interactions is critical. Customizing electrode materials, such as designing pore geometry/size and doping defects/functional groups, is one of the most effective approaches [24],

[25]. The ideal materials should be plentiful and inexpensive, should have large specific surface areas and great conductivity, should be nontoxic and environmentally acceptable, and are simple to produce [26]. Carbon materials are therefore one of the most promising electrode materials [27].

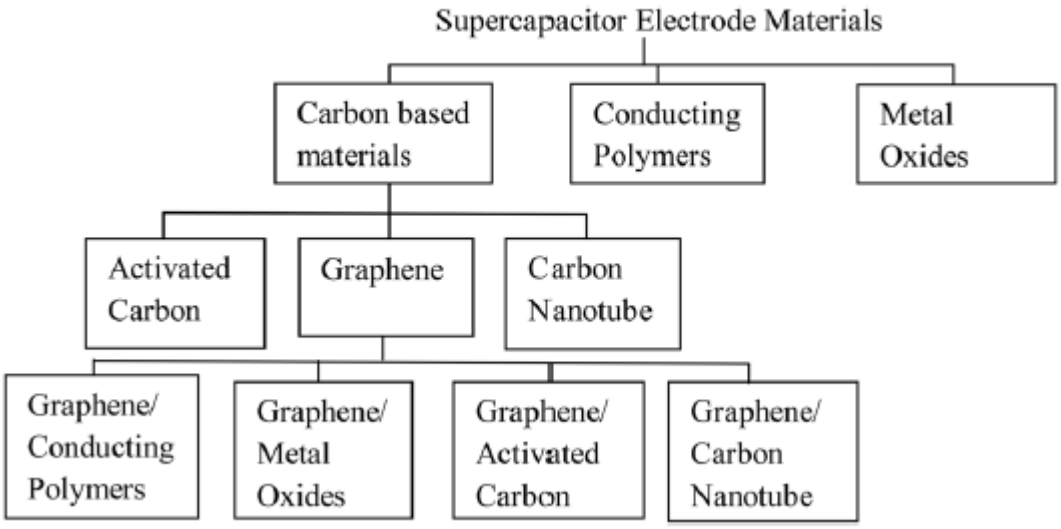

Fig 1. 6: Taxonomy of supercapacitor materials [3].

Fig 1.6 shows taxonomy of electrode materials. In the following section, previous studies of different electrode material and their influence on the EDLC performance is discussed.

1.9.1 Usage of Porous Materials as Electrode

Due to its low cost and large specific surface area of 3000 m^2 g^{-1}, Activated Carbon (AC) has recently become one of the most extensively utilized porous materials in commercial applications as supercapacitor electrodes [15]. Because of the difficulty to construct meaningful numerical model due to the complexity of its structure, a very few MD simulations have been carried out on AC. Coconut shell AC (CSAC) is a unique instance in which the majority of the pores are micropores, which is a good pore size range for MD simulations. The Reverse Monte Carlo procedure was used by Rajput et al. to create a CSAC numerical model and compare it to an

electrode material with homogenous pore size [28]. The importance of heterogeneous pore size and shape, as well as the complex morphology, was revealed using this method. The majority of commercially accessible devices use activated carbon electrodes and organic electrolytes, with an operable cell voltage of 2.7 V, a specific capacitance ranging from 100–120 F g^{-1}, and a volume of up to 60 F cm^{-3} [29]. Low-cost carbon-rich biochar of red cedar claims to achieve a gravimetric capacitance of 115 F g^{-1} in aqueous electrolyte, making it a suitable choice for mass manufacturing [30]. Many researchers have established relationships between capacitance performance and the nanoporous structure of ACs using different electrolytes and increased specific capacitance. Because organic electrolyte ions are larger than those in water-based electrolytes, the capacitance of aqueous electrolytes (100–300 F/g^{-1}) is higher than that of organic electrolytes (150 F/g^{-1}) [15]. Apart from AC, Carbide-Derived Carbons (CDC) have been used extensively as an active electrode material. Titanium CDCs have the best gravimetric capacitance in KOH (up to 220 F g^{-1}) and organic electrolyte (up to 120 F g^{-1}), whereas SiC-CDCs have the highest volumetric capacitance in KOH (up to 126 F cm^{-3}) and organic electrolyte (up to 72 F cm^{-3}) [31]. Merlet et al. were the first to use MD simulations to quantify the phenomena of room-temperature ionic liquid (RTIL) ions situated in a numerically generated CDC structure [32]. The capacitance value (125 F g^{-1}) determined from their computational work matches the experimental data and is higher than simple planar structures. The microstructure of sub-nanometer pores can influence energy storage dynamics. As illustrated in Fig. 1.7, Merlet et al. investigated the confinement effect for four types of adsorption locations on the edge: planar, hollow, and pocket sites [33]. With increasing confinement, they discovered an increase in desolvation and stored charge (DoC). To penetrate the small pores of CDCs, solvated ions must be partially stripped of their hydration shells, resulting in additional charges being accommodated inside very constricted holes resulting in enhancement of the capacitance

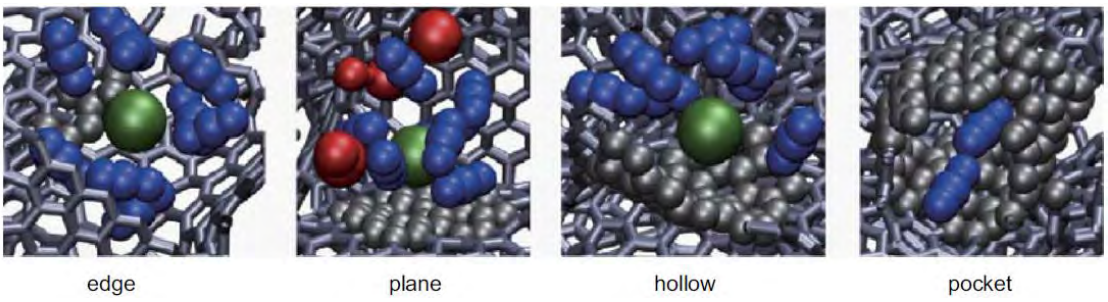

Fig 1. 7: Four typical structure for adsorption location [33].

1.9.2 Investigation on 0-D and 1-D Materials as EDLC Electrode

New graphitic carbon nanomaterials with multi-dimensions, such as dimensionless (0D) fullerene, one-dimensional (1D) carbon nanotubes (CNTs) [34]–[36], and two-dimensional (2D) graphene sheets, have been created as a result of recent advancements in nanoscience and nanotechnology [37]–[39]. CNTs and graphene has been substantially studied in the field of supercapacitor electrode material because of outstanding mechanical and electrical property.

CNT can be divided into single-walled carbon nanotube (SWCNT) and multiwalled carbon nanotube (MWCNT) based on the number of graphitic sheets (MWCNT). CNTs are suited for supercapacitor electrode fabrication, whether in their pure form or when combined with other electrode materials. Pure carbon nanotubes have been reported to have a specific surface area of 120–500 m^2 g^{-1} and a specific capacitance of 2–200 F g^{-1} [40], [41]. Their specific surface area is often less than 500 m^2 g^{-1}, which limits their use as high-capacitance electrodes [42]. Recent researches have looked into enhancing the surface area of by activating the walls of CNTS. For example, Pan et al. used electrochemical activation to enhance the specific surface area of SWNTs from 46.8 to 109.4 m^2 g^{-1}, resulting in a twofold increase in specific capacitance [43]. Feng et al. studied the capacitance of a closed CNT and discovered that as the radius drops from 1 nm to 0.4 nm, the capacitance increases constantly [44]. Shim et al. used the MD approach to investigate the double-layer capacitance effect for electrified CNTs of various diameters [45]. The capacitance versus diameter curve generated is congruent with the experimental data. The ion dynamics of solvent molecule and electrolyte ions with CNT electrode has been studied. Kalugin et al. examined the dynamics of ACN molecules inside the inner region, and their findings revealed a monotonous increase in self-diffusion coefficient with increasing internal diameter [46]. Water molecules, on the other hand, display a non-monotonic relationship of diffusion coefficient on radius [47].

To take advantage of their synergistic effects, researchers are presently working on developing flexible carbon fiber (CF) hybrid electrodes (CF-CNT). Xiong et al.used electrophoretic deposition and chemical vapor deposition to manufacture reduced graphene oxide (rGO)-CNTs on CF [48]. The specific capacitance of the reported composite was 203 F/g^{-1}, which is four times higher than

pure CF. Onion-like Carbon (OLC) too has been considered as a potential electrode material for supercapacitors. To demonstrate the curvature effect, Feng et al. investigated the capacitive effect in OLCs with radii ranging from 0.356 to 1.223 nm [49].

1.9.3 Graphene and Crumple Graphene Electrodes

Graphene is a carbon allotrope made up of a single layer of carbon atoms (2D) organized in a honeycomb lattice in two dimensions. Graphene is a two-dimensional structure made up of individual layers of graphite. Each layer of graphene has an interplanar distance of 3.35Å, with a C-C bond length of 0.142nm. In graphene, each carbon atom has sp^2 hybridization: three σ−bonds and one π−bond. The electron cloud may freely migrate and this is responsible for graphene's outstanding electrical conductivity. Graphene has a higher electrical and thermal conductivity than most metals.

Wide potential windows, a large number of functional groups with a huge surface area, and outstanding thermochemical stability, processability, and electrical performance have all been explored, making graphene an appealing candidate for energy devices [50]. The high specific area (2630 $m^2\ g^{-1}$) of graphene sheets has piqued interest as a material for energy storage devices like Supercapacitors and batteries [4]. This accessible surface area is significantly more than that of black carbon (900 $m^2\ g^{-1}$) and carbon nanotubes (50–1315 $m^2\ g^{-1}$) [51]. Zhang et al. demonstrated that graphene is an efficient microwave absorber [52]. The highly oxidized graphite structure exhibited a flat surface with a specific area of 415 m^2g^{-1}. At a scan rate of 5 mVs^{-1}, a specific capacitance of 185 Fg^{-1} was achieved. Stoller et al. constructed a 705 m^2g^{-1} graphene with a chemically modified surface area [53]. Using both cyclic voltammetry and galvanostatic charge/discharge calculations, average specific capacitances of 135 to 82 Fg^{-1} for aqueous and organic electrolytes were measured. Specific capacitances of 75, 135, and 99 Fg^{-1} were observed in graphene-based supercapacitors utilizing ionic liquid electrolytes, aqueous electrolytes, and organic electrolytes, respectively [5].

The energy and power density of EDLCs are significantly affected by controlling surface shape and designing pore structure in graphene. Surface roughness, for example, has a significant impact

on energy storage and charge dispersion. Surface roughness works by creating sub-nanometer pores or increasing the number of pores on the surface. Atomically corrugated surfaces have a greater capacitance than flat surfaces for practically all electrode potentials, as demonstrated by Vatamanu et al [54]. A corrugated surface, in particular, has about double the capacitance of a flat surface near the potential of zero charge (PZC). Furthermore, reasonable surface roughness design could maximize energy storage behavior. Xing et al. compared an atomically flat surface to two corrugated surfaces with varied degrees of nanopatterning [55]. The capacitance of a corrugated surface with a small groove width increased significantly, whereas the capacitance of a corrugated surface with a big groove width was found to be roughly equivalent to that of a flat surface. When the groove width approaches the diameter of electrolyte ions, the most efficient energy storage occurs. Incorrect surface roughness, on the other hand, could cause a slight increase in capacitance or even harm the energy density. Temperature and ion types have also been found to affect the capacitance and morphologies of the C–V curve for corrugated surfaces [56]. According to Vatamanu et al studies.'s, the influence of voltage and temperature on capacitance appears to be substantially stronger for corrugated surfaces. New theoretical models for sub-nanometer pores have been proposed as a result of MD investigations that have advanced our understanding of EDL microstructures and energy storage mechanisms [57]. The introduction of heteroatoms or functional groups into the structure of a carbon monolayer is referred to as the doping effect. For energy storage applications, doping graphene with heteroatoms can increase its electrical/electrochemical characteristics [58]. Jeong et al. used a simple plasma technique to make N-doped graphene, which has a specific capacitance of 280 F g1, which is 4 times larger than the similar undoped pristine graphene [58]. Investigations on doping effect towards EDLC characteristics have been illustrated by MD and DFT method. Paek et al. ran simulations on two types of nitrogen-doped structures, N1 and N3V and found that their overall capacitances were significantly larger than the pure graphene layer [59]. The EDL capacitances and structures suffer when oxygen-containing functional groups are doped. The most frequent oxygen functional groups in graphene layers are hydroxyl and epoxy groups, which are formed during the oxidation process. According to the research of Kerisit et al. , hydroxyl groups cause a faster drop in capacitance than epoxy groups [60]. However, according to Xu et al findings.'s, the effects of both hydroxyl and epoxy are similar [61].

Since the discovery of the abnormal increase in capacitance inside subnanometer pores by Chmiola et al. , size effect, or confinement effect, in graphene-based electrodes has gotten a lot of attention [62]. The confinement effect may cause electrolyte ions to lose their dynamic properties. Ions in different layers are subjected to varying degrees of confinement, resulting in distinct local dynamical behaviors as the distance between the ions and the wall changes. As they approach the walls of slit pores, the dynamics of RTIL ions are weakened. When the confinement effect is increased, the overall dynamics of confined ions are greatly attenuated, according to a simulation study [63]. This observation is in line with the findings of Salemi et al. [64]. Ion dynamics that are less dynamic may result in a slower charging rate and a longer charging time for slit pores.

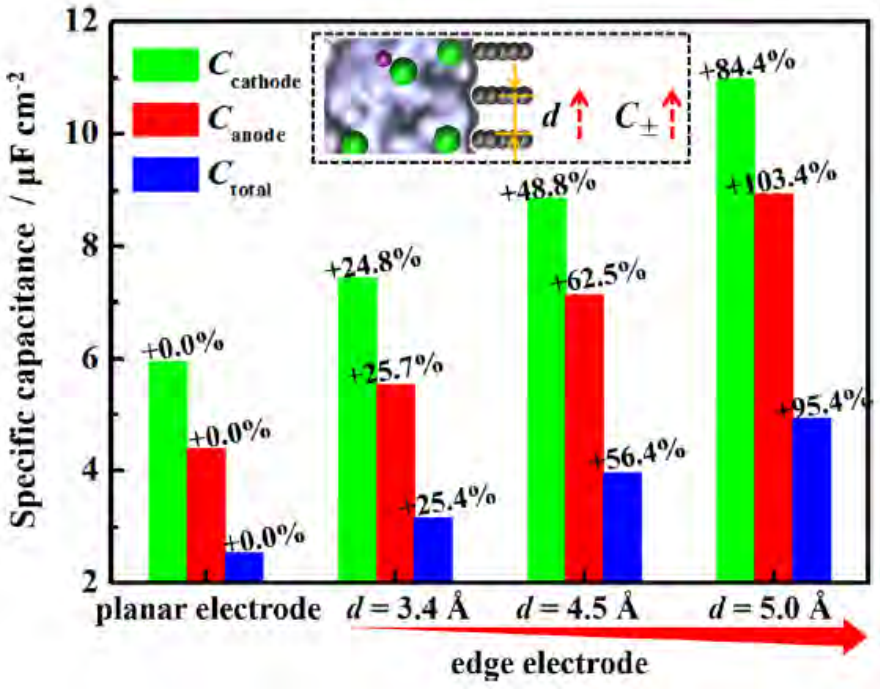

Fig 1. 8: Specific capacitance of planar and edge electrode [65].

Kondrat et al. compared a broader (0.66 nm) and a smaller (0.53 nm) pore and discovered that the wider pore charges faster than the narrower pore [62]. More ions are adsorbed in a narrower pore, yet there are limited paths for co-ions to leave the pore (primarily the process of counterion adsorption), resulting in the overfilling phenomena.

It appears that reducing the pore size can reduce the charging rate. Despite a higher supercapacitance for narrower pores, this affects the efficiency of EDLCs to some extent.

Graphene's edge region is made up of multiple single-atom graphitic lines, as well as numerous defects and dandling bonds. This region may aid in ion separation, resulting in efficient energy storage. The specific capacitance of the edge region is 4 orders of magnitude higher than that of the basal region, according to experimental studies [66]. Pak et al. completed modeling work on the edge effect of monolayer graphene [67]. The capacitances of virgin graphene and edge-functionalized graphene are compared in this study. Yang et al. examined the capacitive performance of planar electrodes and multilayer graphene edges with varied interlayer spacings shown in Fig 1.8 [65]. The multilayer graphene edges had a larger capacitance than the planar electrode (approximately a two-fold increase at 5.0 Å), according to their findings.

Recent advancements in the fabrication of graphene–polymer/ graphene-metal oxides composites highlight the materials' potential for Supercapacitor applications. Manganese dioxide (MnO_2) has been identified as a suitable supercapacitor electrode material due to its inexpensive cost, increased electrochemical activity, and non-toxic nature. The maximum capacitance and energy density recorded at a scan rate of 0.01 Vs^{-1} were 542 Fg^{-1} and 75.3 $Whkg^{-1}$, respectively, due to the extraordinary electrical conductivity of graphene nanoparticles and high pseudocapacitance of MnO_2 nanoparticles [68]. Yan et al. used microwave irradiation to self-limit the deposition of nanoscale MnO2 on the surface of graphene, resulting in graphene–MnO_2 composites [69]. The specific capacitance value was 310 Fg^{-1} at 2 mVs^{-1} in this composite. This could be owing to MnO_2's enhanced effective interfacial area with the electrolyte, as well as its high conductivity and contact area with graphene. RuO_2/Graphenes composite supercapacitor electrode possess the maximum specific capacitance of 570 Fg^{-1} [70]. However, due to the high cost of Ru, the use of RuO_2 as an electrode material in supercapacitors has been limited. Through in situ polymerization of pyrrole in the presence of Graphene Quantum Dots (GQD) solution, Kun et al. successfully synthesized a nanocomposite of polypyrrole and graphene quantum dots [71]. The maximum specific capacitance value of 485 Fg^{-1} was achieved at 5 mVs^{-1} for the mass ratio of polypyrrole to GQD (50:1). With a maximum specific capacitance of 650 Fg^{-1}, a highest energy density of 54 $Whkg^{-1}$, and a highest power density of 778.1 Wkg^{-1}, the graphene/polypyrrole based supecapacitors showed interesting performance. Tayel et al. presented a supercapacitor with high

porosity and large surface area graphene/PANI electrode materials [72]. Khosrozadeh et al. revealed that a supercapacitor with polyaniline, graphene, and silver nanowire electrodes can achieve a specific capacitance value of 73.4 Fg 1 at a discharge rate of 1.1 Ag 1[73]. It has a power density of 468.8 Wkg 1 and a density of energy of 5.1 Whkg 1. Rakhi et al. examined graphene nanosheets mixed with tin oxide nanoparticles packed multi-walled carbon nanotubes (MWCNT) as supercapacitor electrode materials [74]. For this electrode material, the specific capacitance, power density, and energy density were 224 Fg^{-1}, 17.6 $kWkg^{-1}$, and 31 $WhKg^{-1}$, respectively. 453 Fg^{-1}, 62.96 $Whkg^{-1}$, and 566.6 Wkg^{-1} were the specific capacitance, energy density, and power density, respectively. Zheng et al. developed a graphene/activated carbon composite as a supercapacitor electrode material [75]. The packing density of the composite, which is more favorable for practical applications than graphene and activated carbon, is much higher. Yu et al. used hydrothermal treatment of graphite oxide to make a KOH activated carbon/graphene composite [76]. The use of KOH to increase the specific surface area of carbon compounds is very effective. This composite shows improved electrochemical performance when used as electrodes in a supercapacitor.

A flat two-dimensional crystal structure characterizes an ideal graphene sheet. Various investigations have shown that when two-dimensional crystals experience structural deformations, they achieve stability by limiting their total free energy. Depending on their height and aspect ratio, these structural deformations are characterized as ripples, wrinkles and crumples [77].Crumples are dense three-dimensional deformations [78]. Crumpled graphene is a dense deformation of a graphene sheet that occurs isentropically (folds and wrinkles). Multi-directional compressive force is the cause of this compact deformed structure. Mechanical parameters such as tensile strength, young's modulus, and the number of layers all influence deformation. Most crucially, we can control and adjust graphene's physical properties such as wettability, transmittance, chemical potential, and conductivity by regulating the degree of deformation.

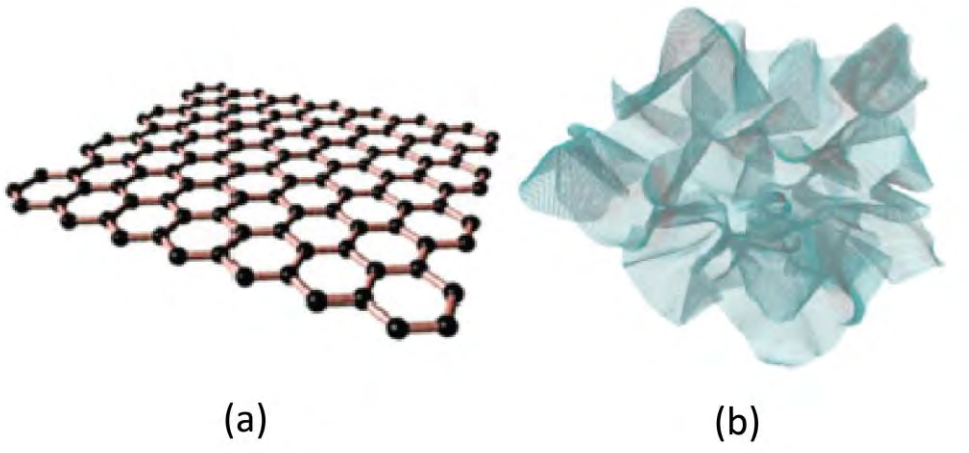

Fig 1. 9: Schematic diagram of (a) graphene and (b) crumpled graphene [77].

Figure 1.9 shows a structural diagram of the crumple graphene. Luo et al. used an aerosol aided capillary compression technique to crumple GO sheets [79]. Rapid evaporation of GO droplets causes them to shrink as a result of the high temperature, resulting in crumpled GO nanostructures that resemble crumpled paper balls. Crumpled graphene sheets have piqued researchers' interest due to its various features, and so find use in energy-related devices, particularly in areas where high specific surface area (SSA) is required. The effect of structural deformations on various attributes has been studied both theoretically and experimentally. The SSA of flat GO sheets was less than 5 m^2/g, whereas the SSA of crumpled GO sheets was 82 m^2/g, showing that the crumpled structure gives a larger surface area, which is one of the most significant criteria for developing graphene-based supercapacitor electrodes [79]. Tang et al. crumpled graphene using an aerosol spray technique with a combination of GO sheets and KOH and then exposed it to thermal reduction, whereas the crumpling process was explored using an aerosol spray technique with water as the medium [80]. While there has been a lot of research on crumple morphology at high temperatures, there have been few investigations on crumple development at extremely low temperatures below 0 °C. As the temperature decreased, the amount of crumpling appeared to rise. According to Semat et al. crumpling at – 80 °C was greater than crumpling at – 40 °C and – 20 °C [81].

Crumpled spheres made from L x L-diameter thin sheets follow the fractal scaling law $\rho_a L^2 \sim R^D$, where $\rho_a = \rho_V h$ is the areal density, h is the thickness (where h << L), V is the material mass density, R is the crumpled sphere's radius, and 2 <D< 3 is the crumpled spheres' material-dependent fractal dimension [82]. To evaluate the possible capacitance of graphene-based ultracapacitors, Steven et. al investigated the packing efficiency and accessible surface area of crumple graphene [83]. The solvent accessible surface area (SASA) is estimated for crumpled configurations, and by linking crumpled geometry to specific capacitance, authors predict a crumpled graphene specific capacitance of 329±45.6 F/g, which is highly dependent on the confining volume. Becton et al. performed a molecular dynamics simulation to explore confinement-induced crumpling of nanosheets of graphene [84]. During the mechanical confinement of graphene sheets, the crumpling behaviors observed when modifying the initial parameters of graphene composition, system temperature, rate of crumpling, and geometry were investigated.

Carbon materials with a 3D porous structure are known to aid ion transport and are hence highly recommended for the production of electrodes for electrochemical capacitors. The electrode material's SSA is determined by its porosity, and the electrode material's capacitance is determined by the pore size of the electrode. Tang et al. found that KOH activated crumple structures had both micropores and mesopores, with micropores accounting for 41.5 percent of total SSA and mesopores accounting for 56.3 percent [80]. There have been various attempts to boost graphene's SSA in order to use it as an electrode material for supercapacitors. Manipulation of the graphene sheet morphology into crumpled forms to avoid restacking is one of them. Wang et al. also used hydrothermal techniques to add Carbon Nano Tubes (CNTs) as interlayer spacers to graphene sheets in various ratios of Graphene and CNT. At a 1:1 ratio of graphene and carbon nanotubes, the maximum capacitance of 318 F/g was discovered (Fig. 20). This result appears to be consistent with crumpled graphene's theoretical value [85]. Crumpling the 2D structure into 3D paper ball structures that are aggregation-resistant is the most viable way for increasing surface area. According to the BET research, virtually wrinkled sheets have an SSA of 66 m^2/g, whereas crumpled sheets have an SSA of 255 m^2/g, resulting in increased capacitance [86].

Apart from electrode materials, various electrolyte has made substantial effects on the performance of supercapacitors. In the following section the studies on effects of electrolyte on EDLC performance is summarized.

1.9.4 Effects of Electrolytes on the Performance of EDLC

The electrolyte is one of the most important components in determining the performance of any electrochemical energy system. A wide range of electrolytes, such as aqueous electrolytes, organic electrolytes, Ionic Liquid (IL) electrolytes, redox-type electrolytes, and solid or semi-solid electrolytes, have been investigated and significant progress has been made in the last few decades. Using neutral aqueous electrolytes, for example, the operating potential window of aqueous electrolyte-based Supercapacitors has been reported to be considerably increased to 2 V [87]. In comparison to commercial organic electrolytes, a large range of new organic electrolytes with wider working potential windows and lower toxicity have been created for electrochemical capacitors. Despite the accompanying problems, such as limited ionic conductivity and excessive viscosity, the operating cell voltage was increased to 4 V for the creation of IL electrolytes [88]. Aqueous electrolytes often have a conductivity that is at least one order of magnitude greater than organic and IL electrolytes [89]. This is advantageous for decreasing the ESR (Equivalent series resistance) and promoting improved power delivery. The equilibrium and non-equilibrium MD simulations of the transport of aqueous K^+Cl^- electrolyte in charged cylindrical nanoporous electrodes were conducted using the extended simple point-charge model [90]. The electrode's surface was designed to be smooth and hydrophobic. Ionic confinement effects were investigated by changing the radius of the electrode. Strong confinement was shown to produce ion desolvation, increased the external field's influence on water molecule orientation, and reduced hydrogen bonding. The ionic conductivity was also shown to decrease when the pore radius reduced. A series of studies have also been carried out to study the impact of ion type. EDL capacitance is influenced by the properties of RTIL ions. A study evaluated two Room Temperature Ionic Liquids (RTIL), [BMIM][BF4] and [BMIM][PF6], and discovered that more asymmetry might lead to a wider difference between the maximum and lowest capacitances [91]. Smaller RTIL ions may result in increased capacitance for the corresponding electrode in general [92]. However, a simulation study

found that increasing the size of anions increases the cathode capacitance significantly [93]. The energy storage is affected by the presence of organic solvents. On the one hand, changing the polarity of solvent molecules could slow down the oscillation of the capacitance versus pore size curve after the initial peak [94]. When compared to pure RTIL electrolyte, a modest amount of solvent can boost capacitance [95]. The presence of Acetonitrile (ACN) molecules, on the other hand, accelerates the movements of RTIL ions, which can be attributed to decreased Coulombic interactions due to the increased distance between the electrolyte ions shown in Fig 1.9 [96]. Water as a solvent can reduce ionic effects, resulting in nearly equal capacitances for ions of various diameters and valences [97]. Wu et al. discovered three separate charging stages for RTIL by analyzing the number density in the pores: ion exchange for low voltage, co-ion exclusion for medium voltage, and counterion adsorption for high voltage[98]. Desolvation of hydrated ions can be aided by the confinement effect. The abnormal rise in capacitance is closely related to the desolvation of solvated ions, which can be considerably aided by confinement. The hydration number and hydration structure are two parameters that can be used to quantify the desolvation phenomenon. When pore widths range from 0.9 to 1.6 nm, Kalluri et al. discovered that narrowing the pore can result in a lower hydration number [99]. MD simulations were performed of aqueous NaCl electrolytes inside charged nanoporous graphene and slit-pore electrodes. The anode and cathode were modelled on opposite sides of the pore walls. To investigate the structural properties of aqueous electrolytes, the electrolyte concentration, surface charge densities, and pore diameter were all altered. The ionic concentration inside the pores reached nearly 10 times the bulk concentration at the maximum surface charge density evaluated (± 40 C/cm^{-2}). Multiple layers of adsorbed electrolytes occurred around the electrode surface, as well. This behavior was comparable to that seen by Wander et al. and it was related to electrostatic interactions, hydration processes, and ion-ion correlations, among other things [100]. Although aqueous electrolytes provide a high-power density for EDLCs, their energy densities are frequently low. Future simulations of EDLCs using aqueous electrolytes must focus on optimization of innovative electrode materials, rather than the slit-type nanopores employed in prior models, to compete with the high energy densities afforded by RTIL electrolytes.

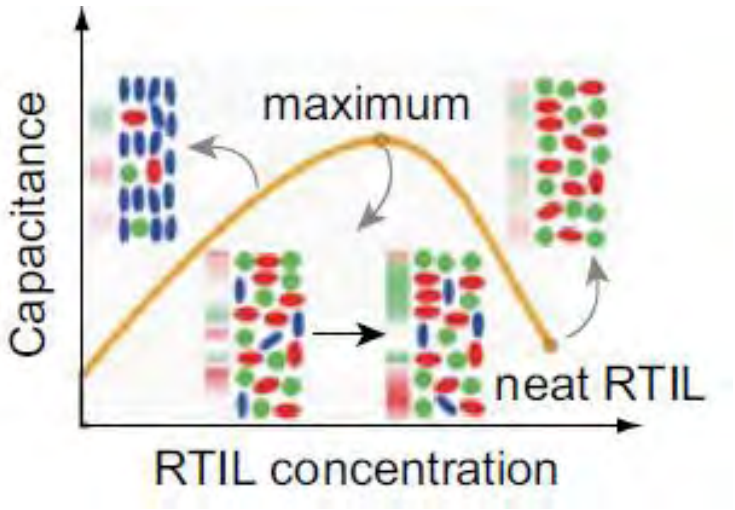

Fig 1. 10: Variation of capacitance with respect to varied concentration of ACN [96].

1.10 Objective of This Study:

It is clear from the preceding sections that the use of EDLCs as efficient energy storage devices is a rapidly developing topic. Molecular modeling can help with the optimization of EDLCs as a whole system, as well as the identification of new electrode materials and electrolyte combinations with improved electro-capacitive performance. In response to experiments that questioned long-held notions of the EDL, molecular modeling has made significant contributions to our knowledge of charge storage processes and dynamics in EDLCs in recent years. Under equilibrium settings, molecular modeling has mostly focused on planar electrodes to examine steric and potential effects, and porous electrodes to study confinement effects. From the previous studies, there is a clear indication that electrode material with higher SSA, 3-D structure, pores can be beneficial than other materials. In line with these observations, crumple graphene would be an ideal electrode material. The existing literature has considerable gap in this particular area. So, the prime objectives of this study are:

i. To investigate the capacitive behavior of EDLC with crumpled graphene electrode by employing molecular dynamics simulation.

ii. To analyze the effects of the degree of crumpling state on the EDLC characteristics.

iii. To study the effect of nano-level pores on the crumpled graphene electrode surface.

iv. To evaluate the influence of the wettability of the crumpled graphene electrode surface on the energy storage performance of the supercapacitor.

Chapter 2

Computational Methodology

Computational analysis is utilized to duplicate the properties of a system. In a number of instances, it is challenging to collect information directly from trials. In these instances, computer models can deliver reliable data with fewer obstacles. The "force field" contributes significantly to the accuracy of these simulations. In actuality, the force field parameters replicate the underlying physics and explain how the energy of the molecule reacts to specific function-required events. In many instances, they necessitate a substantial amount of simplification in order to reduce the inherent complexities of real-world problems and make the analysis more manageable. In this chapter, the details of the computational methodology adopted in this study are discussed.

2.1 Molecular Dynamics Simulation

Large-scale Atomic/Molecular Massively Parallel Simulator was utilized for the simulation of Molecular Dynamics in the computational analysis of the current work (LAMMPS). The impact of a solvent (water) and aqueous electrolyte (NaCl) on the structural and capacitive properties of an electrochemical supercapacitor based on a crumpled graphene electrode was investigated using molecular dynamics simulations. Further improved and modified models were explored to optimize performance.

2.1.1 Large-scale Atomic/Molecular Massively Parallel Simulator (LAMMPS)

The time evolution of a group of interacting atoms is traced by integrating their equation of motion in molecular dynamics, a mechanics-based computer simulation method. Individual atoms are numerically integrated using Newton's second rule of motion, and the interactions between them are specified by empirical potential fields.

$$F_i = m_i a_i \tag{2.1}$$

For a set of N atoms, m_i denotes the mass of the atom, $a_i = \frac{d^2 r}{dt^2}$ denotes its acceleration, and F_i is the force exerted on the atom by the interacting atoms.

Molecular dynamics is a deterministic method in which, given an initial set of coordinates and velocities, the following temporal evolution is, in theory, totally predetermined. Atoms will behave similarly to how they behave in actual matter. For instance, atoms in the simulation domain will interact by moving, colliding, wandering, and oscillating in waves with their neighbors. Even atoms will evaporate if there is a free surface and so on.

LAMMPS is a classical molecular dynamics program that is mostly used for modelling materials. Sandia National Laboratories, a US Department of Energy facility, distributes it as open-source code under the GPL terms and conditions. LAMMPS offers potential in various material science domains. LAMMPS can be used to study solid-state materials like as metals and semiconductors, soft materials such as biomolecules and polymers, and coarse-grained or mesoscopic systems. It can be utilized for all atomic, meso, and continuum scales not only to construct atomic models, but also to simulate particles in simultaneously. LAMMPS runs on single processors or in parallel utilizing message-passing mechanisms. During operation, spatial subdivision of the simulation domain is applied. One of the benefits of utilizing LAMMPS is the ability to simply modify or add new functionality to the code created and used [101].

2.1.2 Modelling the Physical System

The primary component of a simulation is a physical system model. This entails selecting the potential for a molecular dynamics simulation: a function V (r_1, ..., r_N) of the locations of the nuclei that represents the potential energy of the system when the atoms are organized in the specified configuration. This function is invariant with respect to translation and rotation. It is often derived from the relative locations of the atoms in the simulation region.

The forces are then obtained from the gradients of the potential in relation to atomic displacements:

$$F_i = -\Delta_{r_i} V(r_1, ..., r_N) \tag{2.2}$$

This expression indicates the existence of a conservation law for total energy E = K + V, where K represents instantaneous kinetic energy. A simple technique of expressing V is as the sum of pair-wise interactions.

$$V(r_1, ..., r_N) = \sum_i \sum_{j>1} \varphi(|r_i - r_j|) \tag{2.3}$$

The goal of the sentence j > i in the second sum is to consider each atom pair just once. In the past, pairwise interactions were the only parameter that comprised the majority of potentials, but this has changed. In addition, the performance of the two-body approximation for many significant systems, such as metals and semiconductors, is extremely low. In modern simulations of condensed matter, a variety of many-body potentials are utilized.

2.1.3 The Lennard-Jones Potential

The Lennard-Jones (LJ) 12-6 potential [110] is given by the expression:

$$\varphi(r) = 4\varepsilon[(\frac{\sigma}{r})^{12} - (\frac{\sigma}{r})^{6}] \tag{2.4}$$

This potential exhibits an attractive tail at high r, a minimum around 1.122σ, and is extremely repulsive at shorter distances, passing through 0 at r =σ and increasing rapidly as r is dropped further.

When atoms are placed very close together, the quantity $\sim 1/r^{12}$ dominates and models the repulsion phenomenon at short distances. The Pauli principle can provide a physical explanation for this: the position of an atom can alter the energy of a system. When atoms approach one another and the electronic clouds begin to overlap, the system's energy grows dramatically. The distance exponent, r, was chosen based on practical considerations. The Lenard-Jones equation is very simple to solve, and an exponential behaviour would be more suitable from a physical standpoint.

The cohesion phenomena of the system are expressed by the dominant $1/r^6$ term at great distances. Due to actuating dipoles, dipole-dipole interactions occur, which generate van der Waals dispersion forces; in the LJ potential, van der Waals forces are responsible for $1/r^6$ attraction. As the interactions are minimal, it often predominates for closed-shell systems, such as the rare gases Ar and Kr. In this potential, parameters such as ε (depth of potential wall) and σ (finite distance at which the inter-particle potential is zero) are incorporated to match the material's physical qualities.

On the other hand, the two-body interactions technique fails to operate simulation models with open shells and LJ potentials. Strong localized bonds (in covalent systems) and delocalized "electron sea" (in metals) cannot be explained by LJ potential physics.

Nevertheless, the LJ 12-6 potential is a crucial model system for studying various geometries such as solids, liquids, surfaces, clusters, and two-dimensional systems, etc. LJ is the standard potential to employ for investigating basic concerns as opposed to analysing individual material features. The study conducted on LJ systems aids in the comprehension of fundamentals in numerous domains, including condensed matter physics. Thus, the significance of LJ characteristics has already been established. In actual applications, a cut-off radius R_c must be set, and atom interactions in the simulation process are separated by this cut-off radius. The advantage of this cut-off radius is that it conserves computational resources, as the number of atomic pairs separated by a distance r grows as r^2 and can be substantial in a short amount of time. A simple truncation of the potential, however, introduces a new issue: every time a particle pair "crosses" the cut-off distance, the energy takes a small leap. Multiple occurrences of this can compromise the energy conservation of a simulation.

To avoid this issue, the potential value for a distance less than the cut-off radius:

$$V(r) = \begin{cases} \varphi_{LJ}(r) - \varphi_{LJ}(R_c) & if\ r \le R_c \\ 0 & if\ r > R_c \end{cases} \tag{2.5}$$

Obviously, the potential truncation has a negative impact on physical quantities. This truncation effect of a full-ranged potential can be predicted approximatively if the simulation domain is assumed to be a uniform continuum beyond R_c. For instance, the potential tail contributes additionally to the cohesive (attractive) energy as well as the total pressure. The effects of

truncation depend on a number of variables and are difficult to estimate. For instance, it is challenging to evaluate the truncation effects for geometries with free surfaces and low system symmetry. In our simulation, to describe the interaction of electrode-electrolyte L-J potential was used to mimic the real physical scenario by incorporating the dipole and van der interactions.

2.1.4 Periodic Boundary Conditions (PBC)

In molecular dynamics simulation, periodic boundary condition (PBC) is utilized to reduce the surface effects. In PBC, an endless lattice can be generated using a simulation box that replicates itself throughout space. In each box of this endless lattice, the movement of molecules is identical. Due to periodic image consideration, if a molecule moves in the central box, all other box's molecules will move with the exact same orientation. In addition, as the molecule leaves the center box, one of its images will enter the box from the opposite face. In a PBC system, there is no surface and no barriers at the boundary. A three-dimensional representation of a typical periodic system is depicted in Fig 2.1. From the figure, using the aforementioned idea as a guide, a particle crosses a border, matching images of that particle also cross their respective boundaries. The unchanging number of particles in the middle box implies that the total number of particles in the system is conserved. In our investigation, we opted for the p p f (Periodic, Periodic, Non-periodic, and fixed) boundary condition. This was done because as the two electrodes were kept 50Å apart in z-direction, electrolyte movement in z-direction was the only point of concern in this study. So, PPF boundary condition were employed.

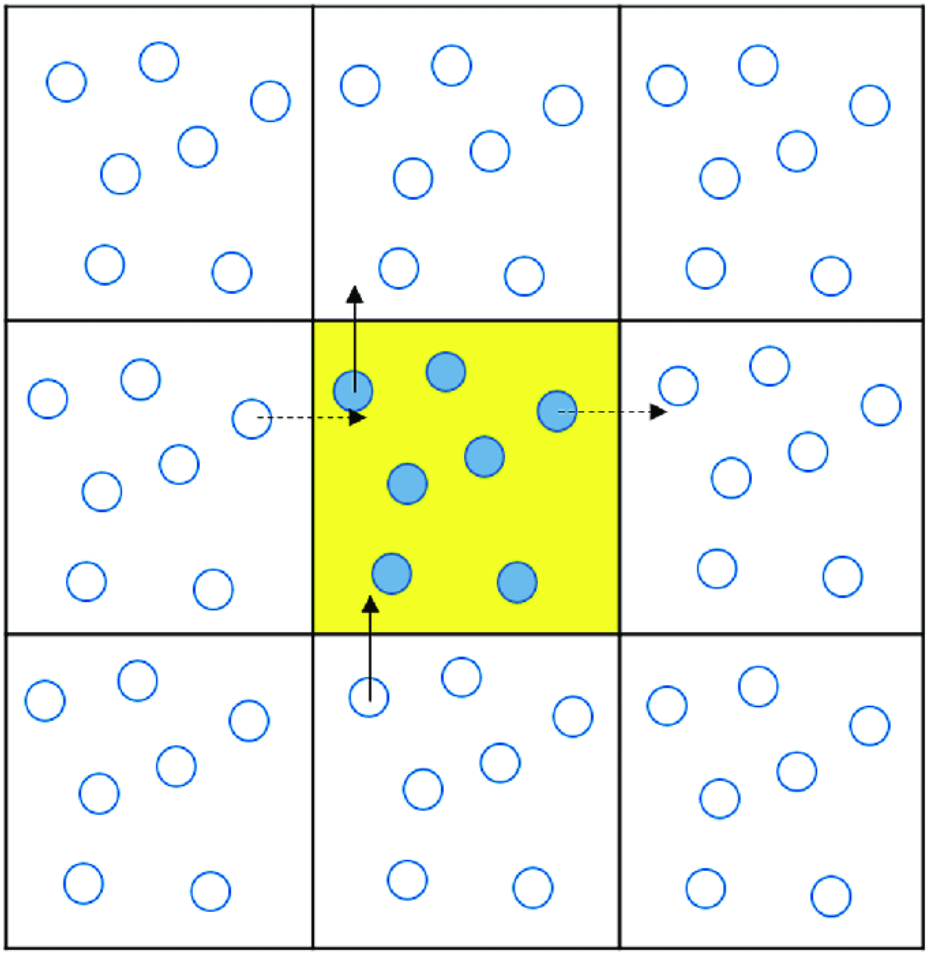

Fig 2. 1: Periodic boundary conditions (The central box is outlined by a thicker line)

2.1.5 Time Integration Algorithm

The time integration algorithm drives the simulation of molecular dynamics. It functions by integrating the motion equation of the interacting particles and tracking their motion trajectory. This algorithm is founded on finite difference techniques. Initially, time is discretized using the finite grid network, w here the time step t is defined as the distance between consecutive grid points. By applying the known data at time t, the integration technique offers the position and some of their time derivatives at the final time t+Δt. By repeating the technique in accordance with the progression of time, this process can run for extended periods. There are a number of well-known integration methods for MD calculations, such as the Verlet algorithm and predictor-corrector

techniques, among others. Verlet style, which is a typical velocity-Verlet integrator compatible with PPPM style, has been employed in this study. The reason of the choice of Verlet algorithm is given in the section below.

2.1.5.1 The Verlet Algorithm

Verlet method is the most prominent time integration algorithm in molecular dynamics [102]. Here, Taylor expansions of the third order for positions r(t) form the basis of the algorithm. In total, there will be two equations, one forward and one backward in time. Calling v the velocities, a the accelerations, and b the third derivatives of r with respect to t, one has:

$$r(t+\Delta t) = r(t) + v(t)\Delta t + (\frac{1}{2})a(t)\Delta t^2 + (\frac{1}{6})b(t)\Delta t^3 + O(\Delta t^4) \tag{2.6}$$

$$r(t-\Delta t) = r(t) - v(t)\Delta t + (\frac{1}{2})a(t)\Delta t^2 - (\frac{1}{6})b(t)\Delta t^3 + O(\Delta t^4) \tag{2.7}$$

Adding these two equations we get,

$$r(t+\Delta t) = 2r(t) - r(t-\Delta t) + a(t)\Delta t^2 + O(\Delta t^4) \tag{2.8}$$

This is the basic form of the Verlet algorithm. Since we are integrating Newton's equations, a(t) is just the force divided by the mass, and the force is in turn a function of the positions r(t):

$$a(t) = -\left(\frac{1}{m}\right)\nabla V(r(t)) \tag{2.9}$$

As can be seen immediately, the algorithm's truncation error while evolving the system by t is on the order of t^4. This technique is widely utilized by molecular dynamics simulations because to its ease of use, precision, and ability to provide stable circumstances.

The Verlet algorithm's inability to create velocities immediately negates the aforementioned advantages. Even though velocities are not necessary for the time development, they are necessary for calculating the kinetic energy K. To verify the conservation of total energy E = K+V, the kinetic energy must be determined. This is one of the most crucial checks to ensure that an MD simulation is running properly. It is possible to compute the velocities from the positions using;

$$v(t) = \frac{r(t+\Delta t) - r(t-\Delta t)}{2\Delta t} \tag{2.10}$$

Nevertheless, the inaccuracy associated with this equation is of order Δt^2, not Δt^4. Several variants of the Verlet method have already been developed to address this velocity-related issue. These variants result in the exact same trajectory, but differ in terms of which variables are stored in memory and at what periods. One example is the leap-frog algorithm, which handles velocities better than the standard Verlet algorithm [103].

The velocity Verlet scheme is an upgraded implementation of the fundamental Verlet algorithm. This approach includes locations, velocities, and accelerations at time t+ Δt derived from the same numbers at time t as follows:

$$r(t+\Delta t) = r(t) + v(t)\Delta t + (\frac{1}{2})a(t)\Delta t^2 \tag{2.11}$$

$$v(t+\frac{\Delta t}{2}) = v(t) + (\frac{1}{2})a(t)\Delta t \tag{2.12}$$

$$a(t+\frac{\Delta t}{2}) = -(\frac{1}{m})\nabla V(r(t+\Delta t)) \tag{2.13}$$

$$v(t+\Delta t) = v(t+\frac{\Delta t}{2}) + (\frac{1}{2})a(t+\Delta t)\Delta t \tag{2.14}$$

2.1.6 Ensembles

An ensemble is a collection of all of a system's conceivable states. There are multiple ways to regulate temperature and pressure. Different statistical ensembles can be produced based on the fixed state variables (energy E, enthalpy H (that is, U+PV), number of particles N, pressure P, stress S, temperature T, and volume V):

Constant particle number, temperature, and pressure (NPT)

Constant Particle Density, Temperature, and Volume (NVT)

Constant number of particles, volume, and energy (NVE)

Constant particle number, constant pressure, and constant enthalpy (NPH)

2.1.6.1 NPT Ensemble

Using a constant number of particles, constant temperature, and constant pressure, this ensemble offers control over both temperature and pressure (NPT). This procedure permits the unit cell vectors to change, and the volume is modified by adjusting the pressure. To manage pressure, the Berendsen, Andersen, or Parrinello-Rahman approach may be utilized. The Nose-Hoover, Andersen, and Berendsen methods can be used to regulate temperature. When accurate pressure, volume, and density are simulation priorities, the NPT ensemble may be chosen.

2.1.6.2 NVT Ensemble

The NVT ensemble is attained by maintaining a constant number of particles, volume, and temperature. During the initialization phase of this procedure, direct temperature scaling was used to control the temperature. During the data collection phase, temperature-bath coupling was also implemented. Temperature-controlled MD simulation is crucial for a variety of system types.

2.1.6.3 NVE Ensemble

During the simulation, pressure and temperature are not controlled. The primary purpose is energy conservation. Nevertheless, this could result in a pressure or temperature overrun throughout the time integration process. Typically, a more stable system is appropriate for NVE. Thermodynamic systems that adhere to the NVE ensemble are shielded from their surroundings.

2.1.6.4 NPH Ensemble

Constant number of particles, constant pressure, and constant enthalpy H, which is the sum of U and PV, produce this ensemble. In this technique, the pressure is maintained without regard to temperature. Although NPH dynamics do not regulate temperature, these settings can be used

during the simulation's equilibration phase. By periodically scaling the velocities, it is possible to maintain the temperature within defined tolerances for this purpose.

In our research, temperature controlling is a vital parameter as the simulation was conducted into different temperature in different time steps. For this phenomenon NVT ensemble was incorporated in our simulation.

2.1.7 Particle-Particle Particle-Meshstyle (PPPM)

The pppm style invokes a particle-particle particle-mesh solver , and this method transfers atom charge to a three-dimensional mesh [104]. This is accomplished by solving Poisson's equation with 3D FFTs on the mesh, which then interpolates electric fields on mesh points back to the atoms. This technique is similar to the AMBER and CHARMM-utilized particle-mesh Ewald method (PME) [105]. Traditional Ewald summing has a scaling factor of $N^{(3/2),}$ where N is the number of atoms in the system. In contrast, PPPM solvers utilize Nlog(N) scaling due to FFTs, indicating that PPPM is always the quicker option [106]. The criterion for implementing PPPM is that the object must be three-dimensional and periodic in all dimensions. That is why we implemented the pppm style. The only exception where the above-mentioned boundary condition can be amended is slab option which has to be set with kspace modify. In this situation, the xy dimensions must be periodic, whereas the z dimension must be nonperiodic.

In order to compute long-range Coulombic or $1/r^6$ interactions, it is necessary to define a long-range solver for LAMMPS to employ at each time step. This command is called "kspace style command" because most long-range solvers do computations in K-space [107]. With an appropriate pair style, the cut-off for Coulombic or $1/r^N$ interactions is virtually limitless for such a solver. Using this method, the simulation domain for the Coulombic scenario will be limitless. Because an endless number of periodic images of the simulation domain will be formed, with each charge in the system interacting with charges in each periodic image, the simulation domain will be represented by an infinite number of periodic images. Note that a matching pair style is required to do consistent short-range pairwise calculations with a long-range solver. This shows that for each pair style, there is a corresponding keyword for the Kspace style, i.e., for the pppm solver,

the pair style must be coul/long. In our research, the lj/cut/coul/long pair style was implemented with a global LJ parameter cutoff.

2.1.8 General Procedure of Molecular Dynamics Simulation

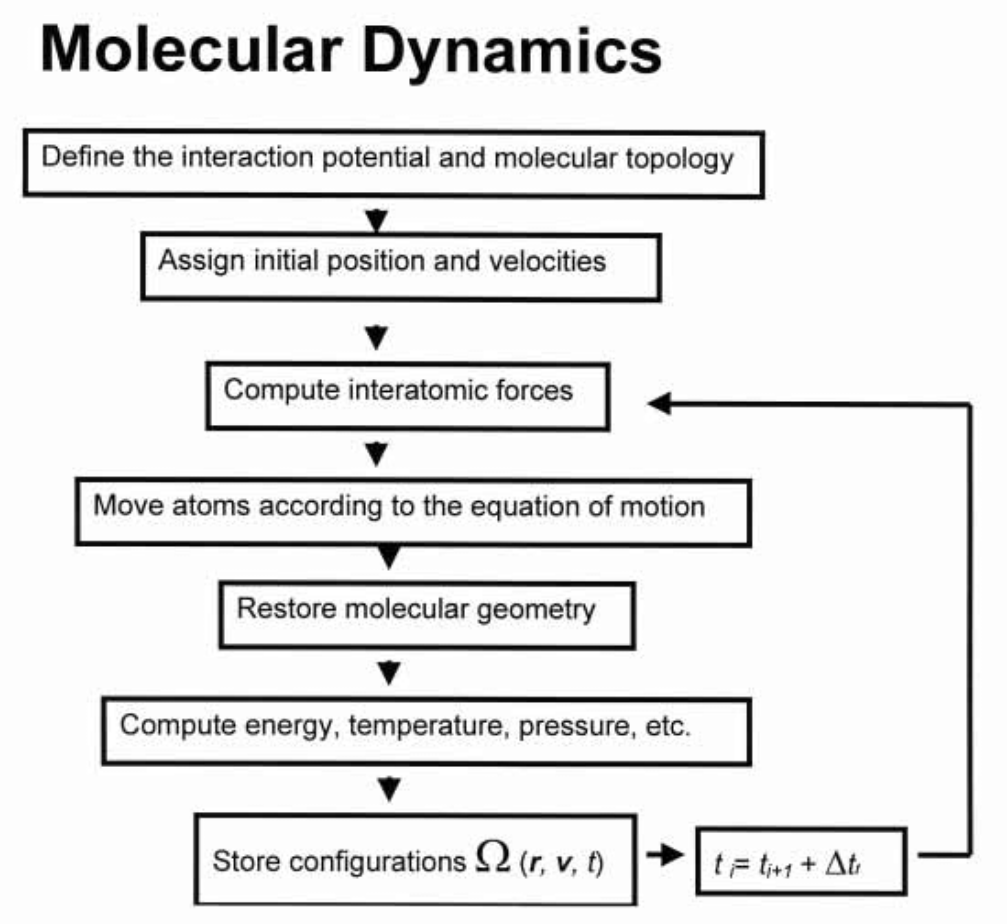

Fig 2. 2: Schematic diagram of a basic MD code [107]

The general procedure of the MD simulation is described in Fig 2.2.

2.1.9 Limitations of MD Simulations

Although it is a highly effective method, molecular dynamics is not without its drawbacks. We spend a brief amount of time focusing on the most significant of them.

2.1.9.1 Use of Classical Forces

As it utilizes Newton's law to move atoms, the validity of the molecular dynamics process might be questioned. On the other hand, it is clearly proven that quantum rules are more applicable at the atomic level than classical laws.

A straightforward test of the classical approximation's validity is based on the de Broglie thermal wavelength [108], which is defined as:

$$\Lambda = \sqrt{\frac{2\pi h^2}{M \kappa_B T}} \tag{2.15}$$

where M refers to the mass of an atom and T refers to the temperature. This approximation is valid under the condition $\Lambda \ll a$, where a refers to the mean distance between the closest neighbours. If one examines, for instance, liquids at the triple point, Λ/a is on the order of 0.1 for light elements such as Li and Ar, declining further for heavier elements. Classical approximation is less successful for extremely light systems, such as H_2 and Ne.

2.1.9.2 Realism of Forces

Instantaneous forces are generated as a result of the interaction of atoms with one another in the field of molecular dynamics. Atoms are moved because they are subjected to these instantaneous forces, which operate upon them. Because of this movement, the relative locations and forces have been altered. These instantaneous forces are a crucial component for defining the dominant parameter of the simulation system's physics. If a simulation resembles the behaviour of the actual system, it is realistic. This can only be determined by comparing the interatomic forces to the

actual values when assembled in the same manner. In simulations of molecular dynamics, forces depend on the location of the particles and are often derived as the gradient of a potential energy function. Therefore, the simulation's realism is highly dependent on the suitable potential. Potential must be selected to replicate the actual behaviour of the material under simulation's operating circumstances.

2.1.9.3 Time and Size Limitation

MD simulations may be run on systems with tens of thousands – or even millions – of atoms, with simulation timeframes ranging from a few picoseconds to hundreds of nanoseconds. While these figures are admirable, there may be times when time and/or space constraints are a factor. When the simulation period is substantially longer than the relaxation time of the values we're interested in, the simulation is safe in terms of length. Varying properties, on the other hand, have different relaxation periods. Phase transitions, in particular, slow and sluggish systems. As a consequence, there's a chance that simulation time will be less than the relaxation period of a physical feature. Another critical element is simulation domain size, since a small system might cause problems. The size of the MD cell must be compared to the correlation lengths of the spatial correlation functions of relevance in this scenario. Again, correlation lengths may lengthen or even diverge in close proximity to phase transitions. Consequently, correlation lengths are no longer comparable to the box dimension.

2.2 Modelling the Simulation Domain for Current Study

Every simulation study begins with a model of the system under investigation. It comprises appropriate atom and molecule definitions, including beginning positions, bonds and angles (if any), masses and charges of each particle, and so on. In our current study, we modelled our simulation domain in three steps:

- Creating crumpled graphene from a flat graphene sheet by simulation
- Modelling the electrolyte-solvent mixture

- Arranging two crumpled graphene as anode and cathode and putting the electrolyte-solvent mixture in the in-between position.

2.2.1 Modelling Crumpled-Graphene Sheets in LAMMPS

The folding of graphene is not the same as folding a sheet of paper (an isotropic material without preference for folding axes). Similar to the spontaneous organization of dislocations into grain boundaries in a stressed crystal, the crumpling phenomenon can be regarded as a network of ridges, where formation is a manner of condensation of energy into a limited subset of the accessible volume [109]. Square sheet of graphene (250 Å x 250 Å) is simulated atomistically using the adaptive interatomic reactive empirical bond-order (AIREBO)-morse potential for carbon-carbon interactions [110]. The AIREBO/morse potential has been shown to provide an accurate account of the chemical and mechanical behavior of hydrocarbons, including graphene. The MD simulations were performed in LAMMPS. The simulation was performed in NVE ensemble as the primary concern for the simulation was to change in bending energy rather than controlling temperature or pressure. The graphene sheets are stochastically crumpled by limiting them to a spherical area with a constraining spring force. The equation of the force is given below:

$$F(r) = -K(r - r(t))^2 \tag{2.16}$$

The force was created using the fix indent command. It places an indenter in the simulation box. Because the indenter repels all atoms in the group that come into contact with it, it can be employed to push into a material or act as a flow obstruction. It can also be used to create a restrictive boundary around a simulation.

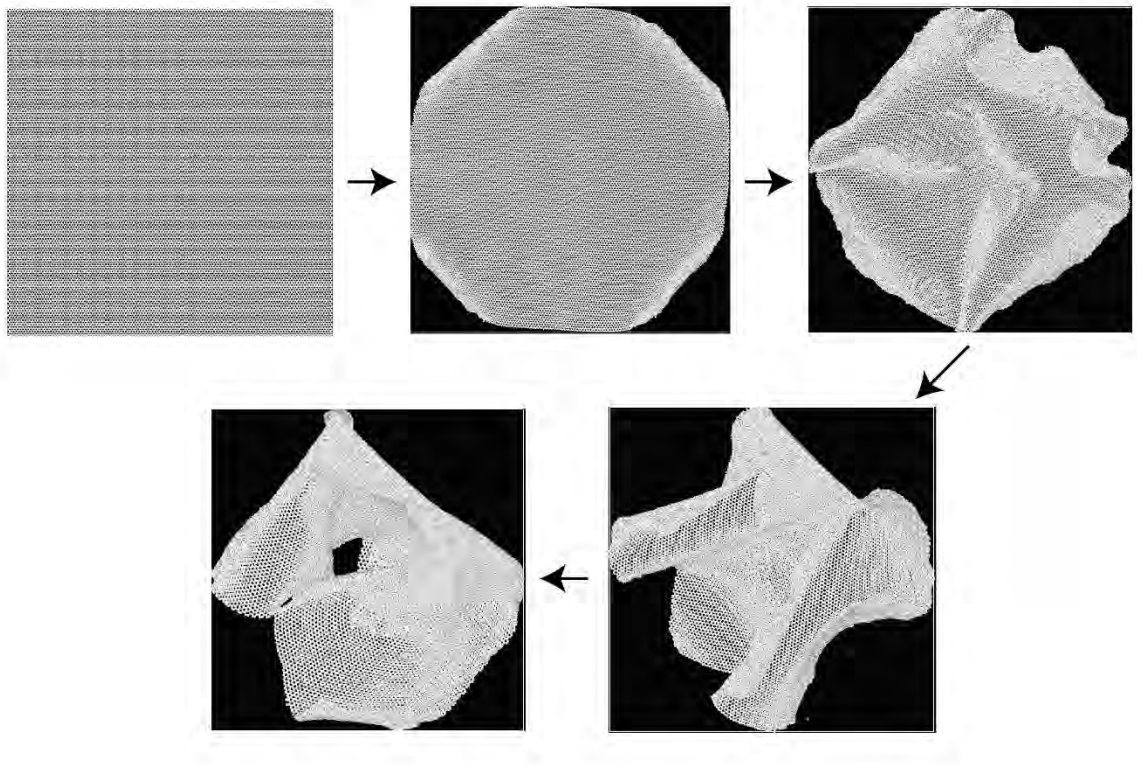

Fig 2. 3: Crumpling of Graphene from a layer of conventional planer graphene.

Crumpling has been performed using LAMMPS in the following steps –

1. Initialization: In all three directions (x, y and z directions), the boundary conditions were specified to be periodic. Carbon atoms with a lattice constant of 3.567 were used to create a graphene layer. To generate an initial temperature, all atoms were given an initial velocity.
2. Thermal Equilibrium: Within the simulation box, the "fix balance" command was used to change the size and shape of processor sub-domains in order to try to evenly distribute the number of particles and thus the computing load among processors. The load balancing is "dynamic" in that it was rebalanced on a frequent basis throughout the simulation. To achieve thermal equilibrium, the simulation was run.
3. Crumpling of Graphene: To begin the crumpling, a spherical indentation force was applied. The effective crumpling radius was gradually reduced at a rate of 0.75Å/step, with a

timestep of 0.002 picoseconds. This was done to avoid any atom loss as a result of the temperature rise. In addition, all three directions' boundary conditions were adjusted to shrink. After each step the radius of the crumpled graphene was calculated using the equation below:

$$r = r_0 - (Current\ step\ number - Number\ of\ steps\ for\ equilibrium) * rate * timestep \quad (2.17)$$

4. Final Simulation: The final simulation was run with a set number of steps to achieve the desired crumpling level.

The crumpling process is shown in Fig 2.3.

2.2.2 Electrolyte Modelling

Water and aqueous NaCl make up the electrolyte. By altering the masses and link lengths, we were able to model each instance. A MATLAB code is used to create the model. The procedures for creating the algorithm are outlined below in Fig 2.4.

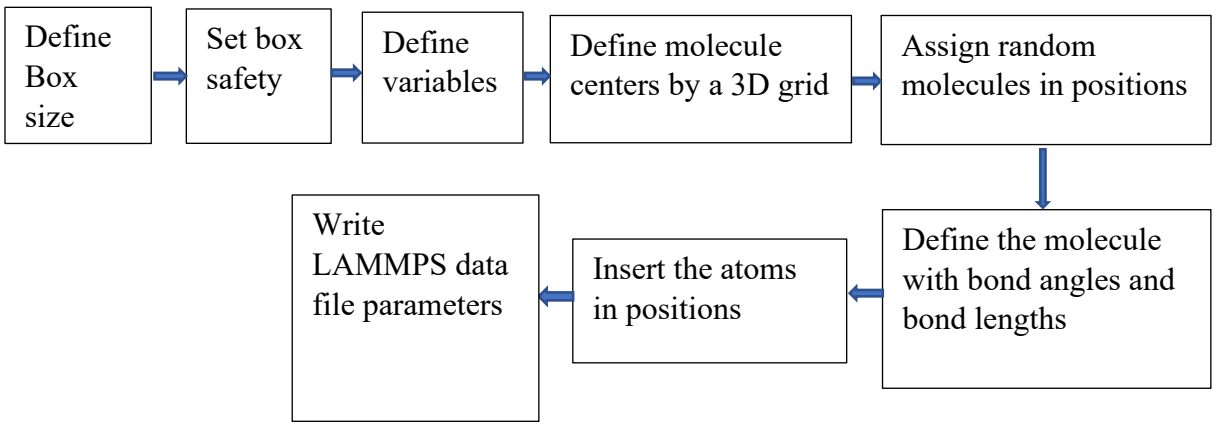

Fig 2. 4: Algorithm for Modelling electrolyte solution

We started by determining the dimensions of the box in which the electrolyte would be generated. This size is determined by the electrode size, and safety measures are taken to ensure that atoms do not escape the confines of the box. The number of atoms, atom kinds, number and type of bonds, bond length, angle type and number, and atom charges are then defined. We came up with the terms lw ratio and lh ratio, which stand for length, width, and height ratios. This variable is required for the creation of the three-dimensional grid on which the molecules will be put. The size of the grid is determined by the total number of particles. This formula is utilized in this case.

$$X = \sqrt[3]{\frac{Nl^2}{wh}} \tag{2.18}$$

Where, N = Total number of molecules

w = Width of the box

h = Height of the box

l = length of the box

X = Number molecules in direction of length

This technique comprises taking a ceiling decimal number and translating it into a three-dimensional grid, which means that certain positions in this design may be unoccupied.

Then comes the LAMMPS data file section, where various parameters must be defined in order for LAMMPS to read them.

The sites of the molecules have already been discovered; now we must characterize them. They are characterized as a center with each atom near it equidistant to half the bond length for sodium halides.

The oxygen is preserved in the center of water, while one hydrogen is at a bond length distance and another at 104.52 degrees from the first hydrogen at the same bond length distance.

We rotated the atoms at random using the rot function in MATLAB, and then populated each atom position with its associated type.

A final output file is produced, and the word "Done" is printed.

2.2.3 Simulation Physics Employed in the Present Study

- The Particle-particle particle-mesh (PPPM) algorithm of LAMMPS was used to calculate columbic interaction in the simulation domain.
- The TIP3P (transferable intermolecular potential 3P) model and shake algorithm are used to determine water interaction. This approach is better than any other model at reproducing the observed dielectric constant of water.
- The van der Waals interactions between ions, carbon atoms, and water molecules are established using Lenard-Jones (LJ) potential parameters.
- The number density $\rho(x)$ of particles, which is often used to depict the electric double layer structure, is determined using Molecular Dynamics modelling. Higher number density $\rho(x)$ in electrolytes indicates concentrated electrolytes, which are essential to lower equivalent series resistance and increase power output.
- In case of electrodes, the constant surface charge and constant electric potential methods can be applied. For low electric potential ($\leq$2V), both approaches show minor differences in EDL structure. In addition, for experimental settings, the constant electric potential technique is preferable. The constant surface charge approach is used on the electrodes in this investigation.

2.2.4 Units: Real, Metal and SI Units

A set of units is available to use in LAMMPS, and it must be stated at the beginning of the input file. It determines the units of all quantities indicated in the input script and data file, as well as amounts reported to the screen, log file, and dump file. For this, the "units" command is used at the start of an input script. The most common units used in LAMMPS are real, metal, SI, and so on.

We employed a "real" style to define the units in our research, which included [111]:

- mass = grams/mole
- distance = Angstroms
- time = femtoseconds

- energy = Kcal/mole
- velocity = Angstroms/femtosecond
- force = Kcal/mole-Angstrom
- temperature = Kelvin
- pressure = atmospheres
- charge = multiple of electron charge (1.0 is a proton)

2.2.5 Simulation Time Step

Berendsen thermostat was used to manage the temperature of the simulation environment. Temperature was progressively increased from 298K to 373K during a 10ps time, then maintained at 373K for another 10ps before being gently cooled to 298K over a 10ps period. At 298K, NVT ensemble MD simulations are run for additional 1.2ns. The code is given below:

```
fix     1 All_liquid nvt temp 298.0 373.0 100.0
run     10000
unfix   1
fix     2 All_liquid nvt temp 373.0 373.0 100.0
run     10000
unfix   2
fix     3 All_liquid nvt temp 373.0 298.0 100.0
run     10000
unfix   3
fix     4 All_liquid nvt temp 298.0 298.0 100.0
run     1200000
unfix   4
```

Here, the actual code is: fix fix-ID group-ID nvt temp T_{start} T_{stop} T_{damp}

Where T_{start} and T_{stop} are the temperatures at the start and the end of the run. T_{damp} is the temperature dumping parameter.

These commands use non-Hamiltonian equations of motion in the Nose-Hoover style for time integration. For canonical (nvt), isothermal-isobaric (npt), and isenthalpic (nph) ensembles, locations and velocities are obtained by this integration method.

2.2.6 Simulation Domain

The spacing between the simulation cell's innermost electrode layers is 5 nm. Water and a sodium chloride combination with a total number of atoms of 16000 make up the electrolyte. For a 1M solution, there are 500 Na^+ and 500 Cl^- ions and 5000 water molecules. There are 34263 atoms in each anode and cathode.

The cell's overall dimensions are shown in Table 2.1. The simulation domain details are shown in Table 2.2 and Fig 2.6.

Table 2. 1: Total number of bonds, angles, atom types, bond types, angle types and size of simulation cell

TOTAL ATOMS	**84526**
Total bonds	10000
Total angles	5000
Atom types	6
Bond types	1
Angle types	1
Size of simulation cell (nm)	13.5 x 14.2 x 36.3

Table 2. 2: Dimension of Simulation domain

	Start point	End point
Anode	Z=0	Z=15.79nm
Electrode	Z=15.79nm	Z=20.79nm
Cathode	Z=20.79nm	Z=36.58nm

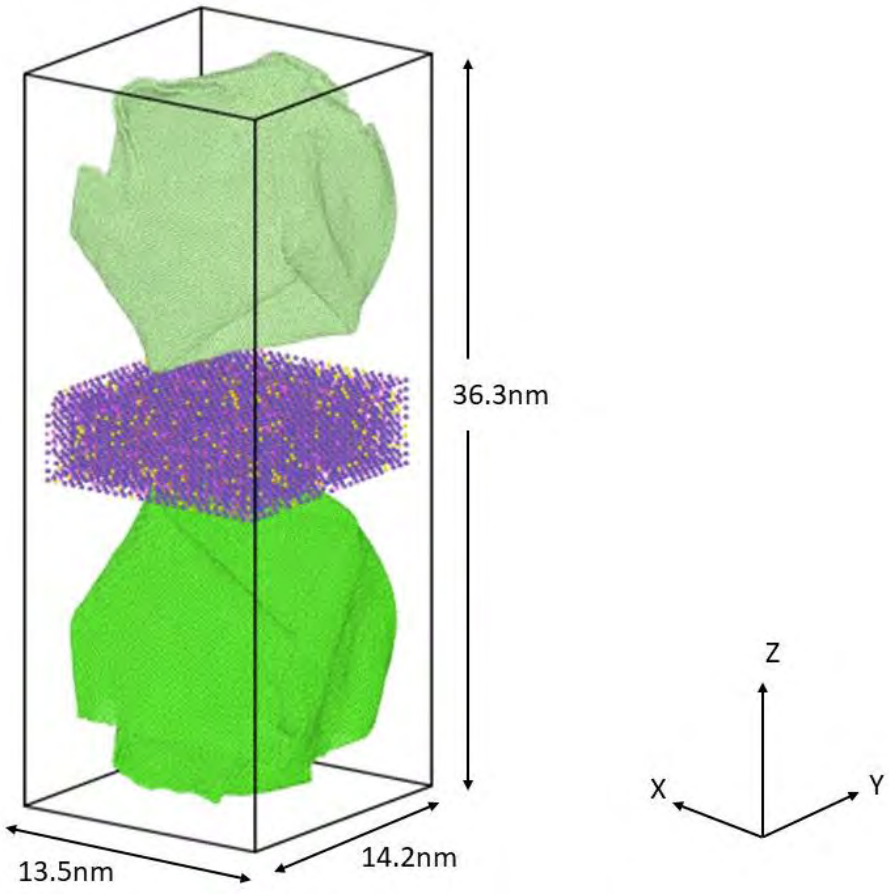

Fig 2. 5: Full Set-up of the Simulation Model

2.2.7 Pair_Style, Bond_Style and Angle_Style Commands

We utilized pair style "full" for our research because we were working with charges and ions. To be in line with prior simulation research [107], both Bond and Angle styles were designated as "harmonic."

2.3 Simulation Parameters

2.3.1 Atom Types, Total number and Atomic Mass

We have selected six types of atoms from the periodic table for our study. These are outlined below Table 2.3.

Table 2. 3: Atom types and their masses used in current study

ATOMS TYPE	ATOM IDENTIFICATION	MASS(AMU)
1	O	15.9994
2	H	1.0078
3	Na	22.9898
4	Cl	35.5
5	C (anode)	12.01
6	C (cathode)	12.01

2.3.2 Force Field Parameters – Bond Coefficients

LAMMPS is utilized to calculate bond interactions between atom pairs. Bond coefficients define the existence of bonds between specified pairs of atoms over the duration of the simulation. In our research, we employed the harmonic bond style, where r_0 is the equilibrium bond distance and k

are the bond energy/distance^2. Along with the bond coefficients, the masses of all atoms must be given for a LAMMPS input file. The tables 2.4 contain a summary of all parameters.

Table 2. 4: Bond Co-efficients.

Bond Coefficients		
Atoms	**K (kcal/Å^{-1})**	**r_0 (Å)**
Na - Cl	799.280	1.40
Water O - H	554.135	1.0

2.3.3 LJ Parameters: Pair Coefficients

Using the modified Lenard-Jones (LJ) potential, the van der Waals interactions between electrolyte ions, carbon atoms, and water molecules have been calculated. Transferable intermolecular potential 3P (TIP/3P) model has been utilized for water because, among the most prominent water models, it reproduces the experimental dielectric constant of water the best. Using the SHAKE algorithm, bond lengths and angles in water molecules have been maintained. Utilizing the Lorentz-Berthelot mixing rule, the LJ potential parameters between electrolyte ions, water, and carbon atoms have been determined. The pair coefficients of all atoms utilized in this investigation are shown in Table 2.5.

Combining rules for the Lennard-Jones potential: Lorentz-Berthelot rule:

H. A. Lorentz proposed the Lorentz rule in 1881: $\sigma_{ij} = \frac{\sigma_{ii}+\sigma_{jj}}{2}$

The Lorentz rule is valid only for hard sphere systems from an analytical standpoint.

Daniel Berthelot established the Berthelot rule in 1898: $\epsilon_{ij} = \sqrt{\epsilon_{ii}\epsilon_{jj}}$

Table 2.5 presents the pair coefficients of all atoms used in this study [91].

Table 2. 5: Pair Co-efficient of the atoms used in current model

Atoms	**ϵ (depth of potential wall), Kcal/mole**	**σ (finite distance at which the inter-particle potential is zero), Å**	**Valence (e)**
O(TIP3P)	0.15540000	3.16550000	- 0.834
H(TIP3P)	0.00000000	0.00000000	0.417
Na	0.13010000	2.35020000	+1
Cl	0.10000000	4.40000000	-1
C	0.12000000	3.29630000	±0.0456

2.4 Modelling Electrodes for Different Degree of Crumpling of Graphene

As it was mentioned in the previous section, that while simulating for graphene sheet into crumple form the radius keep decreasing in every step. Mechanics of crumpling the sheet is to set a spherical spring force which causes the subsequent decrease of the sphere radius. The initial radius of the spherical domain for giving an indenting force was kept at 212 Å. As the radius reduces step by step, the sheet turns more into crumpled form. To evaluate the effect of this varied crumpled state on the EDLC performance 3 models were created in addition to the previously mentioned one. The fully crumpled model's radius is 68.3Å. The force field was kept same as the previously discussed model. The other 3 models were created at 89.5, 110.1 and 165.4 Å. The details of the models are given below in Table 2.6 and schematics are given in Fig 2.6 and 2.7.

Table 2. 6: Simulation domain for varied crumpled state

For r=89.5Å	Start point (nm)	End point (nm)
Anode	Z=0	Z=7.84
Electrode	Z=7.85	Z=12.85
Cathode	Z=12.86	Z=20.70

For r=110.1Å	Start point (nm)	End point (nm)
Anode	Z=0	Z=15.72
Electrode	Z=15.73	Z=20.73
Cathode	Z=20.74	Z=36.54

For r=165.4Å	Start point (nm)	End point (nm)
Anode	Z=0	Z=17.55
Electrode	Z=17.56	Z=22.56
Cathode	Z=22.57	Z=40.11

In these models too, the gap between anode and cathode were taken as 5 nm. The L-J parameters were the same in all cases. Only the electrode configuration is changed, so thus the length of the electrodes was seen different in different degree of crumpling. In each case 1M concentration solution was created with 500 Na^+ and Cl^- ions and 5000 water molecules as solvents.

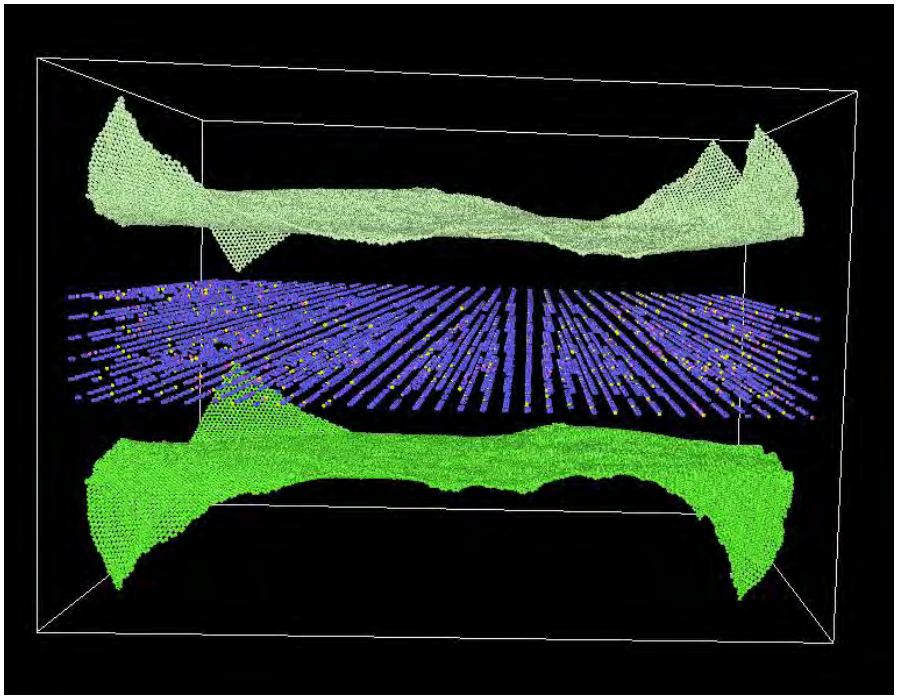

Fig 2. 6: Simulation system for r=165.4 Å.

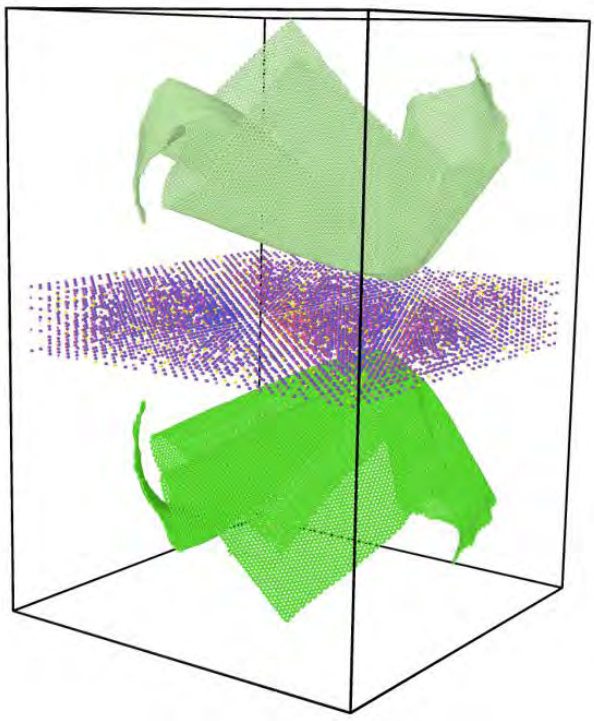

Fig 2. 7: Simulation system for r=110.1 Å

2.5 Modelling of Crumpled Graphene with Defectss

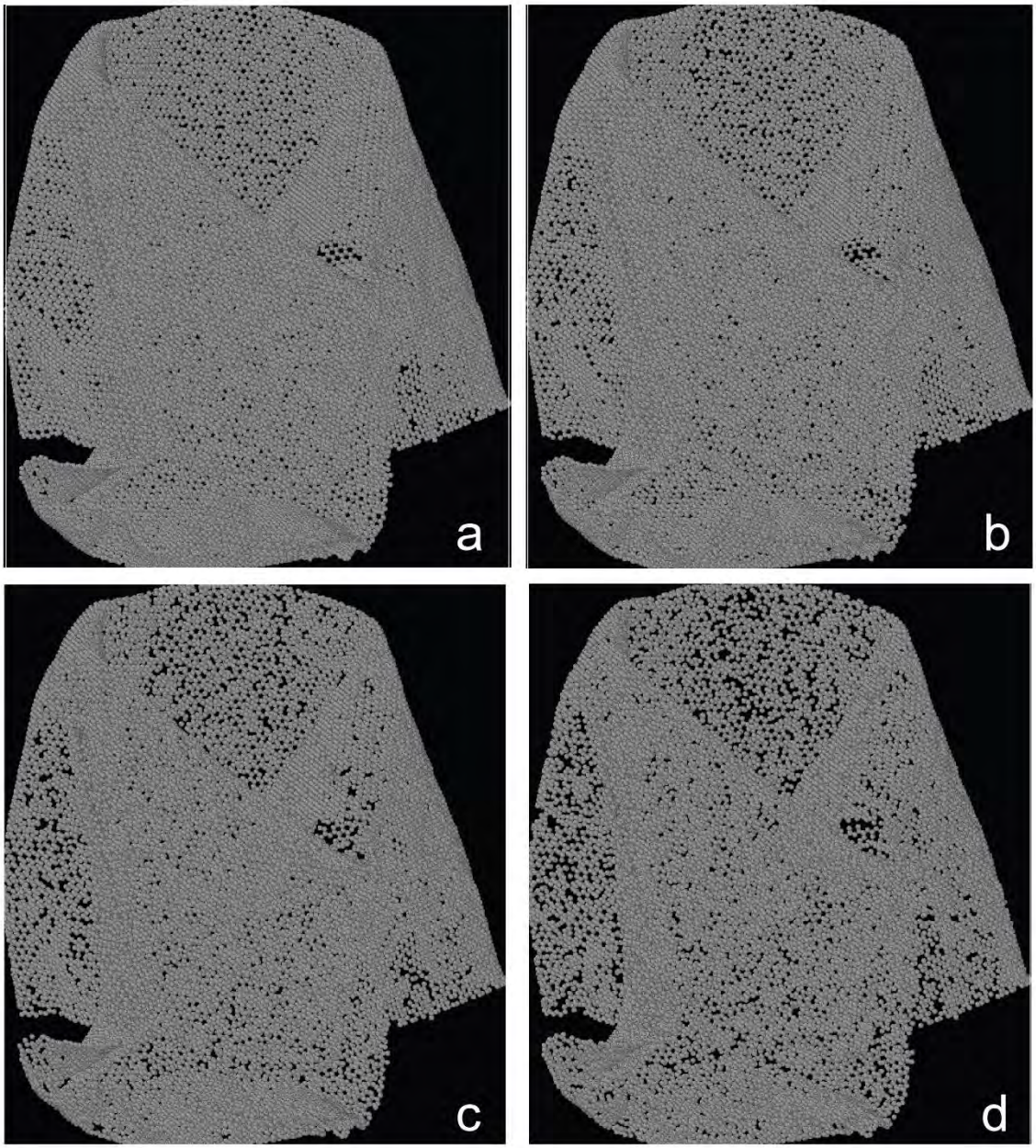

Fig 2. 8: Crumpled graphene for (a) 5% (b) 10% (c) 20% and (d) 30% vacancy

In the chapter 1, a rigorous discussion about the influence of pores on specific capacitance of the EDLC was discussed. Porous electrode always offers an additional benefit towards the performance of the supercapacitor device. So, in this study the varied amount of defects was created on the existing model (r=68.3Å). The amount of the defects were 5%, 10%, 20% and 30% shown in Fig 2.8.

Vacancies in the surface of the graphene were created by using LAMMPS. Atoms were deleted from the graphene sheet that was used for crumpling. This was done by "delete_atoms" command in LAMMPS. In this command the fraction number for deleting atoms were set as 0.05, 0.1, 0.2 and 0.3 for 5%, 10%, 20% and 30% vacancy respectively. Similar L-J parameters were used as the models mentioned in the previous sections. The number of electrolyte and solvent molecules were also unchanged (500 cations and 500 anions, 5000 water molecules). However, In the following Table 2.7 the number of atoms in anode/cathode for different defect levels is specified:

Table 2. 7: Number of atoms per electrode for different defect level

Defects level (%)	**Number of Atoms per electrode**
0	34263
5	32550
10	30837
20	27410
30	23984

2.6 Modelling the Variation of Surface Wettability

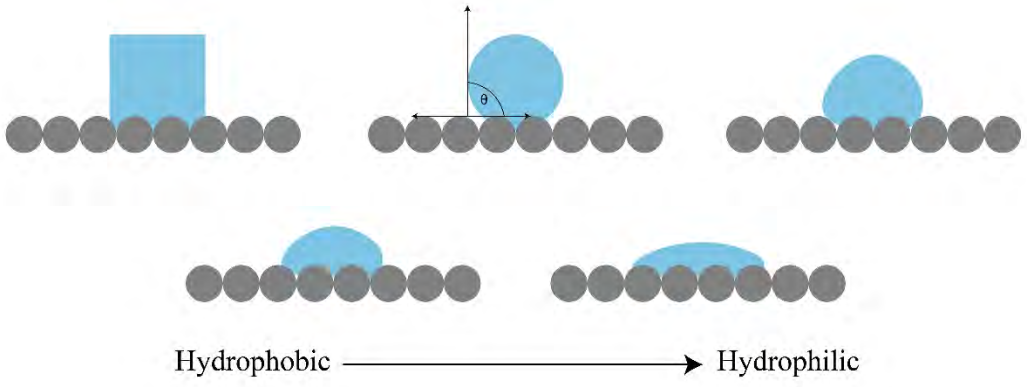

Fig 2. 9: Varied state of surface wettability. Hydrophobic to hydrophilic state from left to right

Wetting property is a fundamental surface feature for defining solid-liquid intermolecular interactions [112]. It is commonly assessed by the equilibrium contact angle θ. The contact angle is the angle formed when a liquid–vapor interface encounters a solid surface and is traditionally measured through the liquid. By increasing the contact angle, the wetting property is deteriorated shown in Fig 2.9. Wettability is thought to have a substantial impact on electrolyte electrosorption, determining effective accessibility, the creation of interfacial EDL structures, and nanomaterial energy storage capacity. The electrolyte electrosorption was enhanced as the electric field strength was increased, overcoming the entrance barriers for ion penetration into nanoscale pores [113]. Furthermore, Kondrat et al. discovered that surface wettability had a significant impact on charging mechanisms, revealing that the electrosorption dynamics of hydrophobic holes differed qualitatively from those of normal, hydrophilic pores [62]. That is the reason EDLC performance was measured by varying wettability in this study. Wetting property, in other word contact angle was varied by adjusting the L-J interaction of the electrode-electrolyte interaction [114]. The binding energy of a water monomer on graphene surface is used as a standard indicator of the strength of the carbon-water interaction to allow comparison between different potential models. A greater carbon-water interaction, i.e., a lower binding energy, encourages spreading of the water on the graphene and results in a smaller contact angle for a fixed bulk water energy. A weakening

of the carbon-water contact, on the other hand, eventually leads to a hydrophobic system. So, by increasing carbon-water interaction the contact angles were changed. Table 2.8 shows the L-J parameters for different degree of wettability we used in this study.

Table 2. 8: L-J parameter for different contact angle [114]

Case	Contact angle	σ_{CO} (Å)	ε_{co} (kj/mol)
1.	29.4°	3.19	0.6270
2.	65.4°	3.275	0.4785
3.	95.3°	3.19	0.3920
4.	141.3°	3.19	0.1881

As it seen from the above table, four different contact angles were used to model four different EDLC. In all cases, the other parameters for example, number of ions, solvent were remained unchanged. In all cases, electrode radius was taken as 68.3Å.

2.7 Surface Charge Density on Electrodes

The applied voltage is represented as a homogeneous distribution of electrical charges on the carbon atoms, as is customary in molecular dynamics simulations. In our simulation the surface charge is taken at 0.045 e/C. This surface charge has been chosen to be consistent with past research. This amount of charge mimic the voltage difference as 2 V [112].

Two crucial factors have been taken into account in the MD simulation shown here: (1) A microporous carbon electrode with a realistic atomistic structure. (2) the polarization of electrode atoms caused by ionic charges. The second method allows simulations to be run with a continuous electrical charge delivered to (conducting) electrodes of any shape.

The constant charges were allocated based on the average total charge observed during constant potential simulations for varied applied potential differences in order to make a fair comparison. This total charge was distributed evenly among the carbon atoms, and the procedure's self-consistency was verified by calculating the potential difference resulting from the so-called

constant charge simulations. It's important to note that the charge variation with respect to potential drop at the electrode/electrolyte interface obtained with constant charge simulations is quite similar to that obtained with constant potential simulations, resulting in similar differential capacitance values. Modelling the polarization relaxation during transient regimes can be used to measure supercapacitor performance in terms of power (i.e., how fast the charge can be provided). This is accomplished using simulations in which the applied potential difference or charge is abruptly adjusted, and the processes that occur before the new steady-state is attained are characterized. The contrast between constant potential and constant charge simulations becomes much more apparent.

Constant potential simulations yielded far more plausible double layer relaxation times, according to these authors. The charge on the electrode atoms fluctuates in reaction to the ionic liquid in constant applied potential simulations; as a result, the charging of the initially empty pores proceeds gradually while they become wetted, resulting in substantially slower relaxation times [115]. The constant potential method, on the other hand, is more computationally intensive than the widely used constant surface charge method. Furthermore, multiple studies have found that EDL structures have a minor difference in simulation between both approaches, particularly at electric potentials less than 2 V. As a result, we used the traditional constant surface charge approach in our investigation [116].

2.8 Calculation of Electric Potential and Capacitance

The channels in this study were separated into a set of bins (each 5 pixels wide) along the x-axis perpendicular to the graphene surface. In each bin, the averaged number density of particles (such as water and electrolyte ions) has been computed. The number densities ρ(x) of the respective particles have been represented by these averaged number densities. Number density ρ(x) is often utilized to represent EDL structures in simulation models. Integrating the following one-dimensional Poisson equation yields the resultant electric potential U(x).

$$\nabla_z[\varepsilon_0 \nabla_z U(z)] = -\rho(z) \tag{2.19}$$

Here, ε_0 and ρ denotes the permittivity of vacuum and charge density of electrolytes and solvents. By integrating the equation 2.19 [65], $U_{electrode}$ can be measured by equation 2.20. σ represents the surface charge density of the electrode.

$$U_{electrode} = \frac{\sigma z}{\varepsilon_0} - \frac{1}{\varepsilon_0}\int_0^z (z - z')\rho(z')dz' \tag{2.20}$$

According to EDLC theory capacitance can be found by equation 2.21 and 2.22 [65].

$$C_{electrode} = \frac{\sigma}{U_{electrode}} \tag{2.21}$$

$$\frac{1}{C_{electrode}} = \frac{1}{C_{anode}} + \frac{1}{C_{cathode}} \tag{2.22}$$

To evaluate the electrode-electrolyte interaction EDLC thickness was measured in this study by the equation 2.23 [65].

$$d = \frac{\int_{z_0}^{z_1} z^N (z - z_0)\rho_{ion}(z)dz}{\int_{z_0}^{z_1} z^N \rho_{ion}(z)dz} \tag{2.23}$$

N is set 1 for planar electrodes. Here z is the position of the electrode whereas z_0 is taken at 0Å. ρ_{ion} is the charge density of the electrolyte.

To explore the energy barriers free energy was calculated by the following equation 2.24 [117].

$$\Delta F(z) = -K_B T \ln\left(\frac{n(z)}{n(bulk)}\right) \tag{2.24}$$

Here, K_B and T presents the Boltzmann constant and electrolyte temperature. n(z) and n(bulk) are the number density of ions.

Chapter 3

Results and Discussion

Numerical simulations of the energy storage behavior of crumpled graphene electrodes in aqueous electrolyte have been conducted. The molecular dynamics (MD) computational model has been validated by comparing density patterns to published literature. The verified computational model was utilized to analyze the behavior of the electric double layer supercapacitor (EDLC), and an enhanced, optimized model was provided as a result of the research. The effect of the degree of crumpling of the graphene, inclusion of defects in the crumpled graphene, and variation of surface wettability on the performance of the crumpled-graphene-based supercapacitors is also examined. In this chapter, the findings and results have been discussed.

3.1 Validation

We attempted to compare our findings with well-established and published studies in order to corroborate the simulation of the current study. Several molecular dynamics studies have been conducted to investigate water models focusing their structure and dynamics. If our current simulation domain is well-designed, the solvent (water) will produce a density peak in the same location as in earlier experiments and simulations. Identical microcanonical (NVE) or NVT simulations were used to examine all different water models, including the TIP3P, SPC, and SPC/E. As said earlier in the chapter 2, we adopted NVT ensemble.

As shown in from the Fig 3.1 it is seen that density peak of O and H molecules form at distance 4.1 Å from electrode surface. The peak is developed at 162 Å and the anode surface is at 157.9 Å. The density peak is of the value of 0.009 for H atom and 0.004 for O atom.

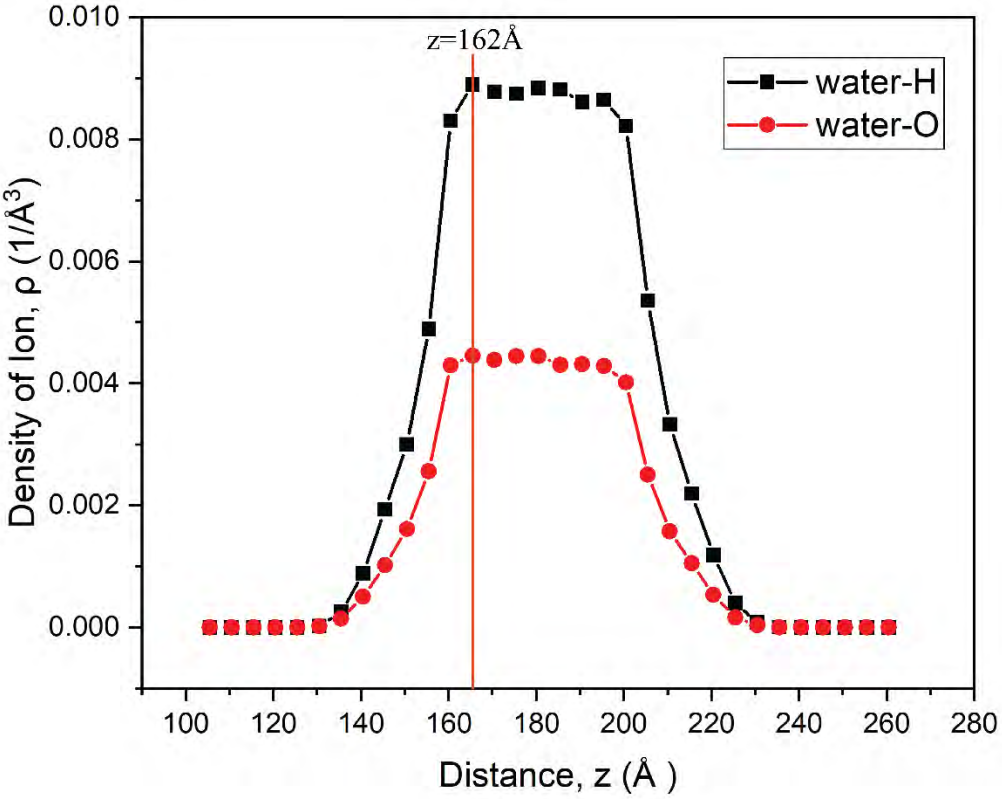

Fig 3. 1: Density profile of water molecules.

The density peak ensures that the water molecules are attracted by the charged electrode surface which lead them to move towards the electrode surfaces. Yang et. al. in his study used the TIP3P model where he found the density peak for water molecules were found at 3.8 Å from the electrode surface [112]. Galib et. al. examined the EDLC performance using the water solvents of TIP3P model and NVT ensemble [107]. It was found the density profile of water molecules showed the highest point at 3.5 Å from the electrode surface. Our simulation results are in well accord with these results.

From the above discussion it can be said that our simulation result shows similar density peaks from the electrode surfaces and thus be validated.

3.2 Performance of the EDLC with Crumpled-Graphene Electrode

In the chapter 1, it was said that when during the discharged stage when the electrodes are neutral in charge, no potential is applied between anode and cathode then the electrolyte ions and the solvent molecules tend stay in the bulk (in the middle region between the electrodes) position in a disoriented order. While the electrodes are charged, they pull the counter-ions near them for example. Positive electrode attracts the negative ions and so on. In the Fig 3.2 the simulation domain of both discharged and charged state are displayed. It is to be noted that the lower electrode is negatively charged and the upper electrode is positively charged. It is seen that Cl^- ions (pink circles) gathers on the surface of the anode. The Na^+ ions (yellow circles) whereas moves to the upper electrode, cathode. Solvent molecules too get attracted by the charged electrodes and therefore pile up near the anode and cathode surfaces. The detail results in this case are elaborated below:

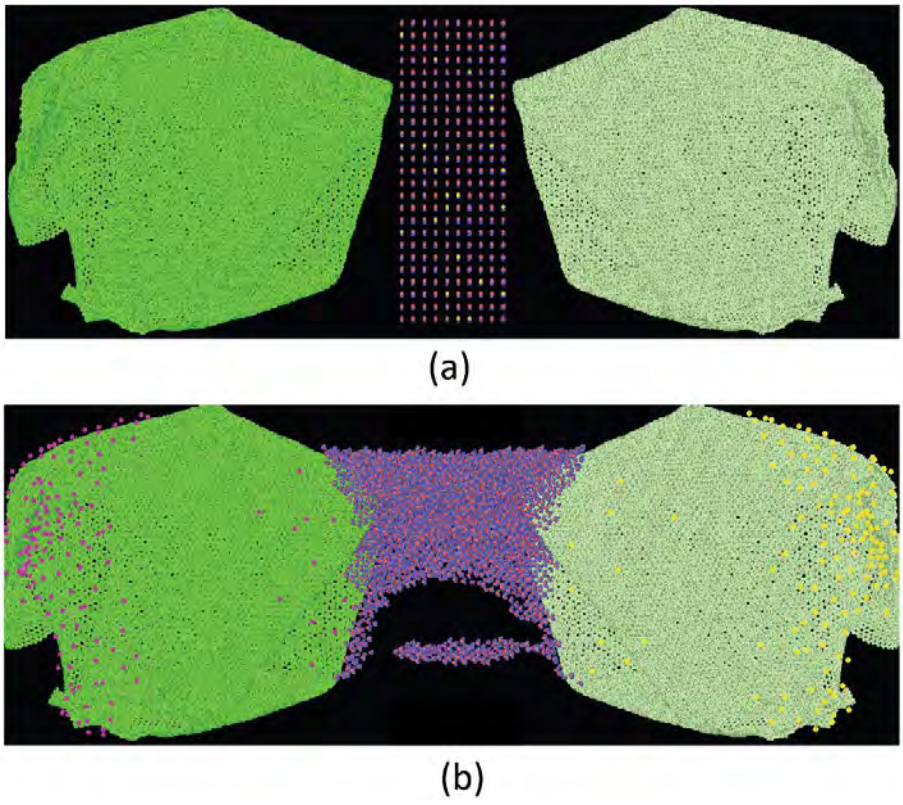

Fig 3. 2: EDLC scenarios (a) discharged state (b) charged state.

3.2.1 Effect on Electrolyte Ions

The number density of electrolyte ions and liquid varies with distance from the electrode surface, this distribution is showed by density profiles. The number density of ions at the electrode is the primary concern in EDLC, that is why density profiles have been investigated in this study. As the graphene electrodes are charged, charged electrodes tend to attract their counter-ions. Fig 3.3 and Fig 3.4 illustrates that Cl^- and Na^+ ions are accumulated near positive (anode) and negative (cathode) electrodes respectively. The accumulation of the counter-ions is result of the electrical interaction between electrode surface and electrolyte ions. In this model the anode starts from 0 Å and ends at 157.9 Å.

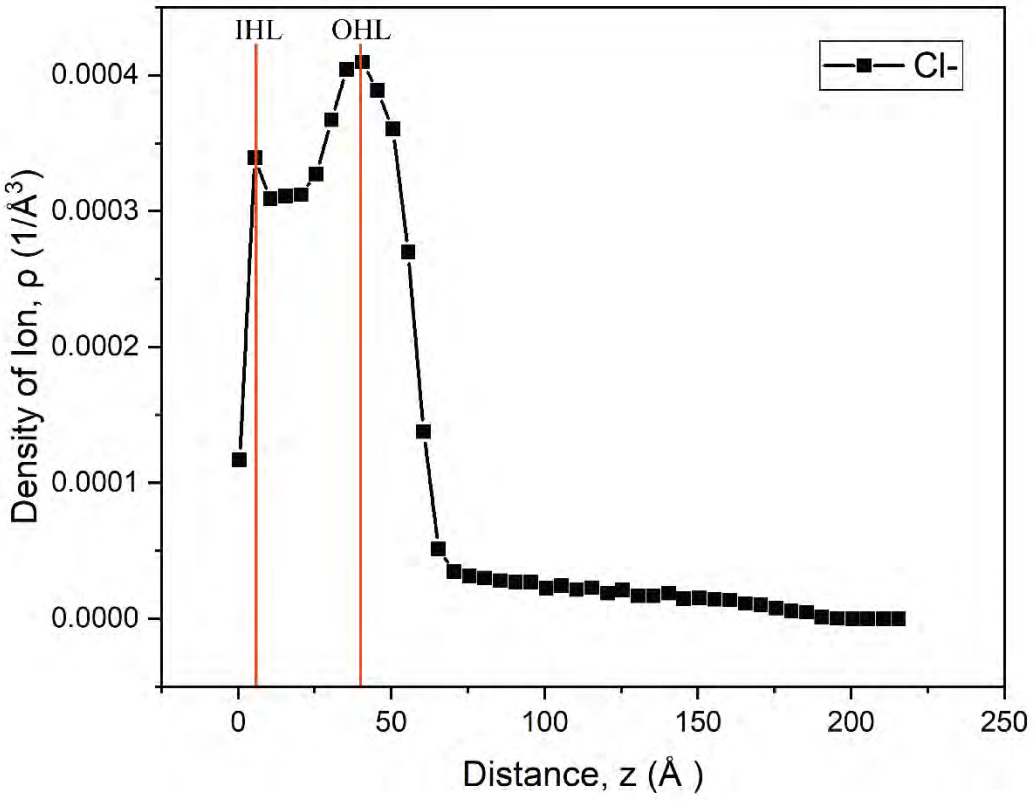

Fig 3. 3: Density profile of Cl^- for validated crumpled graphene model.

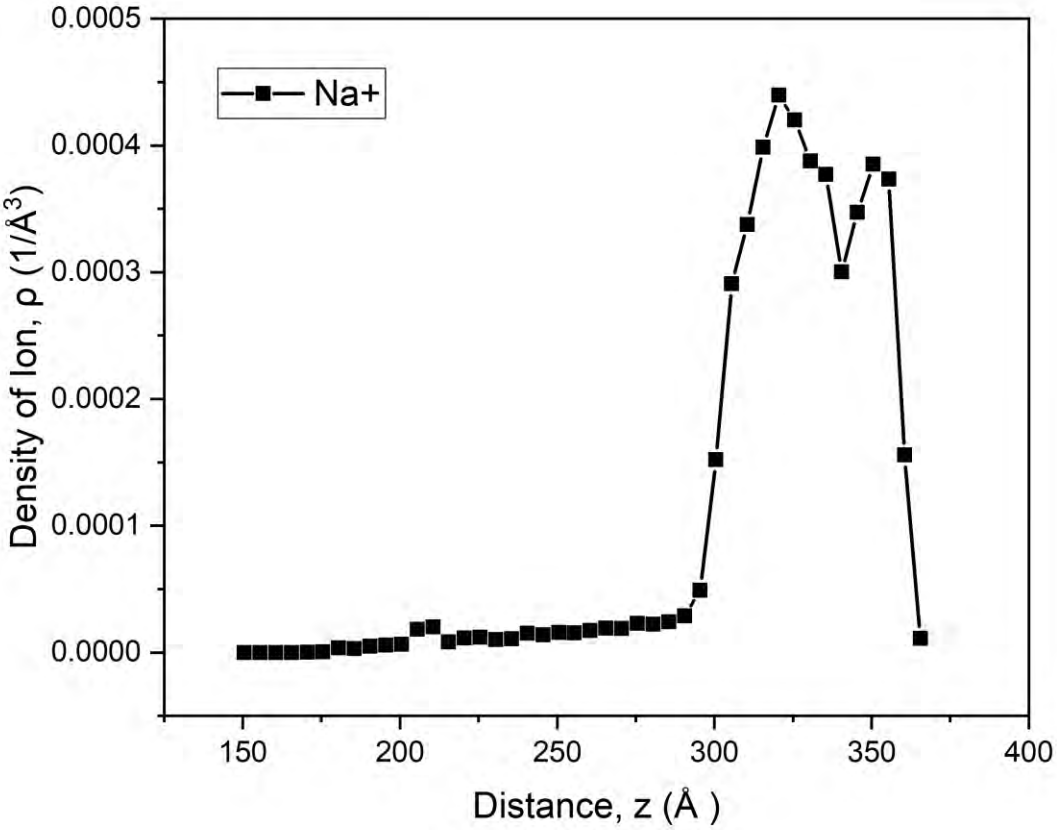

Fig 3. 4: Variation of Na^+ ion with for different spatial position

From the Fig 3.3 and Fig 3.5 it is evident that the Cl^- ions entered into the crumpled graphene anode. In the Grahame model, the impact of Helmholtz layers (HLs) is considered in the regions between the peaks and the electrode surface [115]. According to the standard GCS model, the ionic density steadily drops as the distance between the electrode surface and the nominal density in the bulk solution increases. This region is known as the diffusion layer. In the validated crumpled graphene model, the Inner Helmholtz layer (IHL) is up to 5 Å. The second peak is at approximately 50 Å from the starting of the anode, known as the outer Helmholtz layer (OHL). Similar pattern of the graph can be noticed at the Fig 3.4 where the density profile of Na^+ is drawn. Na^+ is attracted towards the negative electrodes. Cathode length ranges from 207.9 Å to 365.8 Å. Na+ moved towards the end of the cathode and gathered near the electrode surface.

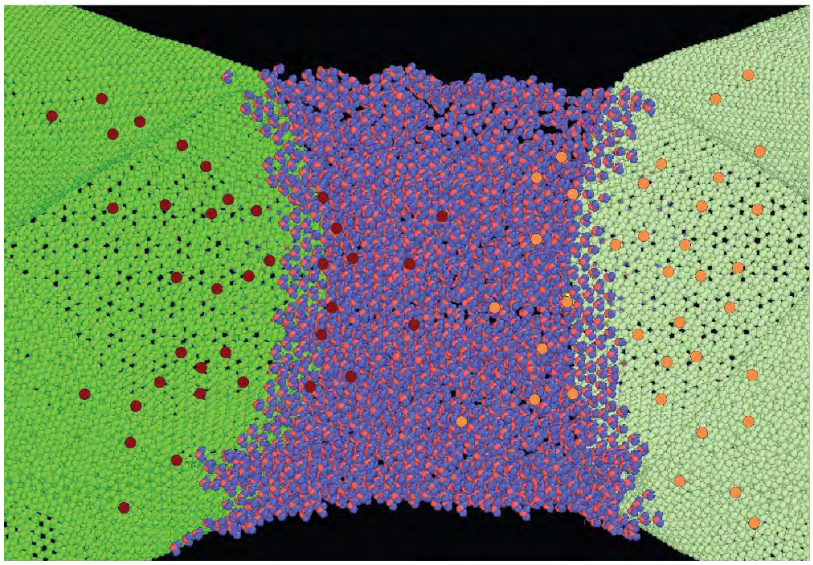

Fig 3. 5: Electrolyte ion tend to enter into the pore whereas solvents are moving towards the surface.

3.2.2 Behavior of Water Molecules

Figure 3.1 shows the peak density of water at a distance of roughly 4-5 Å from the electrode surface, as observed in the density profile. In the literature, it is frequently referred to as "the initial water layer" [118]. The hydrophobic graphene surface disrupts a continuous network of hydrogen bonds, resulting in the formation of this layer. Figure 3.1 shows that the density profiles of hydrogen atoms in the first water layer are slightly closer to the graphene surface than oxygen atoms, indicating that water molecules are present with one of their OH- bonds pointing in the graphene exterior direction.

Both the ions (Na^+ and Cl^-) entered into the electrodes because of the crumpled structure of the graphene which is depicted in the figures. The specific surface area (SSA) accessed by the ions is thus can be said to be increased from the planar graphene because of the structural change. However, water molecules could not penetrate into the electrodes rather it accumulated near the electrode surfaces, end surface for the anode and beginning surface for cathode. This phenomenon

can be explained in terms of energy. Because of the very high energy barrier inside the electrodes, water molecules did not have enough energy to overcome this. Whereas, because of the ionized form and ion size, both cation and anion could make their way inside the electrode. Due to the preponderate charge accumulating ability inside the electrodes, cation and anion have been separated in larger numbers. which would benefit the charged electrodes' effective screen effectively energy storage capability of the supercapacitor.

3.2.3 Performance Parameter Analysis:

The capacitive characteristics of EDLCs are influenced by the ion distribution near the electrode surface as well as the amount of electrolytes accumulating at the interface [119]. A coefficient of d was used to address the effective positioning of counter-ions at the EDLC-dominant area. In this model the d has been calculated and the value is 38.8291 Å, which in terms of % basis, it was found about 63.5% thickness. According to the Fig 3.3, the density fluctuations of Cl- have been flattened out after around 60 Å. From a previous literature, EDL Thickness was found 7.2 Å where density fluctuation disappeared after 10Å from the electrode. So, %EDL Thickness was found to be near 72% which is pretty close to this study, slightly higher. Because of the planar structure the ions accumulate in a slight dispersive manner than the crumpled structure which makes the double layer thicker. This result indicates a rather compact accumulation of counter-ions leading to a thin EDLC thickness.

The measured specific capacitance value for this particular model is 16.351 $\mu F/cm^{-2}$ which is around 406% higher than planar graphene electrodes. [112]. This increased value is due to some reasons. Because of the 3-D structure of the crumpled graphene the surface area increases significantly. Which ensures the more interaction between solvent and electrode surface. Apart from that as in the crumpled model, some ions could enter into the pores, improving the overall attraction. Again, in the crumpled model the EDL thickness is quite thin than the planar one. From literatures, it is known that thinner EDL has a favorable impact on the EDLC performance. So, all these factors contribute towards an exceptional enhancement of specific capacitance.

3.3 Effect of Crumpling State of the Graphene Electrodes

As stated in the chapter 2, three additional models have been developed with different crumpled radius (165.4Å, 110.1Å and 89.5Å) to compare the energy storage performances among them. The crumpling of the planar electrode started from an initial radius of 212Å and in the course of simulation this radius was shrink. The above mentioned three radius denotes three different stages of crumpling. 165.4 Å represents the initiation of crumpling, whereas 110.1Å shows half way through the fully crumpled stage. When the radius is reduced to 89.5Å it looks almost fully crumpled-like structure. The model discussed in 3.2 has a radius of 68.3Å which portrays the complete crumpled stage, round paper-like structure. Different states were studied to examine how different crumple structure affects the energy storage behavior of supercapacitor. This section will discuss elaborately about the effect of crumpling state on supercapacitor performance.

3.3.1 Influence on Interaction between Electrode-Electrolyte

Fig 3.6 demonstrates that the density peak near the electrode surface tends to be enlarged as the radius is diminished. This refers to less charge accumulation ability for larger radius crumpled model. Larger radius crumpled model portrays the model when crumpling process is initiated or at an early stage. The density peak for Cl^- 89.5Å model was observed at z=70 Å and the value of the peak is 0.000195 $1/Å^3$ whereas for the fully crumpled structure the peak is around 0.0004Å which is around 50 % higher at a shorter distance from the anode. The more the radius gets reduced, the more the model turns into complete crumpled form or paper-like structure. This ensures tighter packing of the ions near the electrode surface which is exactly what Fig 3.5 indicates. For radius 165.4Å, though it possesses higher apex for ion density than radius 110.1Å, in the latter case the solvent access area is pretty much more than the former one. This is because ions can enter into the electrode which is not in the case for radius 165.4Å. 165.4Å is more like a 2-D like structure which is forming to a 3-D like structure after a while.

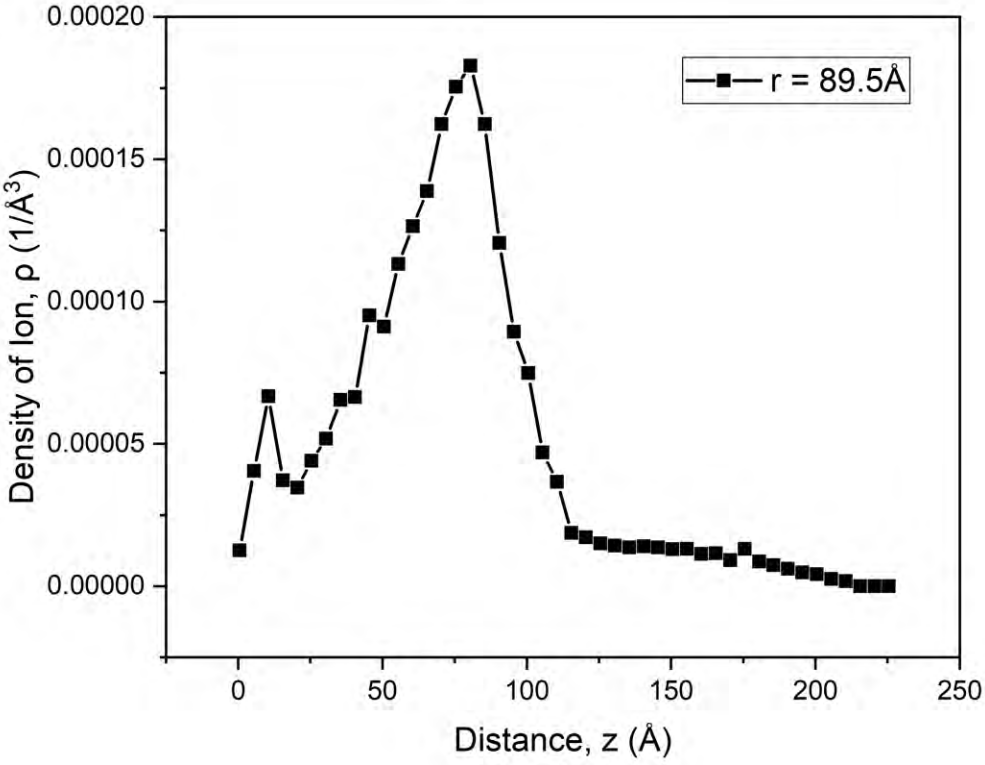
r = 89.5Å
Density of Ion, ρ (1/Å^3)
0.00020
0.00015
0.00010
0.00005
0.00000
0
50
100
150
200
250
Distance, z (Å)

(a)

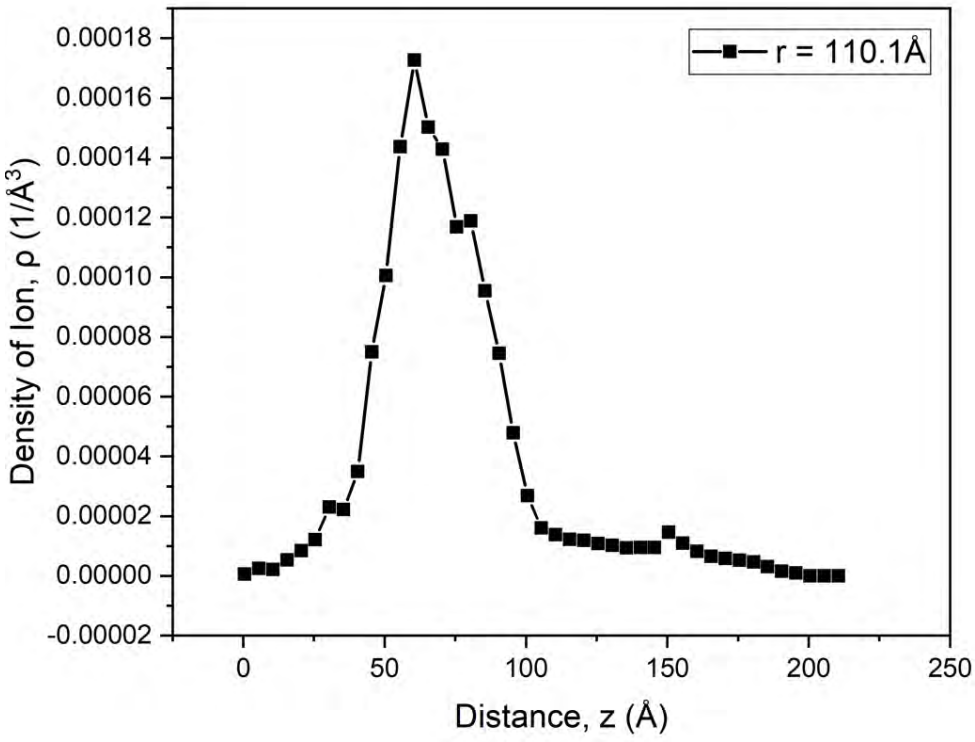
r = 110.1Å
Density of Ion, ρ (1/Å^3)
0.00018
0.00016
0.00014
0.00012
0.00010
0.00008
0.00006
0.00004
0.00002
0.00000
-0.00002
0
50
100
150
200
250
Distance, z (Å)

(b)

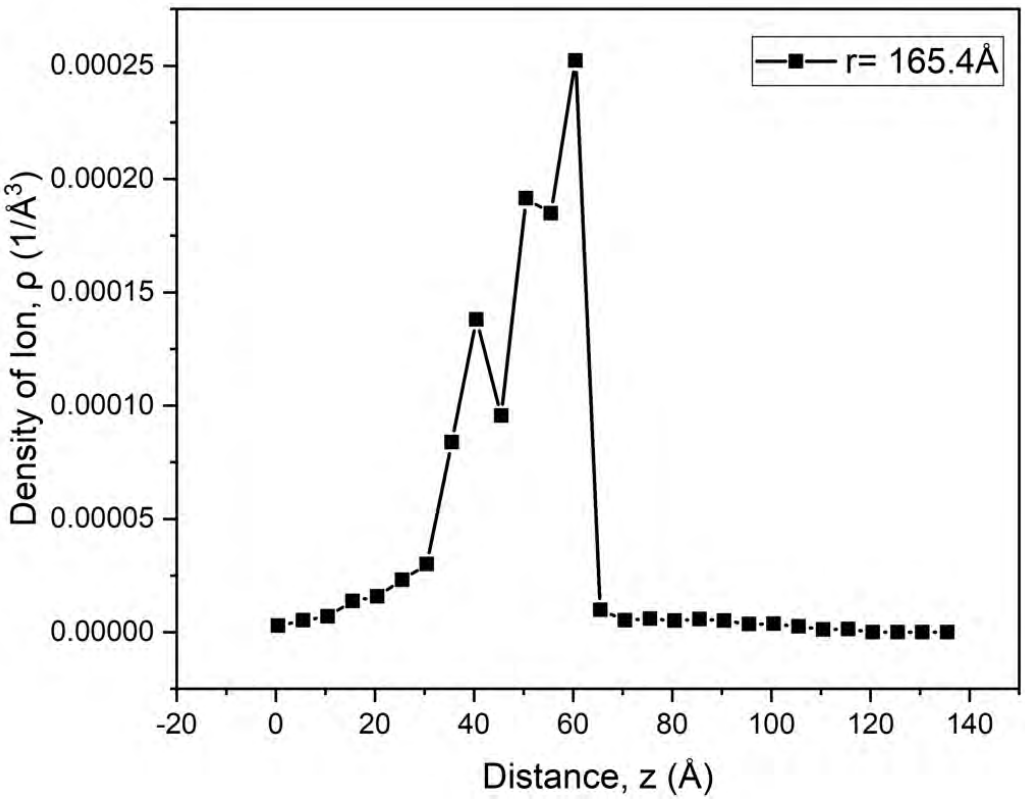

(c)

Fig 3. 6: Density profile of Cl^- for (a) r=89.5Å (b) 110.1 Å and (c) 165.4 Å crumpled states.

Similar pattern can be observed for Na^+ ions from the Fig 3.7. However, Na^+ ions are attracted towards the cathode in a stronger way than the Cl^- ions as slightly higher density peak is observed for Na^+. Another reason behind this is the size of the cations are slightly smaller than the anions due to which cations pile up in a tighter packing than the anions.

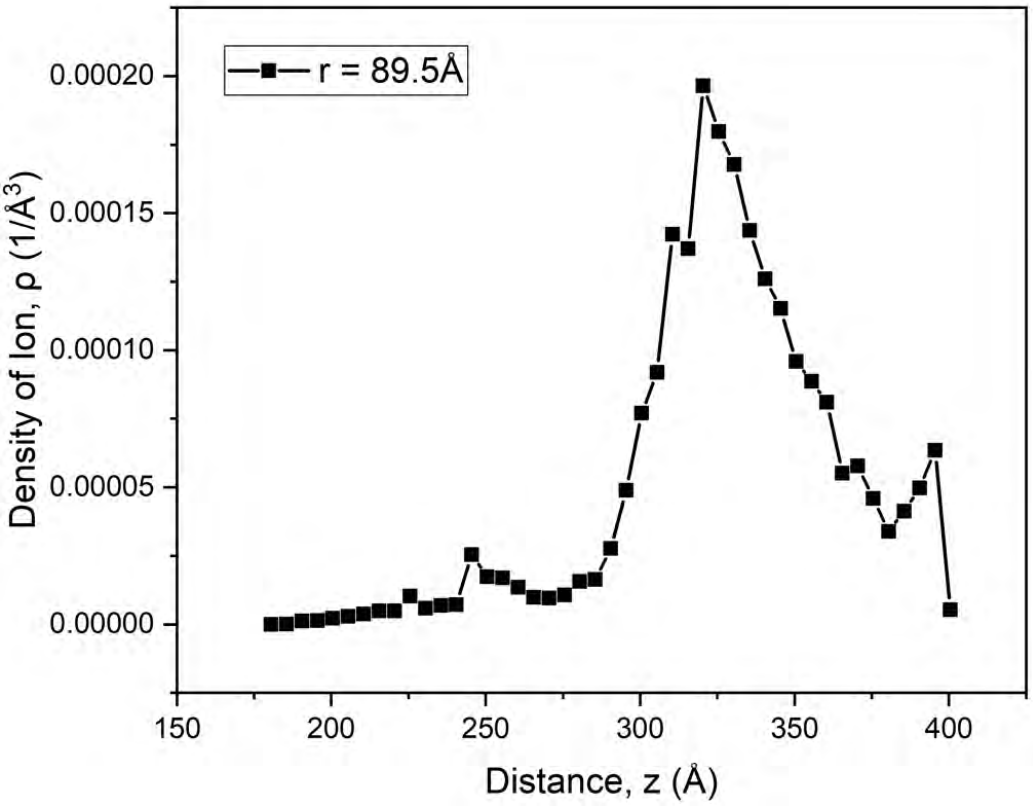
r = 89.5Å
Density of Ion, ρ (1/Å^3)
0.00020
0.00015
0.00010
0.00005
0.00000
150
200
250
300
350
400
Distance, z (Å)

(a)

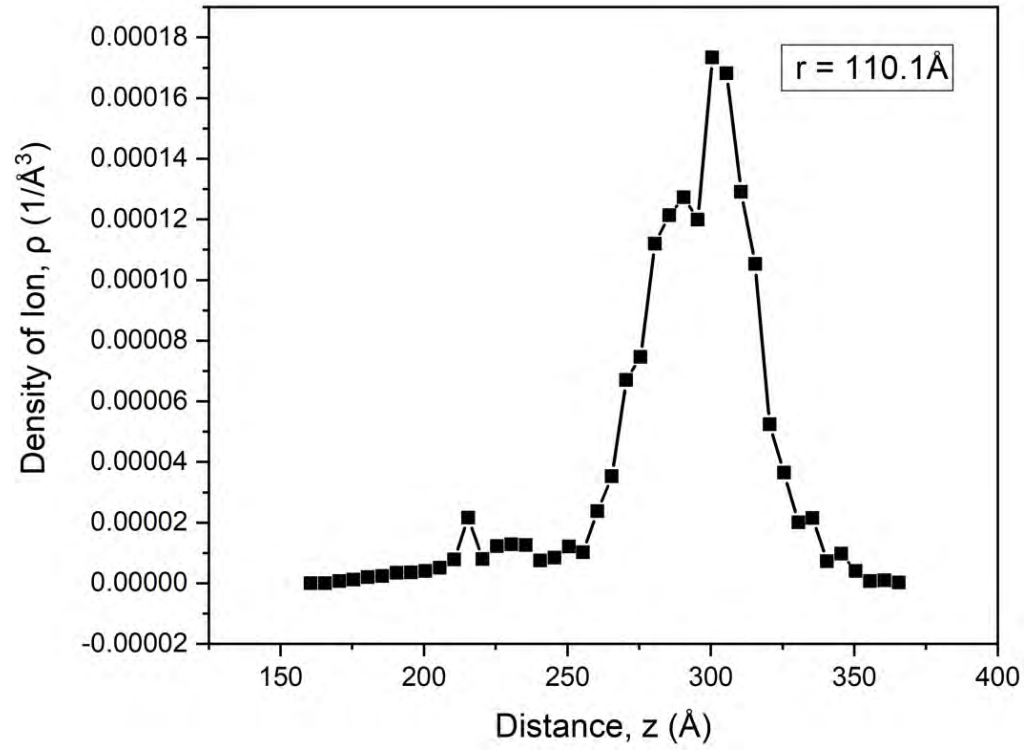
r = 110.1Å
Density of Ion, ρ (1/Å^3)
0.00018
0.00016
0.00014
0.00012
0.00010
0.00008
0.00006
0.00004
0.00002
0.00000
-0.00002
150
200
250
300
350
400
Distance, z (Å)

(b)

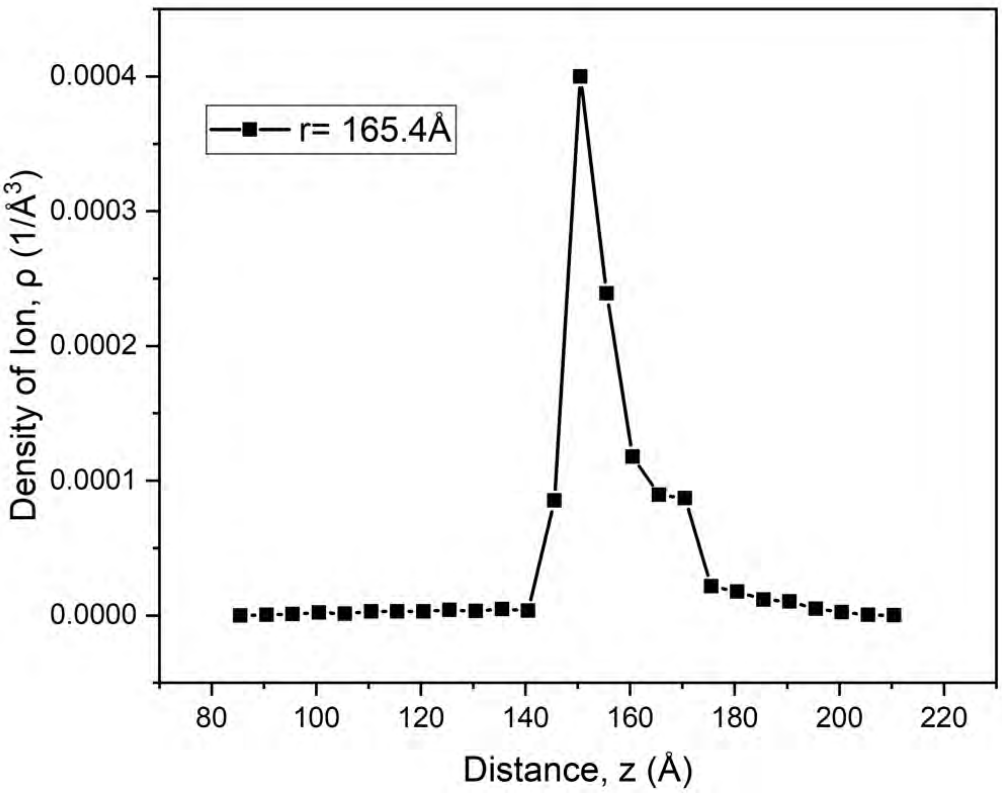

(c)

Fig 3. 7: Density profile of Na^+ ion for (a) r=89.5Å (b) 110.1 Å and (c) 165.4 Å crumpled states.

3.3.2 Interactions between Electrode and Solvent

By comparing the density profiles of water molecules, the explanation gets clearer. As seen in the Fig 3.8 as the model becomes fully crumpled-like state, water molecules become more orderly oriented form. From the post-simulation visualization, it was seen that water molecules were almost parallel near the electrode for higher radius model which in turn contributed towards better charging ability. This can be further elucidated from the Fig 3.8 that distribution of the water molecules is rather oscillatory in the greater radius case while in the 89.5Å radius case the distribution resembles like the fully crumpled graphene model.

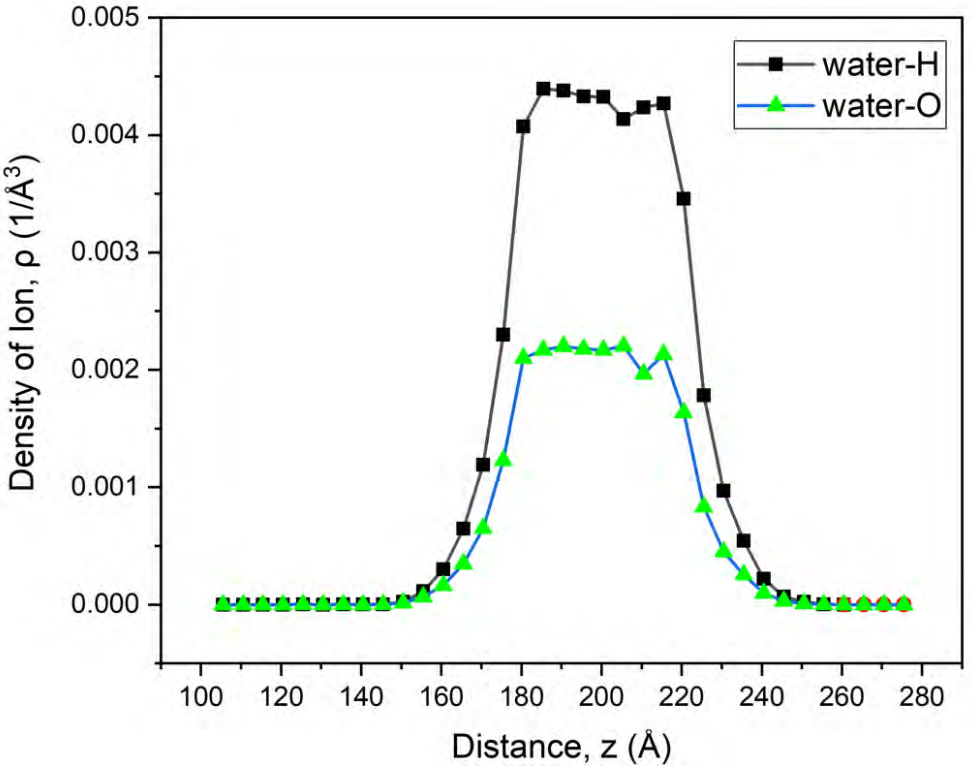
water-H
water-O
Density of Ion, ρ (1/Å^3)
0.005
0.004
0.003
0.002
0.001
0.000
100
120
140
160
180
200
220
240
260
280
Distance, z (Å)

(a)

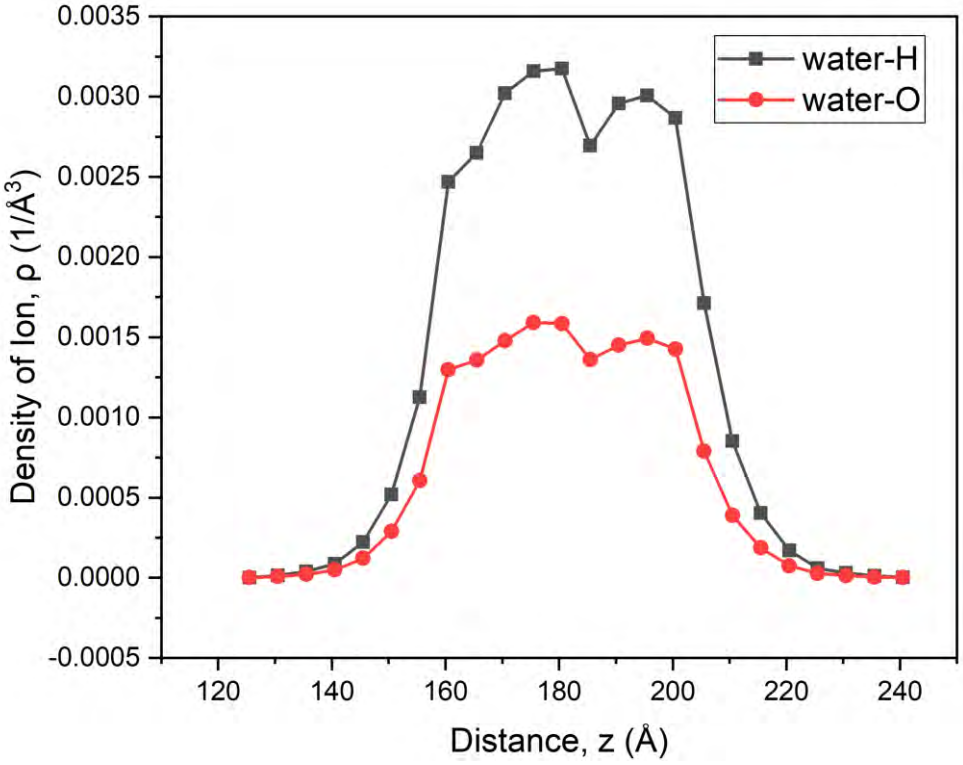
water-H
water-O
Density of Ion, ρ (1/Å^3)
0.0035
0.0030
0.0025
0.0020
0.0015
0.0010
0.0005
0.0000
-0.0005
120
140
160
180
200
220
240
Distance, z (Å)

(b)

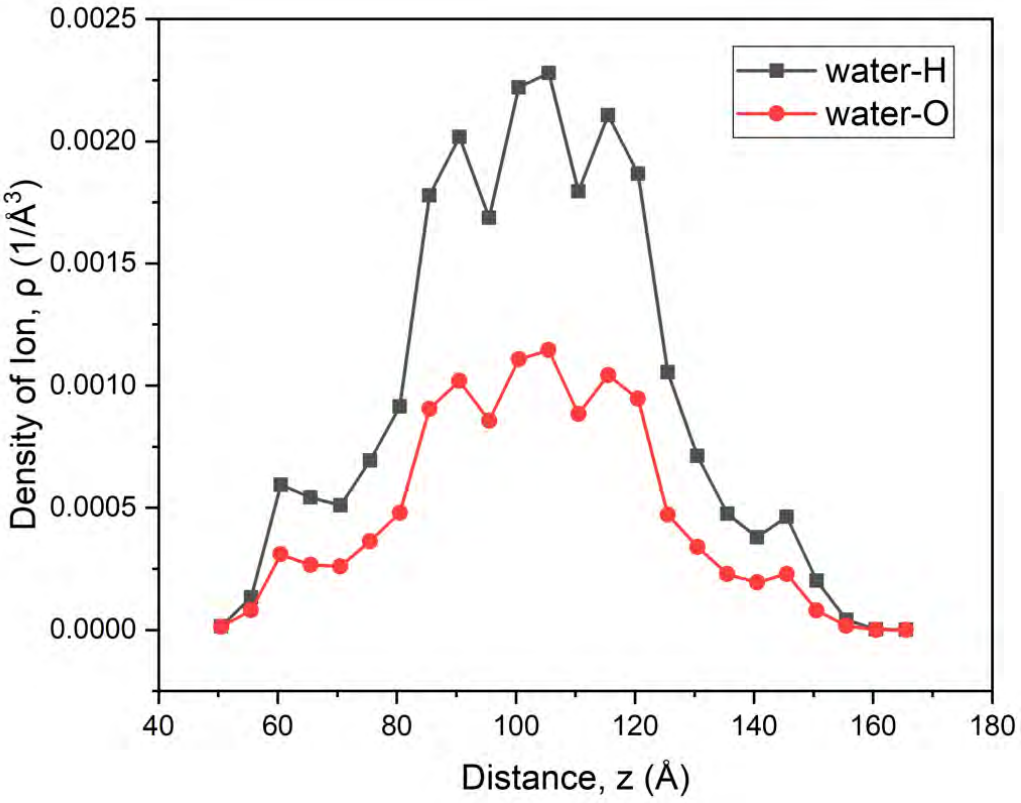

(c)

Fig 3. 8: Density profile of water for (a) r=89.5Å (b) 110.1 Å and (c) 165.4 Å crumpled states.

Highest Oxygen atom population in the bulk region is observed for 89.5Å radius. The desnity for hydrogen and oxygen possess a value of 0.0021 $1/Å^3$ and 0.0045 $1/Å^3$ which is more than 50 % higher than the other two models. It is noted that the magnitude of the density peak of H atom is doubled the value of O atom for obvious reason, H atom being double in numbers.

3.3.3 Impact on EDLC Energy Storage Ability

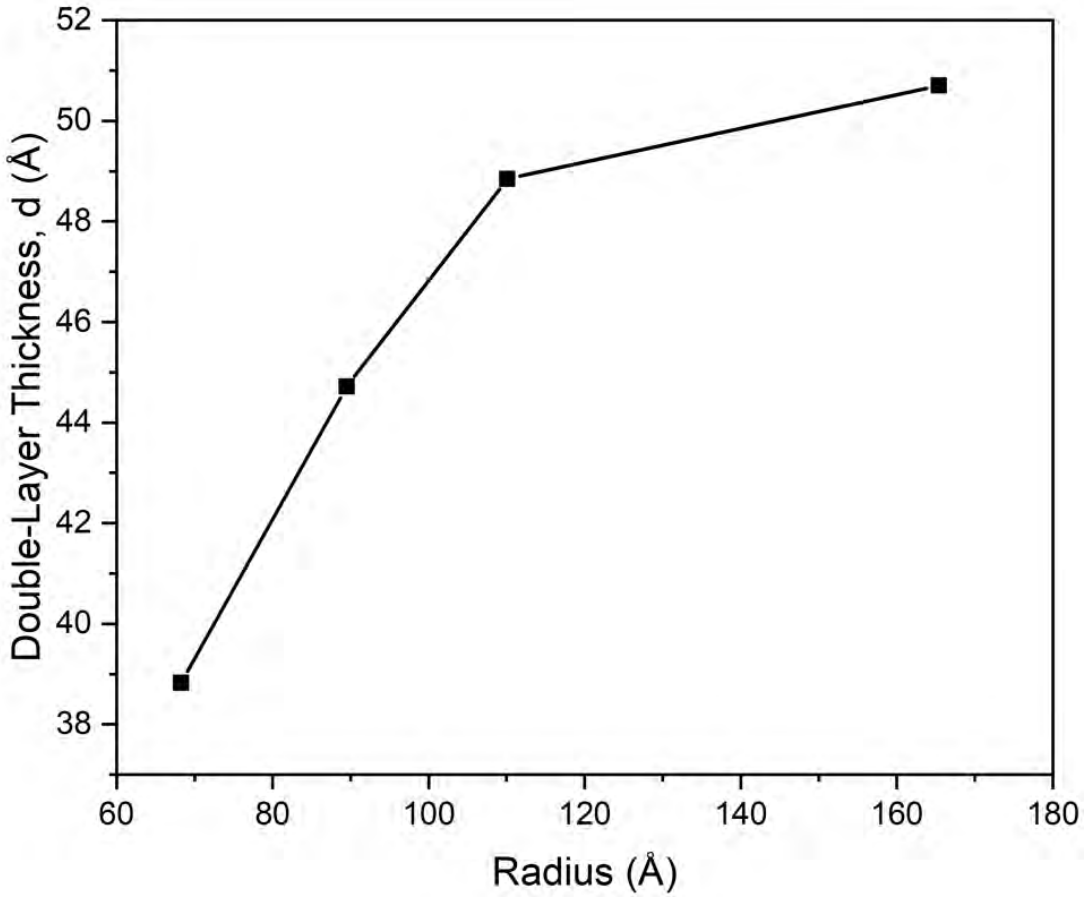

Fig 3. 9: Variation of EDLC thickness with different degree of crumpling state.

Fig 3.9 depicts the EDLC thickness scenario for different models. The result it showed is highly expected. Thinner double layer is formed in case of more crumpled like structure which amplifies the EDLC performance. For the r=165.4 Å model the thickness is around 51Å which is 69% if measured in % basis slightly better than the planar electrode but degraded value in comparison to other crumple configurations. One of the few reasons for this is a dispersive and oscillatory distribution of anions and cations considered from electrode surfaces.

Figure 3.10 shows the potential curves for EDLC models with different degrees of crumpling of the graphene electrode. In each case, a trend is noticed that near the electrode surface electrical

potential tends to rise up due to the faster diffusion of the charges to the electrode surfaces. Total voltage consists of two parts, one from electric double layer contributed from the ion-electrode interaction and another from the polarized water solvents. The difference between them represents the cumulative voltage. First of the increased voltage is due to the U_{ion} whereas a potential drop is detected in a bulk like area (bit far from the surface as the electrode surface begins at 0 for all cases) because of lack of ion storage and higher population of water solvents Total potential descends as the radius is increased. This fully satisfies the observation of density profiles. A monotonic increase trend of the specific capacitance with increment of radius is illustrated in the Fig 3.11. Complete crumpled state ensures better packing efficiency which denotes larger and rapid ion transports towards electrode, in other words improved electrode-electrolyte interaction. Higher solvent accessible area, 3-D architecture attributes towards the magnified performance of the supercapacitor.

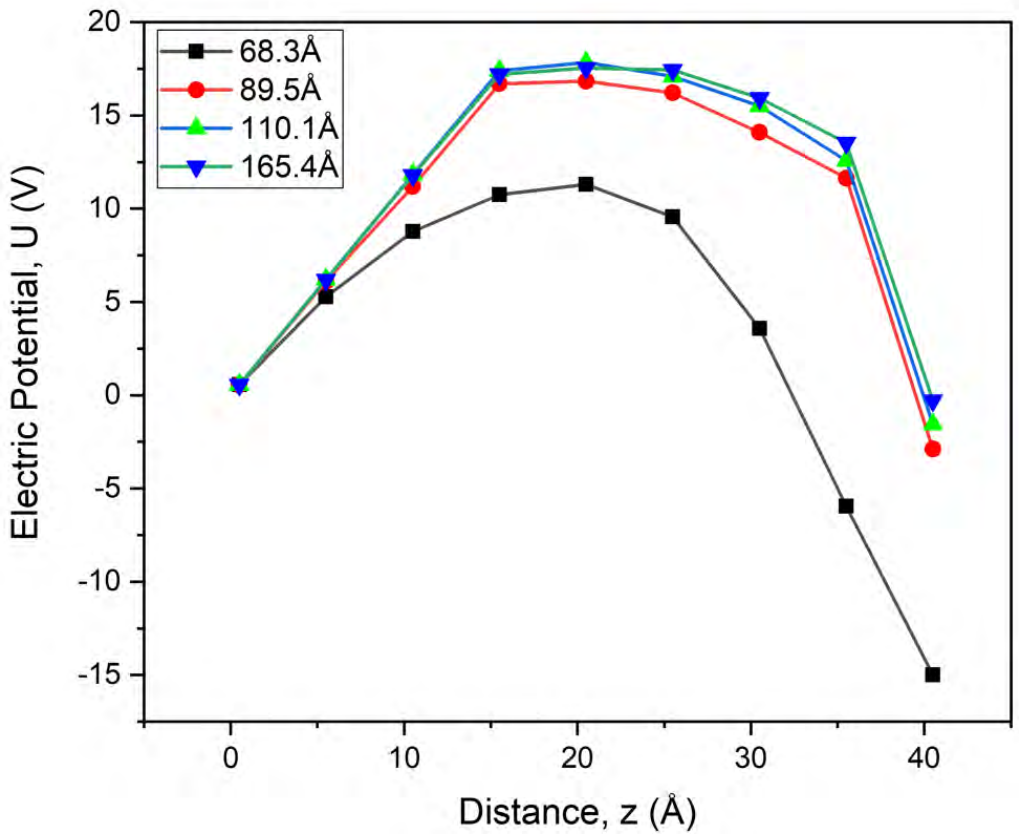

Fig 3. 10: Distribution of potential values with spatial distances at different crumpled states

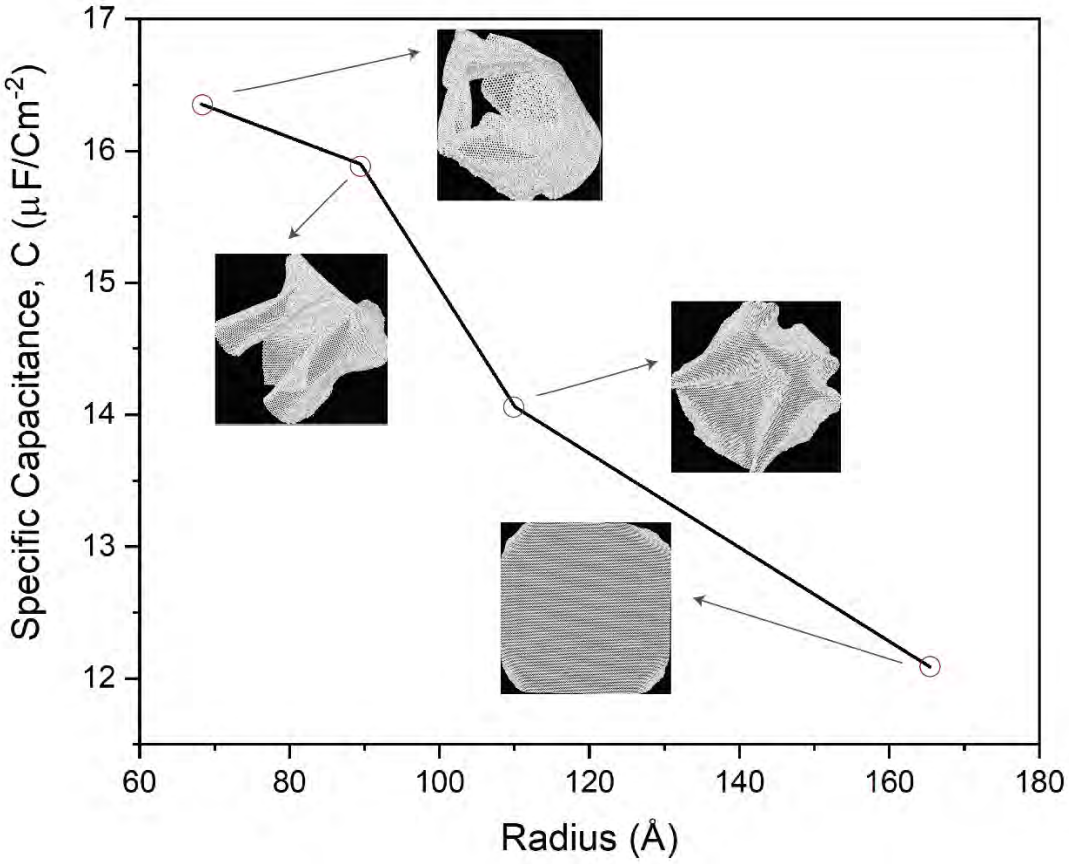

Fig 3. 11: Distribution of specific capacitance with varied crumpled radius

Performance comparison can be made more clearer from the Table 3.1 below:

Table 3. 1 Comparison of performances for different electrode configuration

Electrode Configuration	d (Å)	d (% basis with respect to the electrode)	C (μF/cm^{-2})	% Increase of C
Planar	7.2	72	3.28	-
r = 165.4 Å	51	69	12.21	272
r = 110.1Å	48.5	67	14.15	331
r = 89.5Å	44.5	65	15.92	385
r = 68.4Å	38.8291	63.5	16.351	406

It is obvious that all the crumpled configuration shows improved capacitance but among them the fully crumpled-like configuration possesses the best performance.

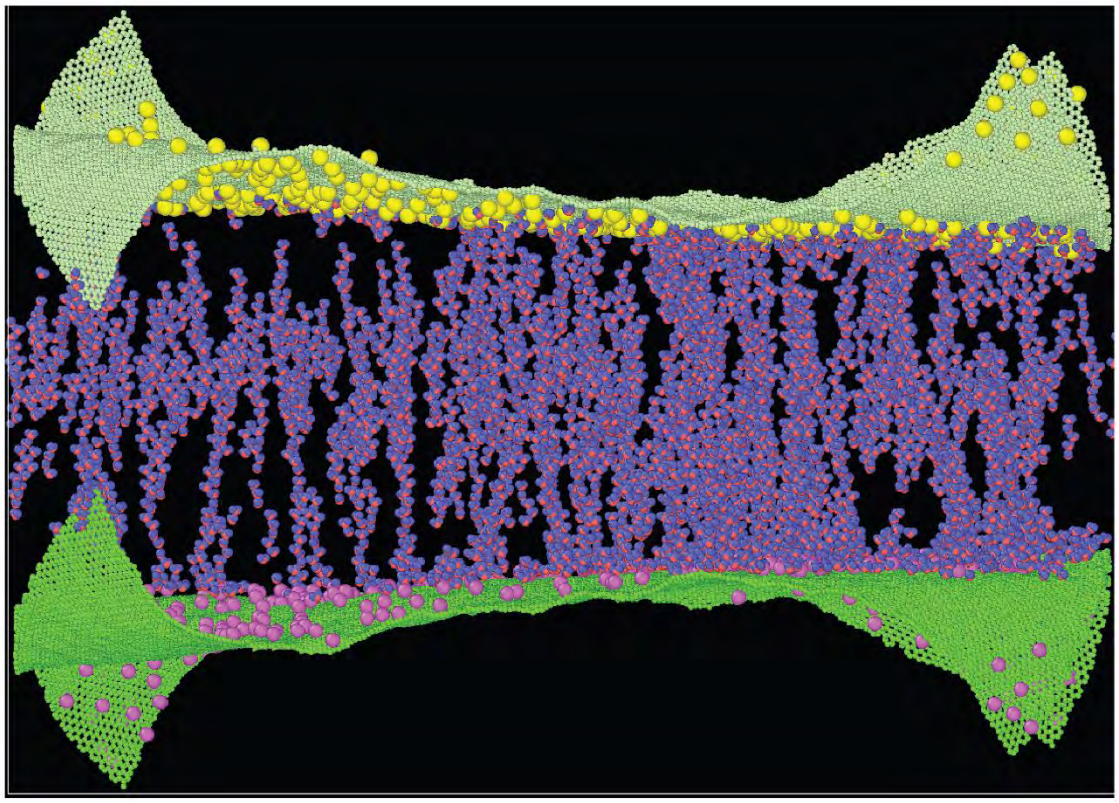

Fig 3. 12: Simulation domain showing electrolyte ions accumulated in electrode surfaces.

In the Fig 3.12 a visualization for the r=165.4Å is represented. It shows in this state, electrolyte ion could not penetrate the electrode surface like the other models rather all these ions accumulate near the surface and some on the bend of the graphene sheet. But because of the larger surface area and bends it is way better than the planar graphene electrode. Nearly complete separation of the ions is seen in this case also which brings greater performance of the EDLC supercapacitors.

3.4 Supercapacitor Performance of Crumpled Graphene with Defects

As mentioned in the chapter 2, the crumpled graphene model (r=68.3Å) was modified by adding different number of defects on the electrode surface. The effect of this inclusion of defects on the supercapacitor performance is analyzed here. Porous materials have been studied to be very effective as electrodes by accommodating more ions and minimize the energy barrier for ions. For this reason, various number of defects was added in the electrode structure. 5%, 10%, 20% and 30% defects (% in terms of surface area), are the 4 cases taken to incorporate the effect of defects in the existing model.

3.4.1 Variation of Ion and Solvent Distribution with Different Amount of Defects

Figure 3.13 represents the density profile of Cl- with the varied number of defects. Like previous density profiles two density peak can be observed. The Fig 3.13 delineates that for defects 20%, the first peak is highest which is developed from about 5 Å distance from the electrode. The magnitude of the first density peak for Cl^- is 0.0032 $1/Å^3$ which is developed at the Inner Helmholtz layer. Almost in all electrodes consisting varied number of defects shows IHL from 5 Å distance from the anode. However highest density peak is formed for 20% pore, then 10%, 5% subsequently. The density peak is found lowest for 30% defects. The second peak value for 20% and 10% almost coincides whereas for 5% it is developed a bit farther than the mentioned two cases. Almost similar trend is portrayed in the Fig 3.14 for Na+. The highest charge accumulation can be seen at 20% defects. This interesting phenomenon can be described in terms of minimization of energy penalty and rapid-transport pathway created by nanometer pores.

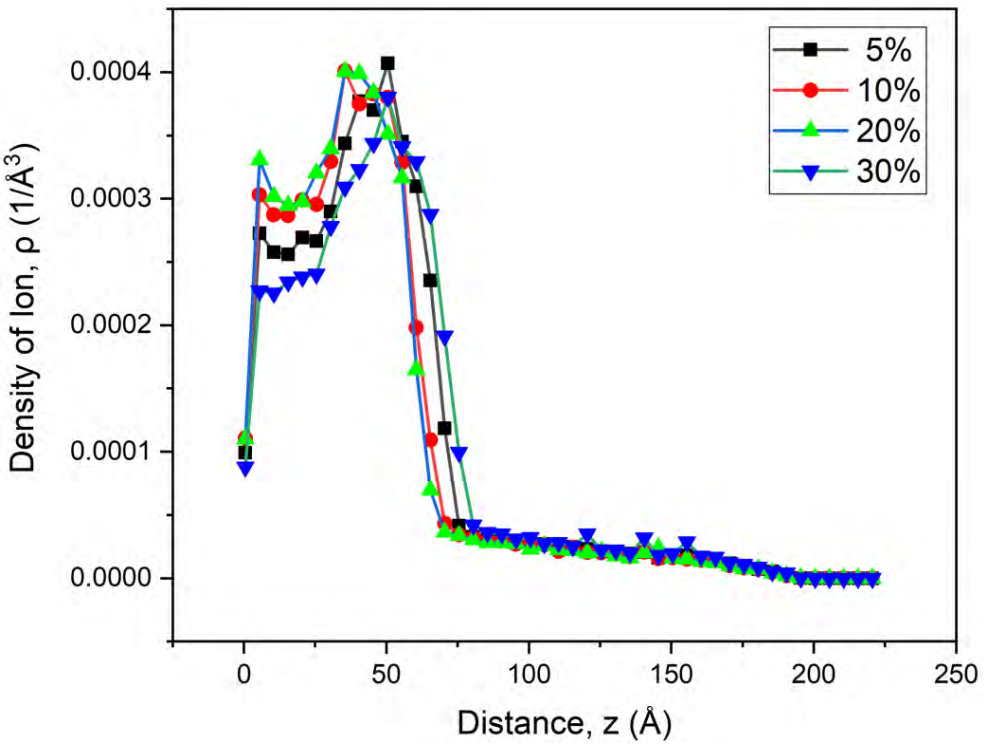

Fig 3. 13: Density profile of Cl^- for different electrodes consisting varied amount of defects (in % of the surface area)

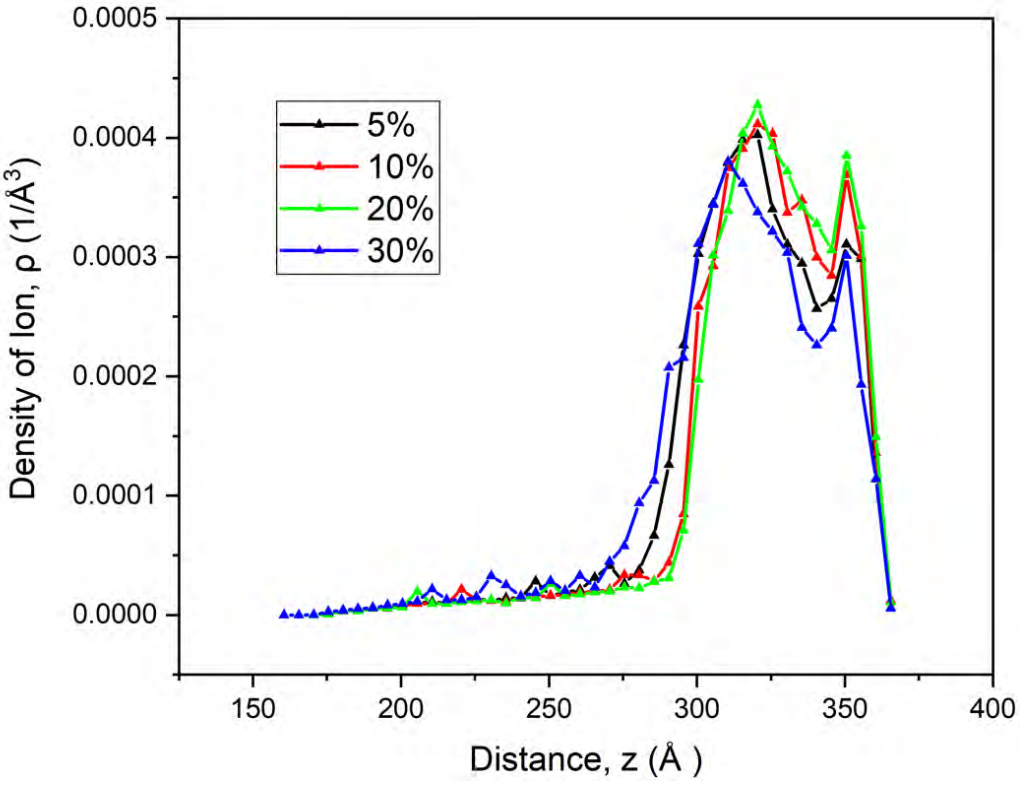

Fig 3. 14: Distribution of cations from different distance of electrodes consisting 5%, 10%, 20% and 30 % defects. respectively

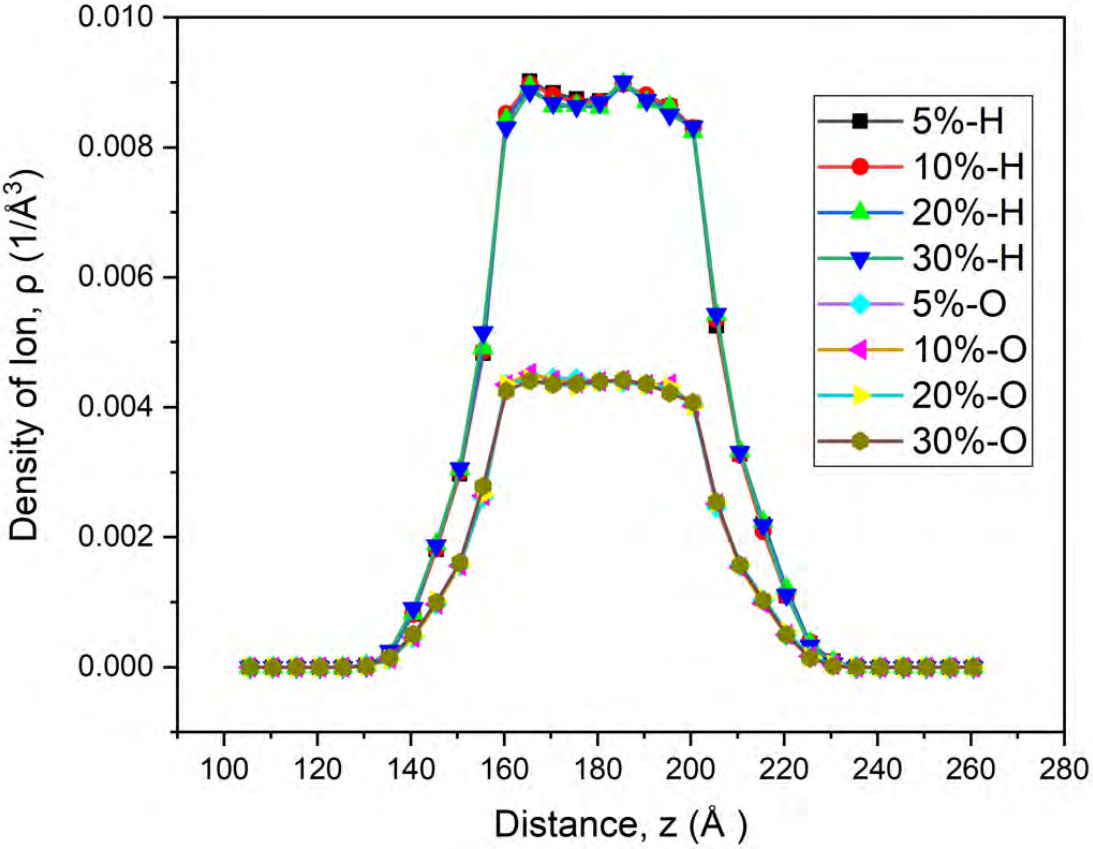

Fig 3. 15: Similar pattern of water molecules accumulation near electrode surface for different defects levels.

The hydration shell must be gently disrupted in an optimal fashion to reduce the energy penalty when entering the pores. Ions, according to Gogotsi et. al can infiltrate sub-nanometer pores once the hydration shell is lost [98]. As there are pores in graphene surface, ions can overcome the energy barrier and easily enter into the electrode. That is why density peak increase when the amount of defects is increased from 5% to 20%. However, a decrease in vertex surprisingly be seen for 30% defects. This is because of the excessive pores the contact area of electrodes reduces significantly. Along with that, as the number of pores is higher, some pores are larger than necessary for losing hydration shell shown in Fig 3.19. A rather thicker double-layer is formed in

this case. Density profiles of water molecules however do not show much variance with the alteration of amount of defects which is depicted from Fig 3.15.

3.4.2 Comparison of EDLC Performance of Various Porous Electrodes

In this section, EDLC performance parameters will be discussed for different defects levels. Free-energy, double layer thickness, partition co-efficient, electric potential and finally specific capacitance will be explored.

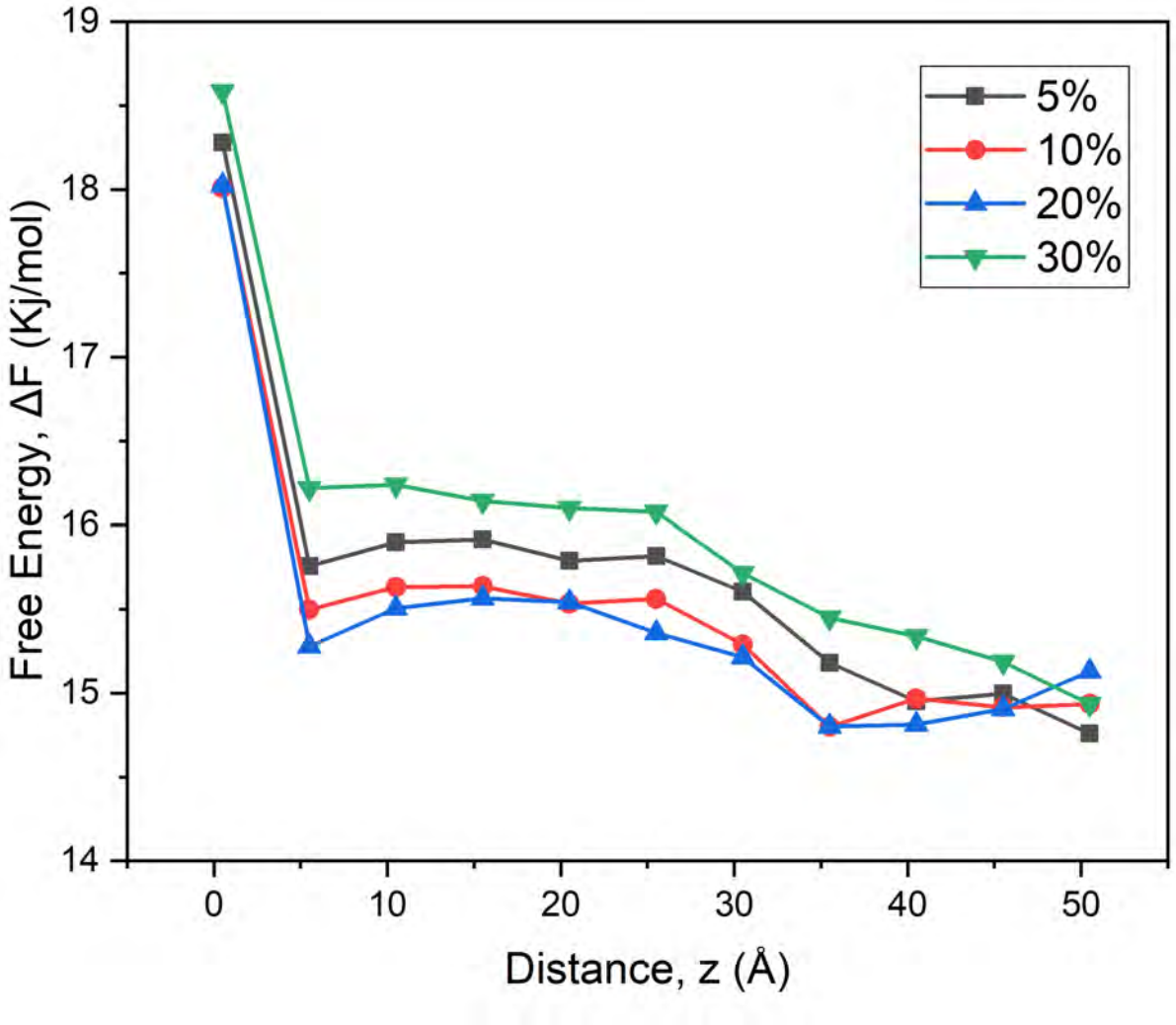

Fig 3. 16: Free-Energy scenario with spatial position of different porous crumpled electrode.

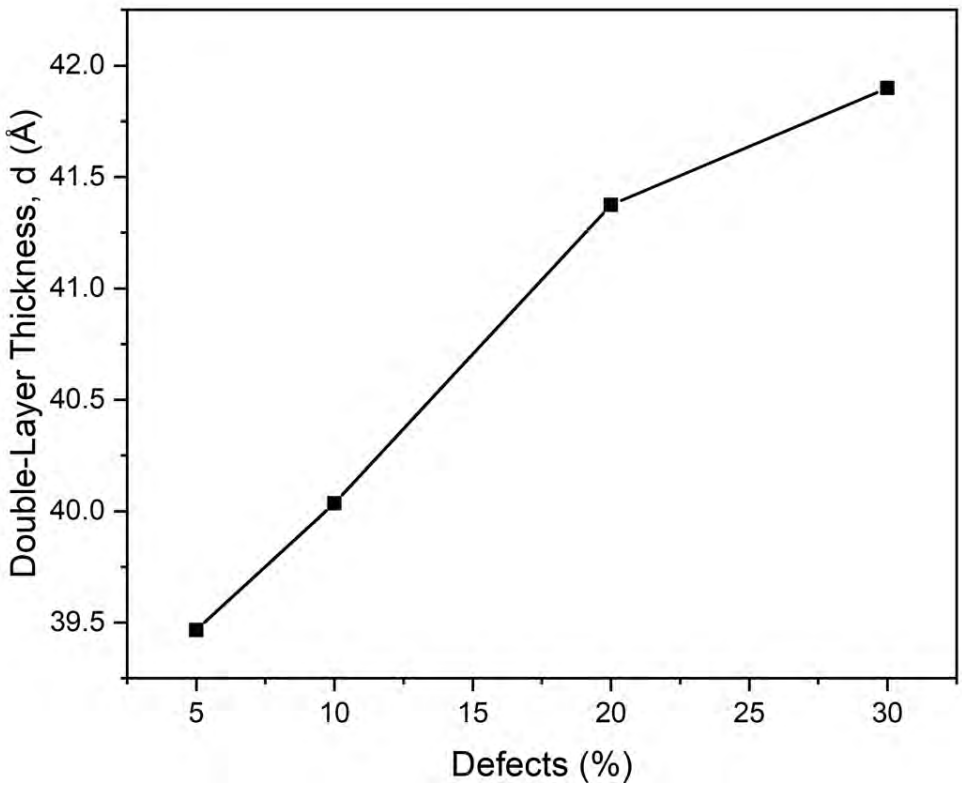

Fig 3. 17: Incrementation of Double layer thickness with increased amount of defects.

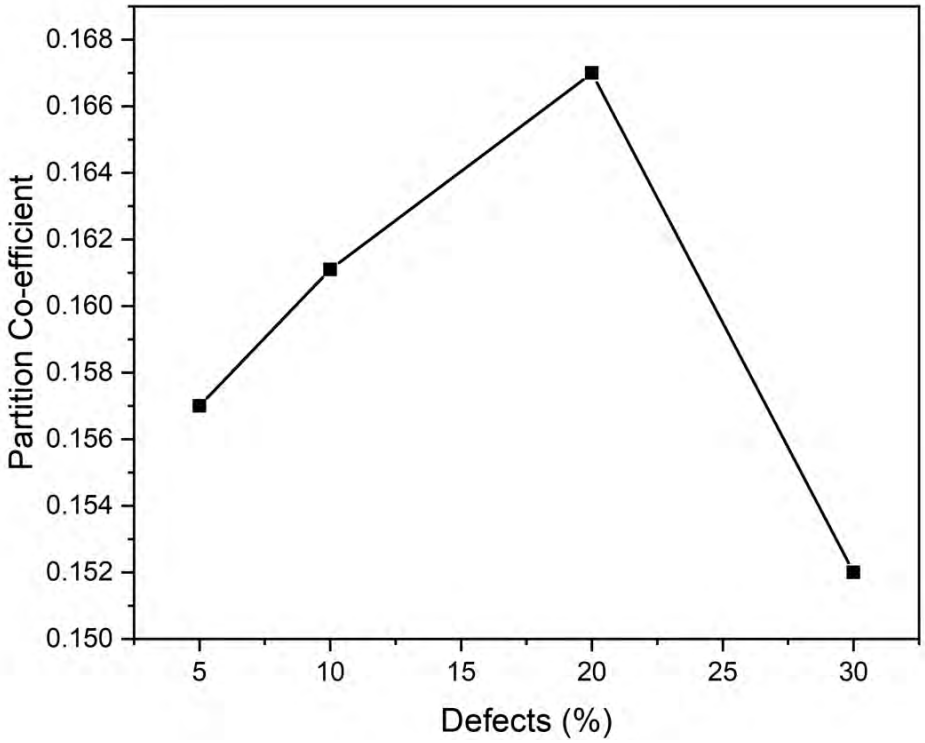

Fig 3. 18: Impact on Partition co-efficient for different levels of defects-based electrodes.

From the Fig 3.16 is clear that decreasing trend of free-energy is observed for 5% defects level to 20% defects level-based electrodes. For 20% defects level, the minima of free-energy is found at 5 Å for a value of 15.1 Kj/mol. This is the exact location where the IHL develops. Lowest minimum energy indicates highest accumulation of ions which is well coincided with the density profiles got from the simulation in this case. For 30% defects it is maximum which corresponds to the lower peak leading to reduced capacitive ability The minimum free-energy for 30 % defects is 7% more than the minimum free-energy for 20% defects level.

A very interesting phenomena is seen from Fig 3.17. Although density peak shows at 20% defects levels, a monotonic increase for double layer thickness is observed with increased amount of defects levels. This is understandable as lower amount of pore somehow provides smaller region to accommodate which in turn creates a thinner double layer. From the figure it can be noticed that thinnest double layer formed for 5% defects level at a magnitude of 39.5Å whereas for 20% defects level it possesses a value of 41.5 Å.

Partition Co-efficient is the proportion of ionic concentration in the pore (C_{pore}) to that in the bulk (C_{bulk}). C_{pore} is determined by counting the amount of electrolyte ions and water molecules inside the pore of the electrode while C_{bulk} is determined by counting them outside the pore [120]. The highest performance of EDLC is found when the pores are neither too big nor too narrow for the simulated domain, we investigated which is for 20% defects shown in Fig 3.18. The best design of electrodes is linked to the properties of hydrated and non-hydrated ions, as well as their ability to attract each other due to the electrostatic effect. The size of pores has a direct influence on the partition coefficients achieved. As for 30% defects because of the oversized pores partition co-efficient holds the lowest value among them, which clearly proves the above-mentioned fact.

Fig 3.19 narrates that, as the number of pores is increased in the electrode it eventually increases the size of the pores too. Narrower pores are found at 5 % defects levels where the largest is at 30% defects level. It is very important to possess a balance between the size of the pore and size of the ions. The optimum scenario is when the size of the ions coincides with the pore sizes. From above results it can be said that in this case, 20% defects-based electrodes show the optimum result.

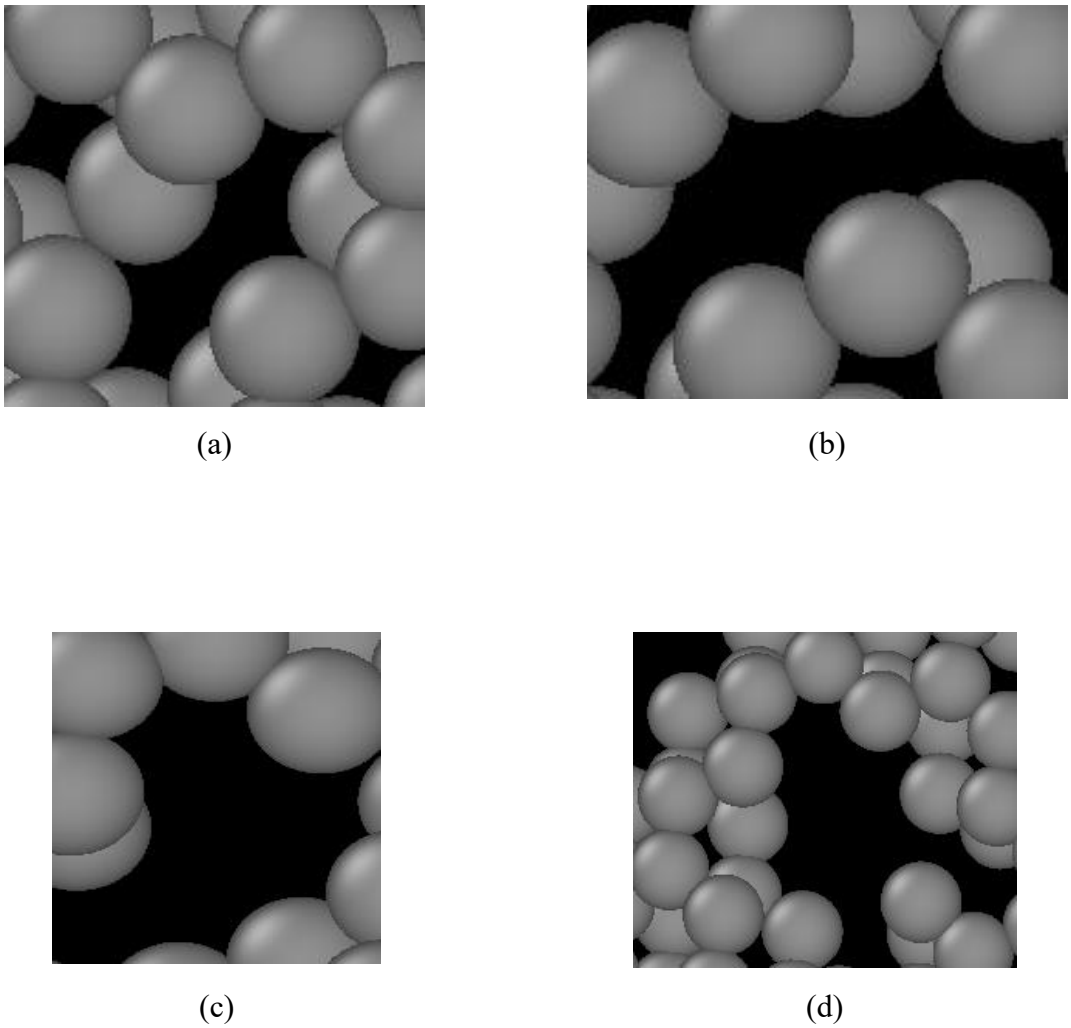

Fig 3. 19: Magnified views of electrodes consisting (a) 5% (b) 10% (c) 20% and (d) 30% defects.

Fig 3.20 portrays potential distribution whereas descend of potential is found for higher defects level-based electrodes except for 30%. The peak voltage of 10V ensures a considerable amount potential whereas the further drop ensures higher capacitance.

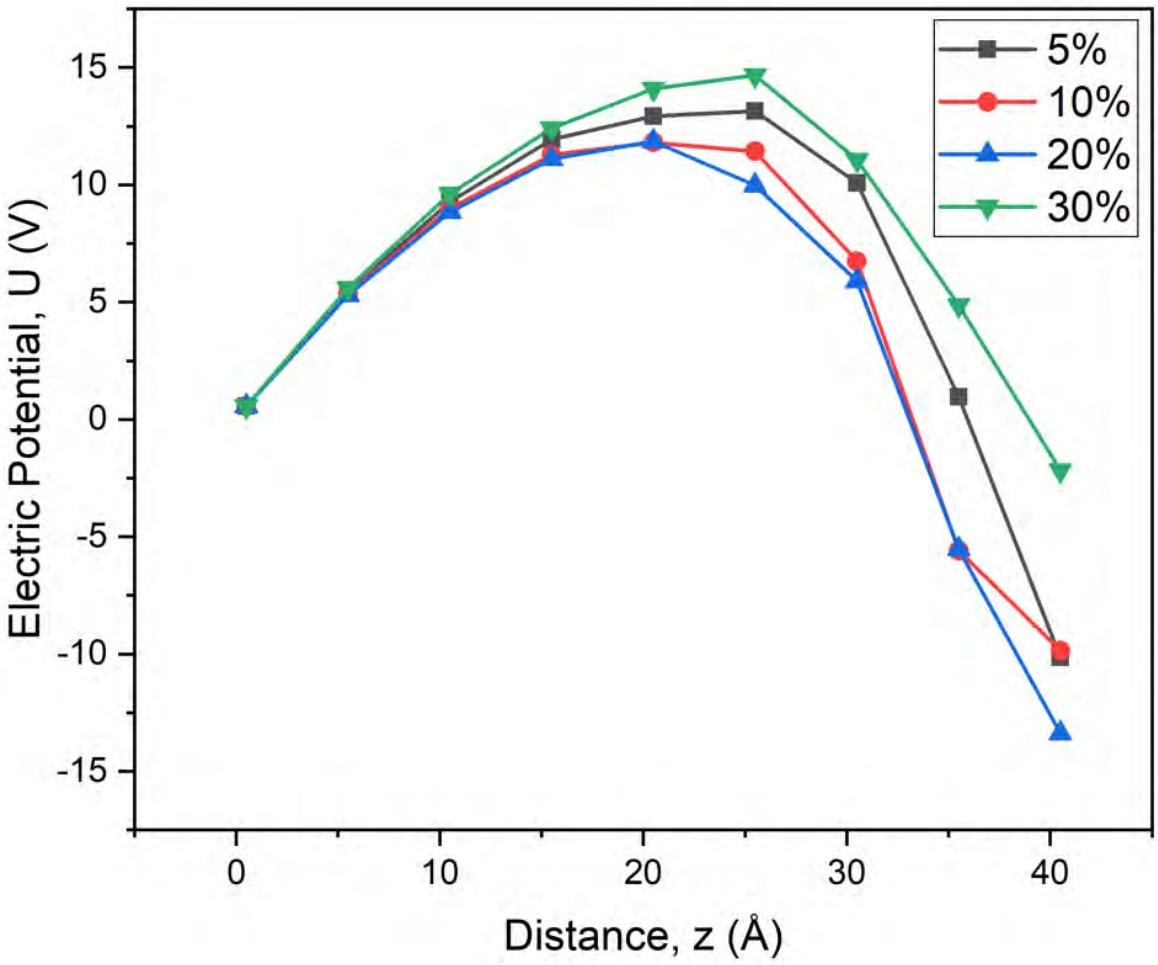

Fig 3. 20:Greater potential drops for 20% defects-based electrode.

Comparison of performance is shown in the table 3.2 below for different level of defects

Table 3. 2 Variation of capacitance for different level porous electrode based EDLC

Defects (%)	**C (μF/cm^{-2})**	**% Increase**
0	16.351	--
5	17.2	5
10	17.7	10
20	19.8	21
30	16.323	-0.17

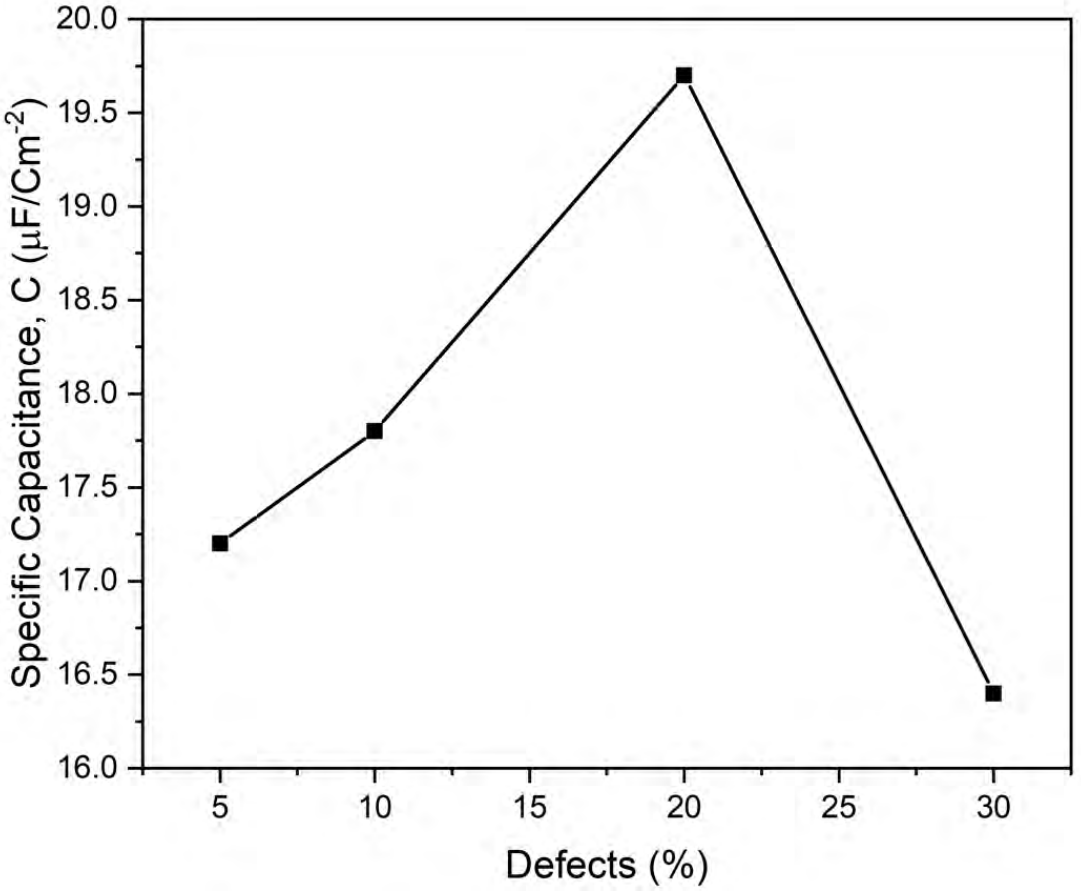

Fig 3. 21: Variation of Specific Capacitance with defects levels. Highest specific capacitance can be seen at 20% defects.

Depicts from Fig 3.21 and Table 3.2, 20% defects exhibit highest specific capacitance among all other models. It is (19.8 μF/cm^{-2}) almost 18% better than the validated crumpled model (16.351 μF/cm^{-2}) which can be announced the most optimized version of the EDLC model. Better charging ability, lower free energy, higher solvent accessible area ensures this enhanced performance of the model. In fact, almost in every case with defects, the specific capacitance is higher than the validated model (17.2 for 5% and 17.7 for 10%). Another reason behind this the total surface charge. Although the per atom charge was given same but higher defects means lower atoms, leading to lower surface charge. It can be concluded that surface charge for 30 % is too low to get a higher amount of capacitance.

3.5 Effect of Surface Wettability of Crumpled Graphene Electrode on the EDLC Performance

In this section, the effects of surface wettability on electrolyte electrosorption have been analyzed. An in-depth investigation into the interfacial EDL microstructures was conducted to determine the influences of wetting qualities on electrolyte electrosorption. Previous studies have demonstrated that surface wettability have considerable impact on the electrode-electrolyte interfacial microstructure. So, the influence of wettability on our model is explored with varied contact angles. To create, different wetting scenario, contact angles were varied and four contact angles were taken as, 29.4°, 65.4°, 95.3° and 141.3°

3.5.1 Density Profiles of the Electrolyte Ions for Different Surface Wettability

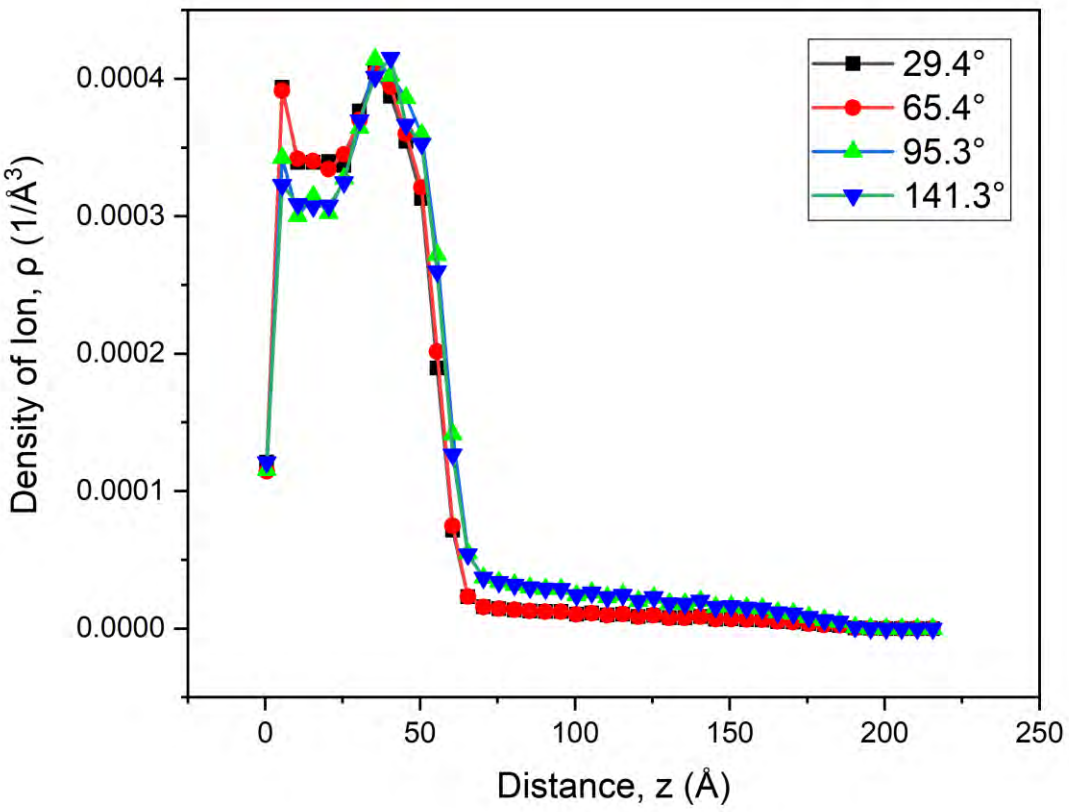

Fig 3. 22: Density profile of Cl^- for different contact angles.

The density profiles of electrolytes as a function of representative contact angle θ are shown in Fig. 3.22 and 3.23. In the EDL region of nanoscale thickness, distinct electrolyte layering is detected, which is a typical property of electrolyte electrosorption structure at the charged surface, and is in good accord with earlier MD studies [121]. Electrolyte agglomeration at the charged electrode is significantly affected by the wetting condition. The magnitude of Cl- density is increased to 29% as the wetting property of the surface is improved, and their layer architectures grew more evident shown in Fig 3.22 and Fig 3.23. This suggests that enhancing the wetting characteristic is likely to aid in the formation of the inner Helmholtz layer.

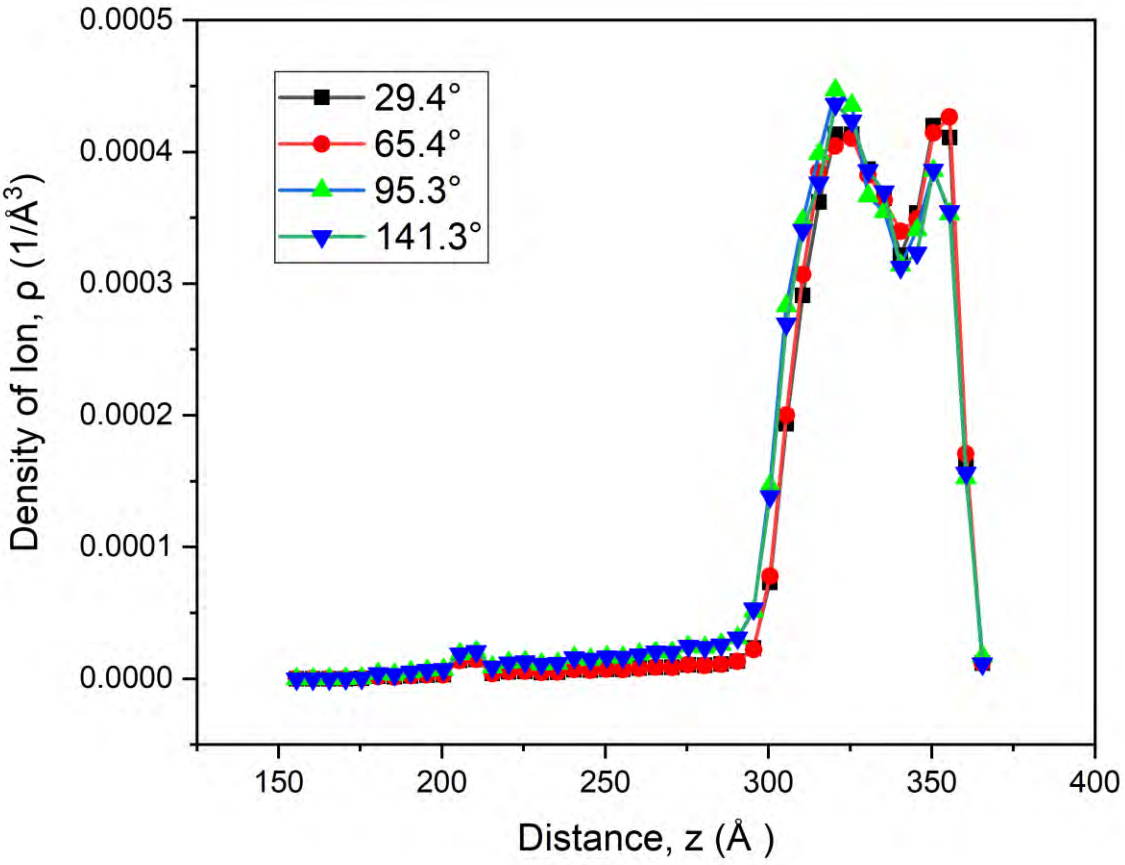

Fig 3. 23: Cations gathering up near cathode. Higher accumulation for hydrophilic surface.

3.5.2 Variation of Density Profiles of Water Molecules with Varied Contact Angles

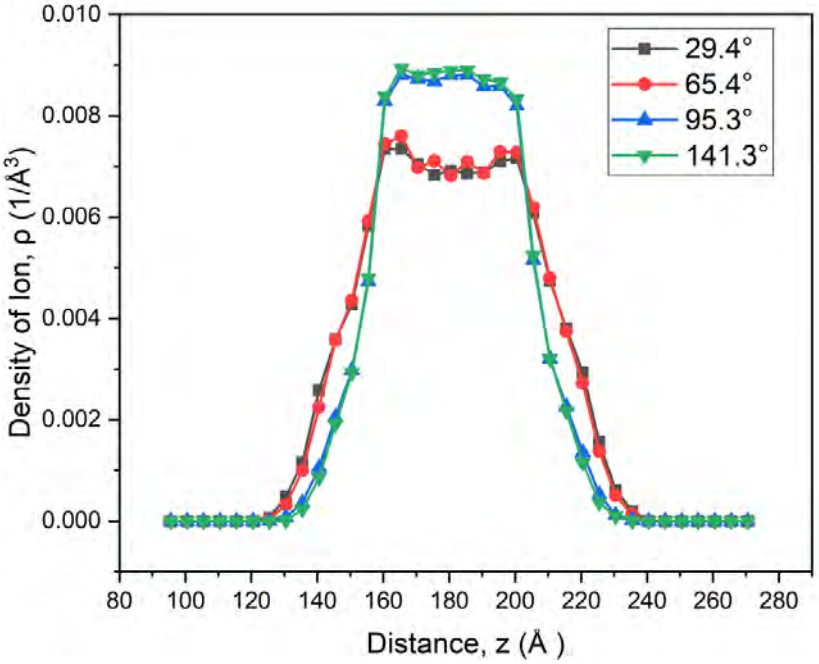

Fig 3. 24: Lower density peak of H molecules for hydrophilic surface.

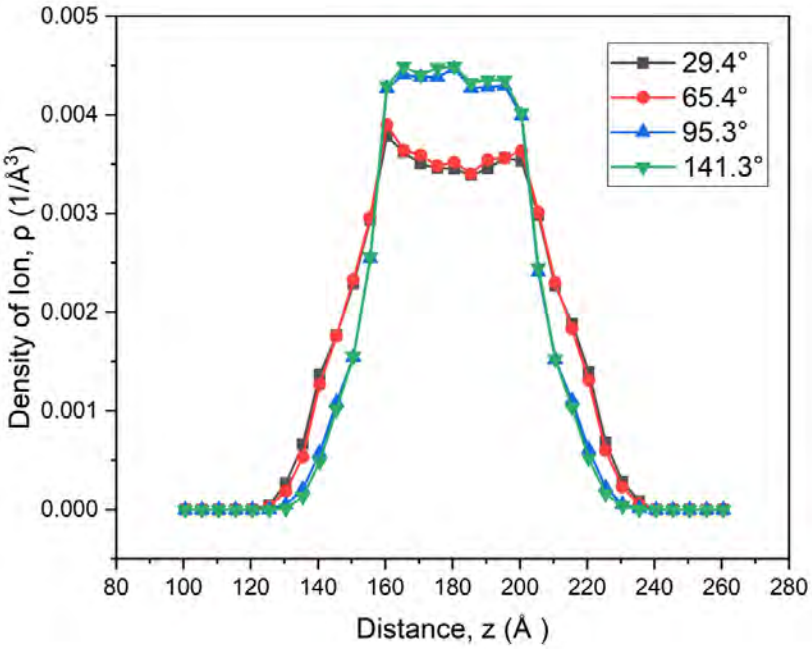

Fig 3. 25: Distribution of water-O solvent molecules as a function of contact angle.

A different case is seen for the water molecules. Unlike the ions, the value of the density peak for water molecules decreased with the increased contact angle represented at Fig 3.24 and 3.25. The reason behind this is some water molecules near the electrode surface could manage to enter into and the water molecules were spread onto the electrode surface the electrode due to its hydrophilic nature. This may be responsible for a lower density peak for water molecules eventually enhancing the performance of the supercapacitor.

3.5.3 Impact of Surface Wettability on EDLC Performance

Various EDLC performance parameters are calculated for different surface wettability and explained in the section below:

The free energy for counter-ions from the bulk region to the absorbed layer was computed to characterize the energy barriers for electrolyte electrosorption [122]. It should be highlighted that maxima in the free energy profiles indicate strong barriers to ion electrosorption on the charged surface, whereas minima correspond to the most favourable place for stack [117]. In accordance with the greater ion populations on the hydrophilic surface, the magnitude of free energy barriers decreased monotonically with increasing displayed at Fig. 3.26. The minima of energy for 29.4° shows a value of 14.5 Kj/mol which is lower than the minima of even the most optimized structure (defects =20% and r=68.4Å) mentioned in the 3.4.2 section. This was primarily due to the enhanced electrode-electrolyte interactions. The energy penalty for electrosorption near the hydrophobic surface is larger than the hydrophilic surface. In other words, the activation energy calculated for hydrophobic surfaces is a bit higher than that calculated for hydrophilic surfaces. This is the reason why water molecules could enter into the nearest electrodes.

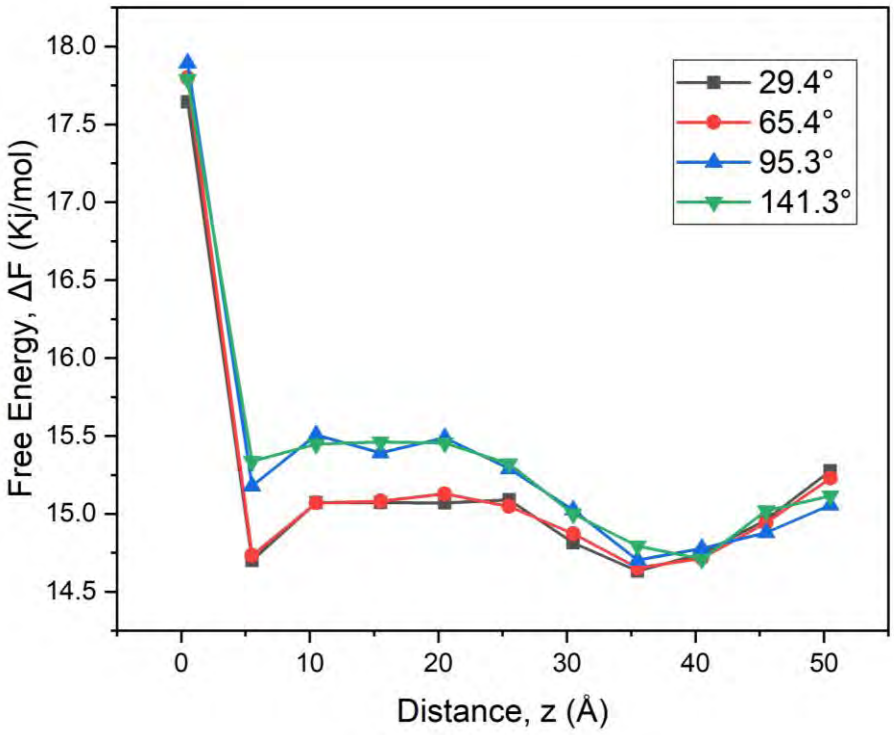

Fig 3. 26: Distribution of free energy with different surface wettability situations.

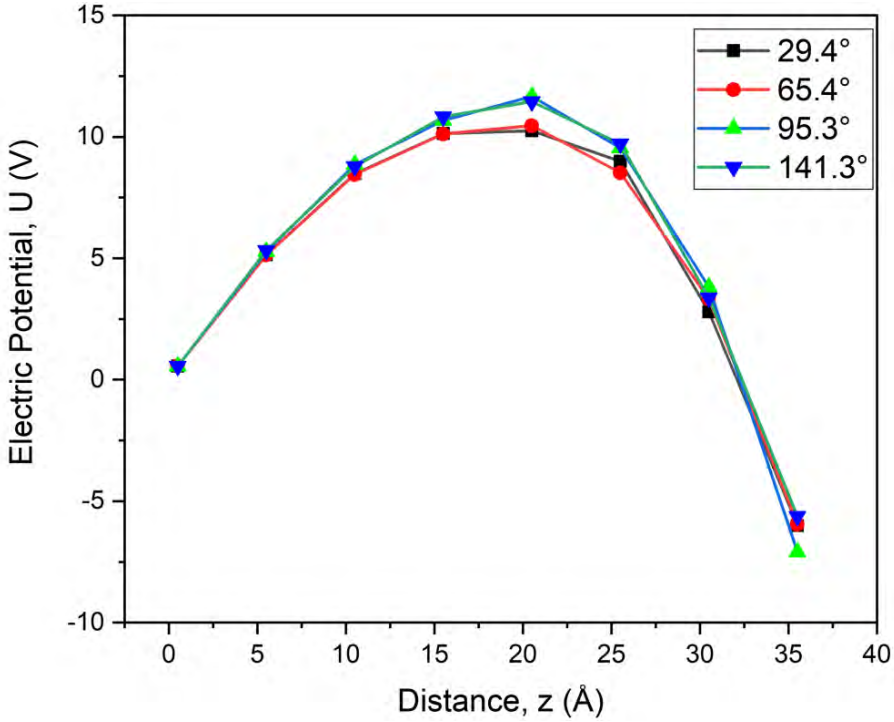

Fig 3. 27: Total potential distribution at different contact angles.

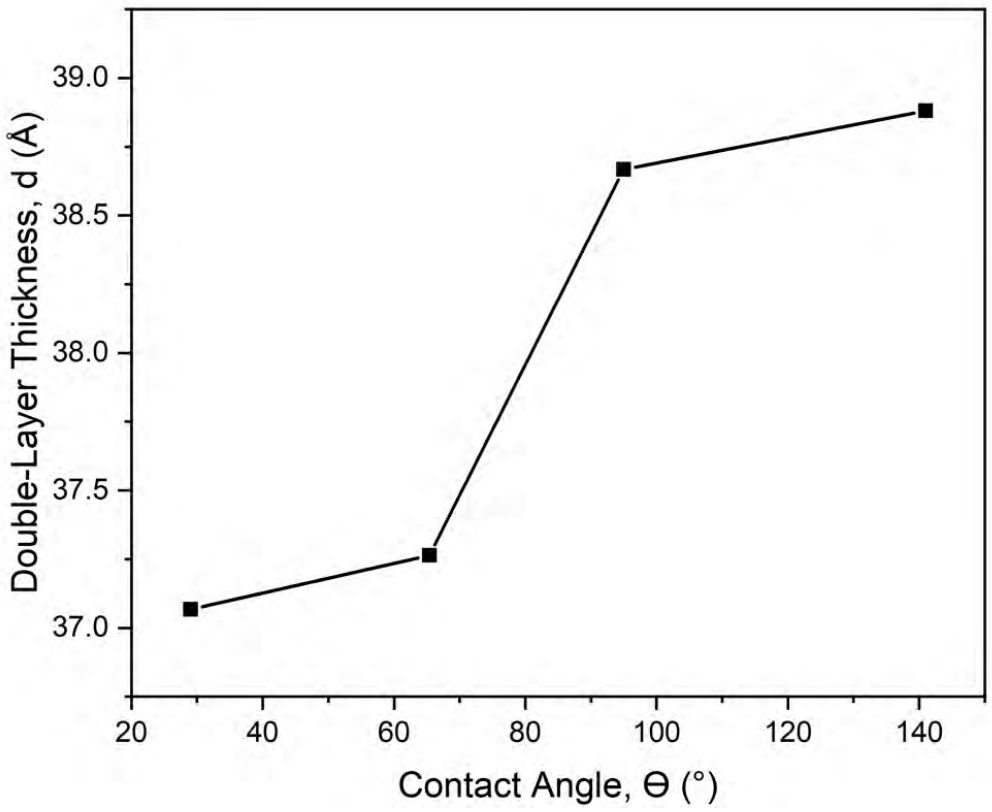

Fig 3. 28: Variation of EDL thickness with changed contact angles.

In the Fig 3.27 total potential profile is shown. From that figure it is quite evident that with the increased contact angle, the potential tends to be reduced as better wettability ensures better screening ability of the ions as well as $U_{solvent}$ part becomes lower. As the density of water molecules are lower for hydrophilic structure, potential from solvent becomes less as well. However, potential from ions incorporate greater potential drop which in turn cumulatively makes the overall potential get lowered.

The effective EDL thickness near crumpled graphene electrodes with varying wetting qualities is investigated to further quantify the interfacial microstructures. As shown in the Fig 3.28, The EDL thickness d of electrolyte ions increased around 5.5% with the deterioration in wetting property, which is consistent with the energy barrier distribution. This is due to the stronger interaction parameters which ensures thinner double layer. This result indicate that near hydrophilic electrodes charge gathers in a more compact way making thinner EDL layer than hydrophobic electrodes.

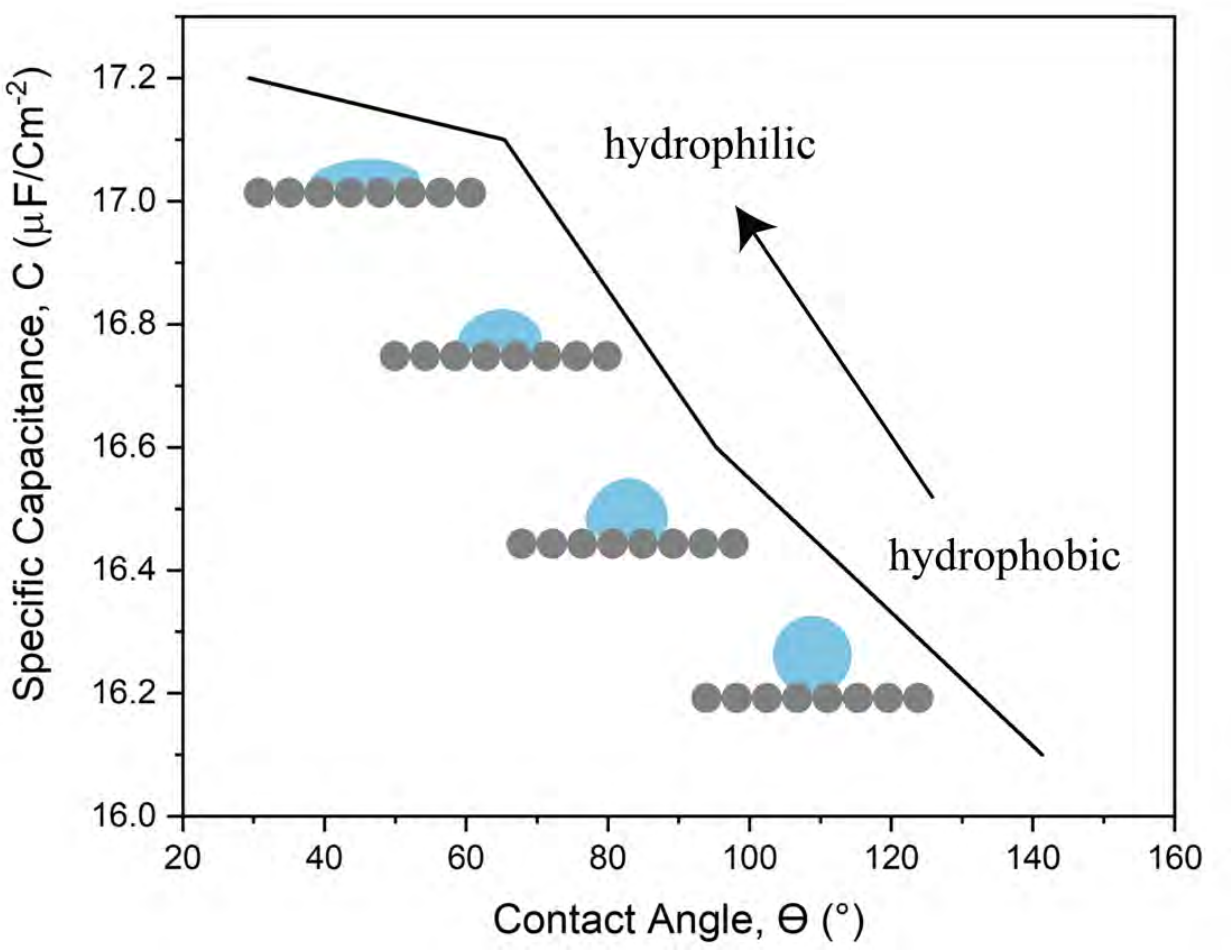

Fig 3. 29: Increased capacitance shown from hydrophobic surface to Hydrophilic surface.

In the Fig 3.23 above displays the change of the capacitive behavior of crumpled graphene electrodes with different wetting condition. The figure clearly presents that as the contact angle is increased specific capacitance of the supercapacitor decreased which is very much understandable comparing with other performance parameters.

When the contact angle is 141.3° the supercapacitor possesses about 16.2 μF/cm^{-2} specific capacitance whereas improved wetting property consequently enhance its capacitive performance to 17.2 μF/cm^{-2} which is roughly 7% more. This is because when the electrode surface is hydrophilic, it is wetted more by the electrolyte and solvent molecules which is exactly portrayed in the density profiles. Solvent accessible area thus increased significantly and hence the capacitance is boosted.

Below a brief summary of the EDLC performance with varied contact angles is given by Table 3.3:

Table 3. 3 Various performance parameters summarized for different surface wettability.

Contact Angle (°)	**d (Å)**	**C (μF/cm^{-2})**	**C (% increase with respect to the superhydrophobic surface))**
29.4	37	17.2	7
65.4	37.2	17.08	6.08
95.3	38.8	16.5	2.4
141.3	39	16.2	--

Chapter 4

Conclusions and Recommendations

4.1 Conclusion

An extensive investigation of crumpled graphene electrodes in supercapacitors has been conducted in this thesis by employing molecular dynamics simulation. The computations were performed in LAMMPS and post processing were done in MATLAB and OVITO. The main objective of the study is to explore how crumpled graphene behaves as electrodes and by doing this further upgraded model is discovered. The major findings from the current investigation are summarized below:

i. The modeled EDLC with crumpled graphene electrode exhibited better charging ability than planar graphen electrodes because of the enhanced solvent accessible area and entrance of ions inside the elctrodes. Improved electrode-electrolyte interaction in the modelled EDLC ensures compact packing of ions and thus thin electric double layer is formed.

ii. The crumpled graphene electrode model showed specific capacitance of 16.351 $\mu F/cm^{-2}$, five times higher than the planar graphene electrode model.

iii. The effect of the degree of crumpling of graphene on the supercapacitor performance was observed. Of all the crumpling states examined, the basic crumpled model (fully crumple state) with a radius of 68.3Å was found to possess the best performance. It is observed that due to the 3-D architecture, which makes the surface area of crumpled graphene more attainable, decreasing the crumple radius enhanced the supercapacitor performance.

iv. The developed model was optimized further by incorporating defects on the surface (5%, 10%, 20%, 30%). The addition of 5% defect on the crumpled graphene surface improved the charging phenomenon. Because of the minimization of activation energy, more charge accumulation was noticed and a thinner double layer was developed. This scenario beccame better by increasing the defect up to 20%, which possessed a very high specific capacitance of 19.8 $\mu F/cm^{-2}$.

v. However, the increase of vacancy to 30% exhibited detrimental effect on the performance. Lower contact area of the electrode possesing larger pores/defects than necessary for losing hydration shell, and lower partition co-efficient are determined to be the prime reasons behind this inferior performance.

vi. Influence of surface wettability on the developed EDLC performance was examined and it was found that hydrophilic surface ensures better by enhancing the accessible area for electrolytes. Energy barriers were minimised as the surface moved from hydrophilic to hydrophobic. Hydrophobic surface hinders ions to penetrate into electrode which in turn creates thicker double layer. The best performance was obtained for a contact angle of 29.4° having a specific capacitance value of 17.2 $\mu F/cm^{-2}$.

4.2 Recommendation

The following suggestions can be made for further research into the atomistic structure of EDLC in a more thorough manner:

i. The simulations of the present study are carried out using constant charge method where a constant charge is incorporated in the electrode surface. However, constant potential method could provide more reasonable result showing more accurate ion-ion and ion-electrode interaction. Because of the limitations of the simulation facility used for the present study, we could not emply the constant potential method.

ii. All the supercapacitor model was designed for aqueous electrolyte. Using organic electrolyte or ionic liquids in place of aqueous electrolyte can be an approach to increase the energy density of the EDLC model. Because of their high working voltage and ionization potential, ionic electrolytes, also known as Room Temperature Ionic Liquids (RTILs), offer a lot of potential in this field. Organic electrolytes have also showed promise in this area, as they can resist higher voltages, be employed with a variety of electrolyte combinations, and provide larger capacitance values.

iii. Decorating Crumpled Graphene (CG) with various functional nanostructures such as metals (Pt, Ag), metal oxides (SnO_2, Mn_3O_4), and transition metal Phosphides has the potential to improve its performance. This aspect can be examined further.

References

[1] P. Simon and Y. Gogotsi, “Materials for electrochemical capacitors,” in *Nanoscience and Technology*, Co-Published with Macmillan Publishers Ltd, UK, 2009, pp. 320–329. doi: 10.1142/9789814287005_0033.

[2] L. Oakes *et al.*, “Surface engineered porous silicon for stable, high performance electrochemical supercapacitors,” *Sci Rep*, vol. 3, no. 1, Art. no. 1, Oct. 2013, doi: 10.1038/srep03020.

[3] W. Raza *et al.*, “Recent advancements in supercapacitor technology,” *Nano Energy*, vol. 52, pp. 441–473, Oct. 2018, doi: 10.1016/j.nanoen.2018.08.013.

[4] J. Xie and M. Wang, “High surface area nano-structured graphene composites and capacitive devices incorporating the same,” US9656862B2, May 23, 2017 Accessed: Jun. 07, 2022. [Online]. Available: https://patents.google.com/patent/US9656862B2/en

[5] S. R. C. Vivekchand, C. S. Rout, K. S. Subrahmanyam, A. Govindaraj, and C. N. R. Rao, “Graphene-based electrochemical supercapacitors,” *J Chem Sci*, vol. 120, no. 1, pp. 9–13, Jan. 2008, doi: 10.1007/s12039-008-0002-7.

[6] Y. A. Tarek, R. Shakil, A. H. Reaz, C. K. Roy, H. R. Barai, and S. H. Firoz, “Wrinkled Flower-Like rGO intercalated with Ni(OH) $_2$ and MnO $_2$ as High-Performing Supercapacitor Electrode,” *ACS Omega*, vol. 7, no. 23, pp. 20145–20154, Jun. 2022, doi: 10.1021/acsomega.2c01986.

[7] S. Mao, Z. Wen, H. Kim, G. Lu, P. Hurley, and J. Chen, “A General Approach to One-Pot Fabrication of Crumpled Graphene-Based Nanohybrids for Energy Applications,” *ACS Nano*, vol. 6, no. 8, pp. 7505–7513, Aug. 2012, doi: 10.1021/nn302818j.

[8] A. S. Shaplov, R. Marcilla, and D. Mecerreyes, “Recent Advances in Innovative Polymer Electrolytes based on Poly(ionic liquid)s,” *Electrochimica Acta*, vol. 175, pp. 18–34, Sep. 2015, doi: 10.1016/j.electacta.2015.03.038.

[9] S. Seki *et al.*, “Effects of cation and anion on physical properties of room-temperature ionic liquids,” *Journal of Molecular Liquids*, vol. 152, no. 1, pp. 9–13, Mar. 2010, doi: 10.1016/j.molliq.2009.10.008.

[10] M. Endo, T. Takeda, Y. J. Kim, K. Koshiba, and K. Ishii, “High Power Electric Double Layer Capacitor (EDLC’s); from Operating Principle to Pore Size Control in Advanced Activated Carbons,” *Carbon letters*, vol. 1, no. 3_4, pp. 117–128, 2001.

[11] V. S. Bagotsky, *Fundamentals of Electrochemistry*. John Wiley & Sons, 2005.

[12] P. Sharma and T. S. Bhatti, “A review on electrochemical double-layer capacitors,” *Energy Conversion and Management*, vol. 51, no. 12, pp. 2901–2912, Dec. 2010, doi: 10.1016/j.enconman.2010.06.031.

[13] H. Pan, J. Li, and Y. Feng, “Carbon Nanotubes for Supercapacitor,” *Nanoscale Res Lett*, vol. 5, no. 3, Art. no. 3, Mar. 2010, doi: 10.1007/s11671-009-9508-2.

[14] J. Huang, B. G. Sumpter, and V. Meunier, “Theoretical Model for Nanoporous Carbon Supercapacitors,” *Angewandte Chemie*, vol. 120, no. 3, pp. 530–534, 2008, doi: 10.1002/ange.200703864.

[15] L. L. Zhang and X. S. Zhao, “Carbon-based materials as supercapacitor electrodes,” *Chem. Soc. Rev.*, vol. 38, no. 9, pp. 2520–2531, Aug. 2009, doi: 10.1039/B813846J.

[16] G. A. Tiruye, “Application of ionic liquids, innovative polymer electrolytes and novel carbonaceous materials in supercapacitors,” p. 270, 2016.

[17] C. Wolff, S. Jeong, E. Paillard, A. Balducci, and S. Passerini, “High power, solvent-free electrochemical double layer capacitors based on pyrrolidinium dicyanamide ionic liquids,” *Journal of Power Sources*, vol. 293, pp. 65–70, Oct. 2015, doi: 10.1016/j.jpowsour.2015.05.065.

[18] “Distinct Difference in Ionic Transport Behavior in Polymer Electrolytes Depending on the Matrix Polymers and Incorporated Salts | The Journal of Physical Chemistry B.” https://pubs.acs.org/doi/abs/10.1021/jp045328j (accessed Jun. 07, 2022).

[19] E. S. Steigerwalt, G. A. Deluga, D. E. Cliffel, and C. M. Lukehart, “A Pt−Ru/Graphitic Carbon Nanofiber Nanocomposite Exhibiting High Relative Performance as a Direct-Methanol

Fuel Cell Anode Catalyst," *J. Phys. Chem. B*, vol. 105, no. 34, pp. 8097–8101, Aug. 2001, doi: 10.1021/jp011633i.

[20] S. Seki, Md. A. B. H. Susan, T. Kaneko, H. Tokuda, A. Noda, and M. Watanabe, "Distinct Difference in Ionic Transport Behavior in Polymer Electrolytes Depending on the Matrix Polymers and Incorporated Salts," *J. Phys. Chem. B*, vol. 109, no. 9, pp. 3886–3892, Mar. 2005, doi: 10.1021/jp045328j.

[21] A. Burke, Z. Liu, and H. Zhao, "Present and future applications of supercapacitors in electric and hybrid vehicles," in *2014 IEEE International Electric Vehicle Conference (IEVC)*, Dec. 2014, pp. 1–8. doi: 10.1109/IEVC.2014.7056094.

[22] J. R. Miller and A. Burke, "Electrochemical Capacitors: Challenges and Opportunities for Real-World Applications," *Electrochem. Soc. Interface*, vol. 17, no. 1, p. 53, Mar. 2008, doi: 10.1149/2.F08081IF.

[23] H. Chen, T. N. Cong, W. Yang, C. Tan, Y. Li, and Y. Ding, "Progress in electrical energy storage system: A critical review," *Progress in Natural Science*, vol. 19, no. 3, pp. 291–312, Mar. 2009, doi: 10.1016/j.pnsc.2008.07.014.

[24] J. Chmiola, G. Yushin, Y. Gogotsi, C. Portet, P. Simon, and P. L. Taberna, "Anomalous Increase in Carbon Capacitance at Pore Sizes Less Than 1 Nanometer," *Science*, vol. 313, no. 5794, pp. 1760–1763, Sep. 2006, doi: 10.1126/science.1132195.

[25] S. Y. Lee, C. H. Choi, M. W. Chung, J. H. Chung, and S. I. Woo, "Dimensional tailoring of nitrogen-doped graphene for high performance supercapacitors," *RSC Adv.*, vol. 6, no. 60, pp. 55577–55583, Jun. 2016, doi: 10.1039/C6RA07825G.

[26] Y. Zhang *et al.*, "Progress of electrochemical capacitor electrode materials: A review," *International Journal of Hydrogen Energy*, vol. 34, no. 11, pp. 4889–4899, Jun. 2009, doi: 10.1016/j.ijhydene.2009.04.005.

[27] G. Wang, L. Zhang, and J. Zhang, "A review of electrode materials for electrochemical supercapacitors," *Chem. Soc. Rev.*, vol. 41, no. 2, pp. 797–828, Jan. 2012, doi: 10.1039/C1CS15060J.

[28] N. N. Rajput, J. Monk, and F. R. Hung, “Ionic Liquids Confined in a Realistic Activated Carbon Model: A Molecular Simulation Study,” *J. Phys. Chem. C*, vol. 118, no. 3, pp. 1540–1553, Jan. 2014, doi: 10.1021/jp408617j.

[29] P. Simon and A. Burke, “Nanostructured Carbons: Double-Layer Capacitance and More,” *Electrochem. Soc. Interface*, vol. 17, no. 1, pp. 38–43, Mar. 2008, doi: 10.1149/2.F05081IF.

[30] J. Jiang *et al.*, “Highly ordered macroporous woody biochar with ultra-high carbon content as supercapacitor electrodes,” *Electrochimica Acta*, vol. 113, pp. 481–489, Dec. 2013, doi: 10.1016/j.electacta.2013.09.121.

[31] Z. G. Cambaz, G. N. Yushin, Y. Gogotsi, K. L. Vyshnyakova, and L. N. Pereselentseva, “Formation of Carbide-Derived Carbon on beta-Silicon Carbide Whiskers,” *J American Ceramic Society*, vol. 89, no. 2, pp. 509–514, Feb. 2006, doi: 10.1111/j.1551-2916.2005.00780.x.

[32] C. Merlet *et al.*, “On the molecular origin of supercapacitance in nanoporous carbon electrodes,” *Nature Mater*, vol. 11, no. 4, Art. no. 4, Apr. 2012, doi: 10.1038/nmat3260.

[33] C. Merlet *et al.*, “Highly confined ions store charge more efficiently in supercapacitors,” *Nat Commun*, vol. 4, no. 1, p. 2701, Dec. 2013, doi: 10.1038/ncomms3701.

[34] Z. Yang *et al.*, “Aligned Carbon Nanotube Sheets for the Electrodes of Organic Solar Cells,” *Advanced Materials*, vol. 23, no. 45, pp. 5436–5439, 2011, doi: 10.1002/adma.201103509.

[35] A. P. Graham *et al.*, “How do carbon nanotubes fit into the semiconductor roadmap?,” *Appl. Phys. A*, vol. 80, no. 6, pp. 1141–1151, Mar. 2005, doi: 10.1007/s00339-004-3151-7.

[36] Z. Yang *et al.*, “Penetrated and aligned carbon nanotubes for counter electrodes of highly efficient dye-sensitized solar cells,” *Chemical Physics Letters*, vol. 549, pp. 82–85, Oct. 2012, doi: 10.1016/j.cplett.2012.08.055.

[37] K. S. Novoselov *et al.*, “Electric Field Effect in Atomically Thin Carbon Films,” *Science*, vol. 306, no. 5696, pp. 666–669, Oct. 2004, doi: 10.1126/science.1102896.

[38] A. A. Balandin, “Thermal Properties of Graphene, Carbon Nanotubes and Nanostructured Carbon Materials,” p. 37, 2011.

[39] L. Dai, "Functionalization of Graphene for Efficient Energy Conversion and Storage," *Acc. Chem. Res.*, vol. 46, no. 1, pp. 31–42, Jan. 2013, doi: 10.1021/ar300122m.

[40] Z. Yang *et al.*, "Recent Advancement of Nanostructured Carbon for Energy Applications," *Chem. Rev.*, vol. 115, no. 11, pp. 5159–5223, Jun. 2015, doi: 10.1021/cr5006217.

[41] X. Bai *et al.*, "In situ polymerization and characterization of grafted poly (3,4-ethylenedioxythiophene)/multiwalled carbon nanotubes composite with high electrochemical performances," *Electrochimica Acta*, vol. 87, pp. 394–400, Jan. 2013, doi: 10.1016/j.electacta.2012.09.079.

[42] M. Yang, B. Cheng, H. Song, and X. Chen, "Preparation and electrochemical performance of polyaniline-based carbon nanotubes as electrode material for supercapacitor," *Electrochimica Acta*, vol. 55, no. 23, pp. 7021–7027, Sep. 2010, doi: 10.1016/j.electacta.2010.06.077.

[43] H. Pan, C. K. Poh, Y. P. Feng, and J. Lin, "Supercapacitor Electrodes from Tubes-in-Tube Carbon Nanostructures," *Chem. Mater.*, vol. 19, no. 25, pp. 6120–6125, Dec. 2007, doi: 10.1021/cm071527e.

[44] G. Feng, S. Li, J. S. Atchison, V. Presser, and P. T. Cummings, "Molecular Insights into Carbon Nanotube Supercapacitors: Capacitance Independent of Voltage and Temperature," *J. Phys. Chem. C*, vol. 117, no. 18, pp. 9178–9186, May 2013, doi: 10.1021/jp403547k.

[45] Y. Shim and H. J. Kim, "Nanoporous Carbon Supercapacitors in an Ionic Liquid: A Computer Simulation Study," *ACS Nano*, vol. 4, no. 4, pp. 2345–2355, Apr. 2010, doi: 10.1021/nn901916m.

[46] O. N. Kalugin, V. V. Chaban, V. V. Loskutov, and O. V. Prezhdo, "Uniform Diffusion of Acetonitrile inside Carbon Nanotubes Favors Supercapacitor Performance," *Nano Lett.*, vol. 8, no. 8, pp. 2126–2130, Aug. 2008, doi: 10.1021/nl072976g.

[47] R. J. Mashl, S. Joseph, N. R. Aluru, and E. Jakobsson, "Anomalously Immobilized Water: A New Water Phase Induced by Confinement in Nanotubes," *Nano Lett.*, vol. 3, no. 5, pp. 589–592, May 2003, doi: 10.1021/nl0340226.

[48] C. Xiong *et al.*, "Reduced graphene oxide-carbon nanotube grown on carbon fiber as binder-free electrode for flexible high-performance fiber supercapacitors," *Composites Part B: Engineering*, vol. 116, pp. 7–15, May 2017, doi: 10.1016/j.compositesb.2017.02.028.

[49] G. Feng, D. Jiang, and P. T. Cummings, "Curvature Effect on the Capacitance of Electric Double Layers at Ionic Liquid/Onion-Like Carbon Interfaces," *J. Chem. Theory Comput.*, vol. 8, no. 3, pp. 1058–1063, Mar. 2012, doi: 10.1021/ct200914j.

[50] Y. Gao, "Graphene and Polymer Composites for Supercapacitor Applications: a Review," *Nanoscale Research Letters*, vol. 12, no. 1, p. 387, Jun. 2017, doi: 10.1186/s11671-017-2150-5.

[51] M. Depardieu *et al.*, "Carbonaceous multiscale-cellular foams as novel electrodes for stable, efficient lithium–sulfur batteries," *RSC Adv.*, vol. 4, no. 46, pp. 23971–23976, Jun. 2014, doi: 10.1039/C4RA03110E.

[52] K. Zhang, L. L. Zhang, X. S. Zhao, and J. Wu, "Graphene/Polyaniline Nanofiber Composites as Supercapacitor Electrodes," *Chem. Mater.*, vol. 22, no. 4, pp. 1392–1401, Feb. 2010, doi: 10.1021/cm902876u.

[53] M. D. Stoller, S. Park, Y. Zhu, J. An, and R. S. Ruoff, "Graphene-Based Ultracapacitors," *Nano Lett.*, vol. 8, no. 10, pp. 3498–3502, Oct. 2008, doi: 10.1021/nl802558y.

[54] J. Vatamanu, L. Cao, O. Borodin, D. Bedrov, and G. D. Smith, "On the Influence of Surface Topography on the Electric Double Layer Structure and Differential Capacitance of Graphite/Ionic Liquid Interfaces," *J. Phys. Chem. Lett.*, vol. 2, no. 17, pp. 2267–2272, Sep. 2011, doi: 10.1021/jz200879a.

[55] L. Xing, J. Vatamanu, G. D. Smith, and D. Bedrov, "Nanopatterning of Electrode Surfaces as a Potential Route to Improve the Energy Density of Electric Double-Layer Capacitors: Insight from Molecular Simulations," *J. Phys. Chem. Lett.*, vol. 3, no. 9, pp. 1124–1129, May 2012, doi: 10.1021/jz300253p.

[56] J. Vatamanu, O. Borodin, D. Bedrov, and G. D. Smith, "Molecular Dynamics Simulation Study of the Interfacial Structure and Differential Capacitance of Alkylimidazolium Bis(trifluoromethanesulfonyl)imide [Cnmim][TFSI] Ionic Liquids at Graphite Electrodes," *J. Phys. Chem. C*, vol. 116, no. 14, pp. 7940–7951, Apr. 2012, doi: 10.1021/jp301399b.

[57] J. Vatamanu, L. Xing, W. Li, and D. Bedrov, “Influence of temperature on the capacitance of ionic liquid electrolytes on charged surfaces,” *Phys. Chem. Chem. Phys.*, vol. 16, no. 11, pp. 5174–5182, Feb. 2014, doi: 10.1039/C3CP54705A.

[58] H. M. Jeong *et al.*, “Nitrogen-Doped Graphene for High-Performance Ultracapacitors and the Importance of Nitrogen-Doped Sites at Basal Planes,” *Nano Lett.*, vol. 11, no. 6, pp. 2472–2477, Jun. 2011, doi: 10.1021/nl2009058.

[59] E. Paek, A. J. Pak, K. E. Kweon, and G. S. Hwang, “On the Origin of the Enhanced Supercapacitor Performance of Nitrogen-Doped Graphene,” *J. Phys. Chem. C*, vol. 117, no. 11, pp. 5610–5616, Mar. 2013, doi: 10.1021/jp312490q.

[60] S. Kerisit, B. Schwenzer, and M. Vijayakumar, “Effects of Oxygen-Containing Functional Groups on Supercapacitor Performance,” *J. Phys. Chem. Lett.*, vol. 5, no. 13, pp. 2330–2334, Jul. 2014, doi: 10.1021/jz500900t.

[61] K. Xu, X. Ji, C. Chen, H. Wan, L. Miao, and J. Jiang, “Electrochemical double layer near polar reduced graphene oxide electrode: Insights from molecular dynamic study,” *Electrochimica Acta*, vol. 166, pp. 142–149, Jun. 2015, doi: 10.1016/j.electacta.2015.03.101.

[62] S. Kondrat, P. Wu, R. Qiao, and A. A. Kornyshev, “Accelerating charging dynamics in subnanometre pores,” *Nature Mater*, vol. 13, no. 4, pp. 387–393, Apr. 2014, doi: 10.1038/nmat3916.

[63] N. N. Rajput, J. Monk, R. Singh, and F. R. Hung, “On the Influence of Pore Size and Pore Loading on Structural and Dynamical Heterogeneities of an Ionic Liquid Confined in a Slit Nanopore,” *J. Phys. Chem. C*, vol. 116, no. 8, pp. 5169–5181, Mar. 2012, doi: 10.1021/jp212440f.

[64] S. Salemi, H. Akbarzadeh, and S. Abdollahzadeh, “Nano-confined ionic liquid [emim][PF6] between graphite sheets: A molecular dynamics study,” *Journal of Molecular Liquids*, vol. 215, pp. 512–519, Mar. 2016, doi: 10.1016/j.molliq.2016.01.035.

[65] H. Yang *et al.*, “Molecular Origin of Electric Double-Layer Capacitance at Multilayer Graphene Edges,” *J. Phys. Chem. Lett.*, vol. 8, no. 1, pp. 153–160, Jan. 2017, doi: 10.1021/acs.jpclett.6b02659.

[66] W. Yuan *et al.*, “The edge- and basal-plane-specific electrochemistry of a single-layer graphene sheet,” *Sci Rep*, vol. 3, no. 1, Art. no. 1, Jul. 2013, doi: 10.1038/srep02248.

[67] A. J. Pak, E. Paek, and G. S. Hwang, “Impact of Graphene Edges on Enhancing the Performance of Electrochemical Double Layer Capacitors,” *J. Phys. Chem. C*, vol. 118, no. 38, pp. 21770–21777, Sep. 2014, doi: 10.1021/jp504458z.

[68] A. Yu, A. Sy, and A. Davies, “Graphene nanoplatelets supported MnO2 nanoparticles for electrochemical supercapacitor,” *Synthetic Metals*, vol. 161, no. 17–18, pp. 2049–2054, Sep. 2011, doi: 10.1016/j.synthmet.2011.04.034.

[69] J. Yan, Z. Fan, T. Wei, W. Qian, M. Zhang, and F. Wei, “Fast and reversible surface redox reaction of graphene–MnO2 composites as supercapacitor electrodes,” *Carbon*, vol. 48, no. 13, pp. 3825–3833, Nov. 2010, doi: 10.1016/j.carbon.2010.06.047.

[70] J. S. Ross *et al.*, “Electrical control of neutral and charged excitons in a monolayer semiconductor,” *Nat Commun*, vol. 4, no. 1, Art. no. 1, Feb. 2013, doi: 10.1038/ncomms2498.

[71] W. K. Si-zhe, Z. Xue-jiao, and W. U. Hai-xia*, “Graphene Quantum Dots Enhanced Electrochemical Performance of Polypyrrole as Supercapacitor Electrode,” *Journal of Electrochemistry*, vol. 19, no. 4, p. 361, Aug. 2013.

[72] M. Harb, “Fabrication of Supercapacitor Based on Graphene and Polyaniline for Energy Storage Applications,” *International Journal of Advanced Research in Electrical, Electronics and Instrumentation Engineering*, vol. 4, Oct. 2015, doi: 10.15662/IJAREEIE.2015.0410033.

[73] A. Khosrozadeh, M. A. Darabi, M. Xing, and Q. Wang, “Flexible Electrode Design: Fabrication of Freestanding Polyaniline-Based Composite Films for High-Performance Supercapacitors,” *ACS Appl. Mater. Interfaces*, vol. 8, no. 18, pp. 11379–11389, May 2016, doi: 10.1021/acsami.5b11256.

[74] R. B. Rakhi, W. Chen, D. Cha, and H. N. Alshareef, “High performance supercapacitors using metal oxide anchored graphene nanosheet electrodes,” *J. Mater. Chem.*, vol. 21, p. 16197, 2011, doi: 10.1039/c1jm12963e.

[75] C. Zheng, X. Zhou, H. Cao, G. Wang, and Z. Liu, “Synthesis of porous graphene/activated carbon composite with high packing density and large specific surface area for supercapacitor

electrode material," *Journal of Power Sources*, vol. 258, pp. 290–296, Jul. 2014, doi: 10.1016/j.jpowsour.2014.01.056.

[76] Q. Duan *et al.*, "pH-Responsive Supramolecular Vesicles Based on Water-Soluble Pillar[6]arene and Ferrocene Derivative for Drug Delivery," *J. Am. Chem. Soc.*, vol. 135, no. 28, pp. 10542–10549, Jul. 2013, doi: 10.1021/ja405014r.

[77] A. V. Ramya, A. N. Mohan, and B. Manoj, "Wrinkled graphene: synthesis and characterization of few layer graphene-like nanocarbons from kerosene," *Materials Science-Poland*, vol. 34, no. 2, pp. 330–336, Jun. 2016, doi: 10.1515/msp-2016-0061.

[78] V. C. Saha *et al.*, "Synthesis and Characterization of Reduced Graphene Oxide Reinforced Polymer Matrix Composite," *IOP Conf. Ser.: Mater. Sci. Eng.*, vol. 438, no. 1, p. 012008, Oct. 2018, doi: 10.1088/1757-899X/438/1/012008.

[79] J. Luo *et al.*, "Compression and Aggregation-Resistant Particles of Crumpled Soft Sheets," *ACS Nano*, vol. 5, no. 11, pp. 8943–8949, Nov. 2011, doi: 10.1021/nn203115u.

[80] Z. Tang, X. Li, T. Sun, S. Shen, X. Huixin, and J. Yang, "Porous crumpled graphene with hierarchical pore structure and high surface utilization efficiency for supercapacitor," *Microporous and Mesoporous Materials*, vol. 272, pp. 40–43, Dec. 2018, doi: 10.1016/j.micromeso.2018.06.020.

[81] J. M. Semat, W. Rashmi, V. Mahesh, M. Khalid, and J. Priyanka, "Synthesis of crumpled graphene by fast cooling method," *AIP Conference Proceedings*, vol. 2137, no. 1, p. 020014, Aug. 2019, doi: 10.1063/1.5120990.

[82] M. a. F. Gomes, "Fractal geometry in crumpled paper balls," *American Journal of Physics*, vol. 55, no. 7, pp. 649–650, Jul. 1987, doi: 10.1119/1.15094.

[83] J. Zang *et al.*, "Multifunctionality and control of the crumpling and unfolding of large-area graphene," *Nature Mater*, vol. 12, no. 4, pp. 321–325, Apr. 2013, doi: 10.1038/nmat3542.

[84] M. Becton, L. Zhang, and X. Wang, "Mechanics of graphyne crumpling," *Phys. Chem. Chem. Phys.*, vol. 16, no. 34, pp. 18233–18240, Aug. 2014, doi: 10.1039/C4CP02400A.

[85] Y. Wang *et al.*, "Preventing Graphene Sheets from Restacking for High-Capacitance Performance," *J. Phys. Chem. C*, vol. 115, no. 46, pp. 23192–23197, Nov. 2011, doi: 10.1021/jp206444e.

[86] J. Luo, H. D. Jang, and J. Huang, "Effect of Sheet Morphology on the Scalability of Graphene-Based Ultracapacitors," *ACS Nano*, vol. 7, no. 2, pp. 1464–1471, Feb. 2013, doi: 10.1021/nn3052378.

[87] HaroldL. Friedman, "Ionic hydration in chemistry and biophysics," *Journal of Electroanalytical Chemistry and Interfacial Electrochemistry*, vol. 131, pp. 407–408, Jan. 1982, doi: 10.1016/0022-0728(82)87097-6.

[88] J. J. Thomson, "XXXIII. On the charge of electricity carried by a gaseous ion," *The London, Edinburgh, and Dublin Philosophical Magazine and Journal of Science*, vol. 5, no. 27, pp. 346–355, Mar. 1903, doi: 10.1080/14786440309462931.

[89] B. E. Conway, H. Angerstein-Kozlowska, and W. B. A. Sharp, "Chemical Aspects of Specific Adsorption and Underpotential Electrodeposition in Relation to Charge Transfer," vol. 98, no. 1–6, pp. 61–74, Dec. 1975, doi: 10.1524/zpch.1975.98.1-6.061.

[90] D. van der Spoel, P. J. van Maaren, and H. J. C. Berendsen, "A systematic study of water models for molecular simulation: Derivation of water models optimized for use with a reaction field," *J. Chem. Phys.*, vol. 108, no. 24, pp. 10220–10230, Jun. 1998, doi: 10.1063/1.476482.

[91] Z. Hu, J. Vatamanu, O. Borodin, and D. Bedrov, "A molecular dynamics simulation study of the electric double layer and capacitance of [BMIM][PF6] and [BMIM][BF4] room temperature ionic liquids near charged surfaces," *Phys. Chem. Chem. Phys.*, vol. 15, no. 34, pp. 14234–14247, Aug. 2013, doi: 10.1039/C3CP51218E.

[92] X. Liu, Y. Wang, S. Li, and T. Yan, "Effects of anion on the electric double layer of imidazolium-based ionic liquids on graphite electrode by molecular dynamics simulation," *Electrochimica Acta*, vol. 184, pp. 164–170, Dec. 2015, doi: 10.1016/j.electacta.2015.10.064.

[93] J. Vatamanu, O. Borodin, and G. D. Smith, "Molecular Simulations of the Electric Double Layer Structure, Differential Capacitance, and Charging Kinetics for N-Methyl-N-

propylpyrrolidinium Bis(fluorosulfonyl)imide at Graphite Electrodes," *J. Phys. Chem. B*, vol. 115, no. 12, pp. 3073–3084, Mar. 2011, doi: 10.1021/jp2001207.

[94] D. Jiang and J. Wu, "Unusual effects of solvent polarity on capacitance for organic electrolytes in a nanoporous electrode," *Nanoscale*, vol. 6, no. 10, pp. 5545–5550, Apr. 2014, doi: 10.1039/C4NR00046C.

[95] R. Burt *et al.*, "Capacitance of Nanoporous Carbon-Based Supercapacitors Is a Trade-Off between the Concentration and the Separability of the Ions," *J. Phys. Chem. Lett.*, vol. 7, no. 19, pp. 4015–4021, Oct. 2016, doi: 10.1021/acs.jpclett.6b01787.

[96] Q.-Y. Zhang, P. Xie, X. Wang, X.-W. Yu, Z.-Q. Shi, and S.-H. Zhao, "Thermodynamic and transport properties of spiro-(1,1')-bipyrrolidinium tetrafluoroborate and acetonitrile mixtures: A molecular dynamics study*," *Chinese Phys. B*, vol. 25, no. 6, p. 066102, Apr. 2016, doi: 10.1088/1674-1056/25/6/066102.

[97] H. Yang *et al.*, "Kinetic-Dominated Charging Mechanism within Representative Aqueous Electrolyte-based Electric Double-Layer Capacitors," *J. Phys. Chem. Lett.*, vol. 8, no. 15, pp. 3703–3710, Aug. 2017, doi: 10.1021/acs.jpclett.7b01525.

[98] P. Wu, J. Huang, V. Meunier, B. G. Sumpter, and R. Qiao, "Voltage Dependent Charge Storage Modes and Capacity in Subnanometer Pores," *J. Phys. Chem. Lett.*, vol. 3, no. 13, pp. 1732–1737, Jul. 2012, doi: 10.1021/jz300506j.

[99] R. K. Kalluri, D. Konatham, and A. Striolo, "Aqueous NaCl Solutions within Charged Carbon-Slit Pores: Partition Coefficients and Density Distributions from Molecular Dynamics Simulations," *J. Phys. Chem. C*, vol. 115, no. 28, pp. 13786–13795, Jul. 2011, doi: 10.1021/jp203086x.

[100] M. C. F. Wander and K. L. Shuford, "Molecular Dynamics Study of Interfacial Confinement Effects of Aqueous NaCl Brines in Nanoporous Carbon," *J. Phys. Chem. C*, vol. 114, no. 48, pp. 20539–20546, Dec. 2010, doi: 10.1021/jp104972e.

[101] S. Plimpton, "Fast Parallel Algorithms for Short-Range Molecular Dynamics," *Journal of Computational Physics*, vol. 117, no. 1, pp. 1–19, Mar. 1995, doi: 10.1006/jcph.1995.1039.

[102] R. W. Pastor, B. R. Brooks, and A. Szabo, “An analysis of the accuracy of Langevin and molecular dynamics algorithms,” *Molecular Physics*, vol. 65, no. 6, pp. 1409–1419, Dec. 1988, doi: 10.1080/00268978800101881.

[103] L. Verlet, “Computer ‘Experiments’ on Classical Fluids. I. Thermodynamical Properties of Lennard-Jones Molecules,” *Phys. Rev.*, vol. 159, no. 1, pp. 98–103, Jul. 1967, doi: 10.1103/PhysRev.159.98.

[104] R. W. Hockney and J. W. Eastwood, *Computer Simulation Using Particles*. Boca Raton: CRC Press, 2021. doi: 10.1201/9780367806934.

[105] T. Darden, D. York, and L. Pedersen, “Particle mesh Ewald: An N·log(N) method for Ewald sums in large systems,” *J. Chem. Phys.*, vol. 98, no. 12, pp. 10089–10092, Jun. 1993, doi: 10.1063/1.464397.

[106] E. L. Pollock and J. Glosli, “Comments on PPPM, FMM, and the Ewald Method for Large Periodic Coulombic Systems,” *Computer Physics Communications*, vol. 95, no. 2–3, pp. 93–110, Jun. 1996, doi: 10.1016/0010-4655(96)00043-4.

[107] M. Galib, M. M. Hosen, J. K. Saha, Md. M. Islam, S. H. Firoz, and Md. A. Rahman, “Electrode surface modification of graphene-MnO2 supercapacitors using molecular dynamics simulations,” *J Mol Model*, vol. 26, no. 9, p. 251, Aug. 2020, doi: 10.1007/s00894-020-04483-5.

[108] J.-P. Hansen and I. R. McDonald, *Theory of Simple Liquids: with Applications to Soft Matter*. Academic Press, 2013.

[109] A. Lobkovsky, S. Gentges, H. Li, D. Morse, and T. A. Witten, “Scaling Properties of Stretching Ridges in a Crumpled Elastic Sheet,” *Science*, vol. 270, no. 5241, pp. 1482–1485, Dec. 1995, doi: 10.1126/science.270.5241.1482.

[110] S. J. Stuart, A. B. Tutein, and J. A. Harrison, “A reactive potential for hydrocarbons with intermolecular interactions,” *J. Chem. Phys.*, vol. 112, no. 14, pp. 6472–6486, Apr. 2000, doi: 10.1063/1.481208.

[111] “units command — LAMMPS documentation.” https://docs.lammps.org/units.html (accessed Jun. 07, 2022).

[112] H. Yang, Z. Bo, J. Yan, and K. Cen, “Influence of wettability on the electrolyte electrosorption within graphene-like nonconfined and confined space,” *International Journal of Heat and Mass Transfer*, vol. 133, pp. 416–425, Apr. 2019, doi: 10.1016/j.ijheatmasstransfer.2018.12.134.

[113] C. Lian, H. Liu, D. Henderson, and J. Wu, “Can ionophobic nanopores enhance the energy storage capacity of electric-double-layer capacitors containing nonaqueous electrolytes?,” *J. Phys.: Condens. Matter*, vol. 28, no. 41, p. 414005, Aug. 2016, doi: 10.1088/0953-8984/28/41/414005.

[114] T. Werder, J. H. Walther, R. L. Jaffe, T. Halicioglu, and P. Koumoutsakos, “On the Water−Carbon Interaction for Use in Molecular Dynamics Simulations of Graphite and Carbon Nanotubes,” *J. Phys. Chem. B*, vol. 107, no. 6, pp. 1345–1352, Feb. 2003, doi: 10.1021/jp0268112.

[115] G. Jiang, C. Cheng, D. Li, and J. Z. Liu, “Molecular dynamics simulations of the electric double layer capacitance of graphene electrodes in mono-valent aqueous electrolytes,” *Nano Res.*, vol. 9, no. 1, pp. 174–186, Jan. 2016, doi: 10.1007/s12274-015-0978-5.

[116] C. Merlet, C. Péan, B. Rotenberg, P. A. Madden, P. Simon, and M. Salanne, “Simulating Supercapacitors: Can We Model Electrodes As Constant Charge Surfaces?,” *J. Phys. Chem. Lett.*, vol. 4, no. 2, pp. 264–268, Jan. 2013, doi: 10.1021/jz3019226.

[117] M. V. Fedorov and R. M. Lynden-Bell, “Probing the neutral graphene–ionic liquid interface: insights from molecular dynamics simulations,” *Phys. Chem. Chem. Phys.*, vol. 14, no. 8, pp. 2552–2556, Feb. 2012, doi: 10.1039/C2CP22730D.

[118] D. C. Bell and A. J. Garratt-Reed, *Energy Dispersive X-ray Analysis in the Electron Microscope*. London: Garland Science, 2003. doi: 10.4324/9780203483428.

[119] P. Taboada-Serrano, S. Yiacoumi, and C. Tsouris, “Behavior of mixtures of symmetric and asymmetric electrolytes near discretely charged planar surfaces: A Monte Carlo study,” *The Journal of chemical physics*, vol. 123, p. 054703, Sep. 2005, doi: 10.1063/1.1992484.

[120] J. Chmiola, C. Largeot, P.-L. Taberna, P. Simon, and Y. Gogotsi, “Desolvation of Ions in Subnanometer Pores and Its Effect on Capacitance and Double-Layer Theory,” *Angew. Chem. Int. Ed.*, vol. 47, no. 18, pp. 3392–3395, Apr. 2008, doi: 10.1002/anie.200704894.

[121] Z. Bo, C. Li, H. Yang, K. Ostrikov, J. Yan, and K. Cen, “Design of Supercapacitor Electrodes Using Molecular Dynamics Simulations,” *Nano-Micro Lett.*, vol. 10, no. 2, p. 33, Apr. 2018, doi: 10.1007/s40820-018-0188-2.

[122] J. Vatamanu and O. Borodin, “Ramifications of Water-in-Salt Interfacial Structure at Charged Electrodes for Electrolyte Electrochemical Stability,” *J. Phys. Chem. Lett.*, vol. 8, no. 18, pp. 4362–4367, Sep. 2017, doi: 10.1021/acs.jpclett.7b01879.

Appendices

Appendix-A: Simulation box for crumpled graphene electrode at r=89.5Å

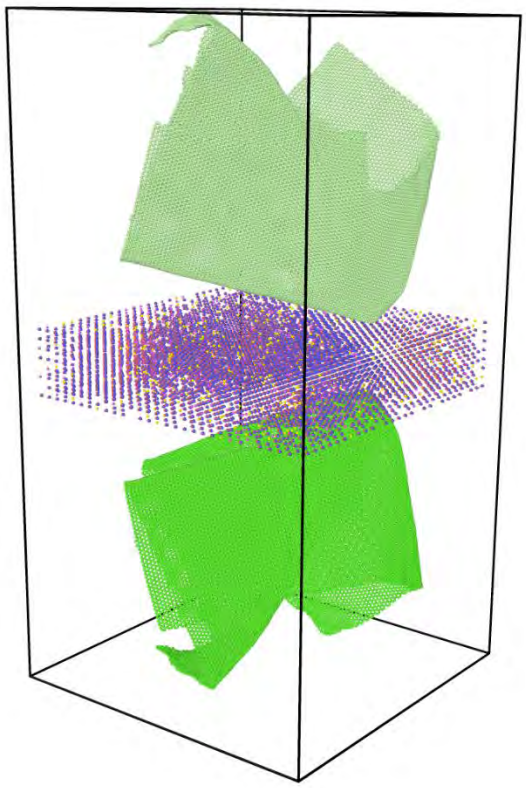

Appendix-B: Code for simulating crumpled graphene

```
dimension       3

units           metal

atom_style      atomic

boundary        p p p

region  box block  -150 150 -150 150 -10 10 units lattice

create_box      1 box

lattice custom 2.4595 a1 1   0   0   a2 0 1.73203 0 basis 0 0 0   basis 0.5 0.16666666666666666 0
basis 0.5 0.5 0 basis 0 0.6666666666666666 0

region  graphene block  -125 125 -125 125 0 0.1 units lattice

create_atoms   1 region graphene

lattice diamond 3.567

mass * 12.011

pair_style airebo/morse 3.0

pair_coeff * * CH.airebo-m C

compute 3 all pe/atom

compute 4 all stress/atom NULL pair

velocity all create   4928459 dist gaussian

fix 1 all npt temp 298 298 .4 x 0.0 0.0 .5 y 0.0 0.0 .5

thermo 10

thermo_style custom step pe ke etotal temp lx ly lz press atoms
```

```
dump 1 all custom 25 dump.${name}.* id x y z vx vy vz c_3 c_4[1] c_4[2] c_4[3]
timestep 0.002
fix bp all balance 250 1 shift z 10 1
thermo_style custom step temp ke pe press pxx pyy vol
run 10000
group graphene region graphene
variable ymn equal ylo+4
variable ymx equal yhi-4
variable xmn equal xlo+4
variable xmx equal xhi-4
region middle block ${xmn} ${xmx} ${ymn} ${ymx} -5 5 units box
group middle region middle
group edge subtract graphene middle
unfix 1
variable r0 equal 212
variable rate equal 0.75
variable radius equal "v_r0 - (step-10000)*dt*v_rate"
fix constrain all indent 1 sphere 0 0 0 v_radius side in units box
change_box all boundary s s s
thermo_style custom step temp ke pe press pxx pyy vol v_radius f_constrain[1] f_constrain[2]
fix nve all nve
run 100000
```